DESIGN AND CHARACTERIZATION OF SEMICONDUCTOR LASER STRUCTURES FOR HYDROGEN SENSING APPLICATIONS

BY

BENJAMIN GEORGE GRIFFIN

DISSERTATION

Submitted in partial fulfillment of the requirements
for the degree of Doctor of Philosophy in Electrical and Computer Engineering
in the Graduate College of the
University of Illinois at Urbana-Champaign, 2013

Urbana, Illinois

Doctoral Committee:

Assistant Professor Lynford L. Goddard, Chair
Professor Kent D. Choquette
Associate Professor Paul Scott Carney
Assistant Professor Gang Logan Liu

ABSTRACT

As gas prices continue to rise and fossil fuels pollute our environment, various alternative fuel sources are being actively pursued. Hydrogen shows considerable promise due to its virtually unlimited supply, energy conversion efficiency, and potentially neutral impact on the environment. However, due to the flammability of hydrogen gas in concentrations as low as 4% in air, reliable sensors capable of detecting small concentrations of hydrogen with quick response times are a necessity.

Photonic-based gas sensors have a wide assortment of advantages over other sensing mechanisms due to their high sensitivity and quick response time. Therefore, several platforms in which semiconductor lasers can be functionalized to detect hydrogen concentrations below the lower explosive limit have been developed. The laser structures were chosen such that there already exist well-established fabrication technologies, and the functionalization method was designed to be easy, practical, and inexpensive so that these devices can be mass produced using existing technologies.

Four different types of hydrogen sensors utilizing thin films of palladium integrated within the structures of semiconductor lasers have been studied. This study includes the design, simulation, fabrication, characterization, and optimization of the devices. The palladium catalyst layer is well known to react to hydrogen gas, forming palladium hydride with optical properties dependent on the hydrogen concentration. This reaction yields a change in complex refractive index and thus also the laser's output power and peak wavelength. The advantages of these sensors are their small size, high sensitivity, wide dynamic range, inline integration, and scalability to arrays.

This thesis is organized into four sections. First, a brief analysis of the rising importance of hydrogen energy sources is presented, followed by an overview of the current state of hydrogen sensing technologies discussing the advantages and disadvantages of each method. Then, a description of

the testing setup and procedure common to all device types is presented. Afterward, an in-depth overview is presented of each of the sensors in terms of the device designs, simulation methods and results, fabrication processes, and experimental measurement results. Finally, comparisons of these device designs are offered and conclusions are made.

To my family, for their support and encouragement.

ACKNOWLEDGMENTS

I am extremely grateful for all of the support from my fellow members of the Photonics Systems Laboratory at the University of Illinois. Their consistent feedback and counsel helped strengthen both the quality of my research and my ability as a researcher. Without them, none of this would have been possible. In particular, I would like to thank my advisor, Professor Lynford Goddard. His continual guidance and patience were indispensable to my personal growth and development. He was always interested in the progress of my research, and always willing to lend advice when I encountered an obstacle. Additionally, it was under his supervision that I had an opportunity to gain experience in every aspect of my research including the device design, simulation, fabrication, and characterization, and for that I am extremely grateful. Of my group members, I would like to give a special thanks to Amir Arbabi and Young Mo Kang. Amir has worked with me steadily throughout my research, always willing to lend a hand and offer advice. His consultation, especially concerning device simulation, has been crucial to my fundamental understanding of semiconductor laser physics. Young Mo has been working alongside me since I first started my graduate studies. He was always there for me when I needed it, and was always willing to help.

Additionally, I would like thank my family for their constant encouragement and advocacy. Whenever I ran into difficulties with either my work or any other aspect of life, they were always there to listen and provide advice. Without their support, I would have never been able to accomplish this achievement.

Finally, I would like to thank the funding sources that supported my graduate education over the years: University of Illinois (startup funds), National Science Foundation (award 0901388), Department of Energy through Lawrence Livermore National Laboratory (PECASE Award: B589070), and the ADM Institute for the Prevention of Postharvest Loss (grant).

TABLE OF CONTENTS

LIST OF TABLES

LIST OF FIGURES

LIST OF ABBREVIATIONS

BCB	Benzocyclobutene
BOE	Buffered Oxide Etch
CW	Continuous Wave
DBR	Distributed Bragg Reflector
DFB	Distributed Feedback (Laser)
EEL	Edge Emitting Laser
FEM	Finite Element Method
FWHM	Full Width at Half Maximum
ICP	Inductively Coupled Plasma
LEL	Lower Explosive Limit
MDL	Minimum Detection Limit
MEMS	Microelectromechanical Systems
MFC	Mass Flow Controller
MOVPE	Metal Organic Vapor Phase Epitaxy
MOX	Metal Oxide
MQW	Multiple Quantum Well
OSA	Optical Spectrum Analyzer
PCB	Printed Circuit Board
PECVD	Plasma Enhanced Chemical Vapor Deposition
PhC	Photonic Crystal

PID	Proportional-Integral-Derivative
PR	Photoresist
PWAM	Plane Wave Admittance Method
QW	Quantum Well
RIE	Reactive Ion Etching
SEM	Scanning Electron Microscope
SMSR	Side Mode Supression Ratio
TEC	Thermoelectric Cooler
TMM	Transmission Matrix Method
VCSEL	Vertical Cavity Surface Emitting Laser

CHAPTER 1

INTRODUCTION

1.1 Motivation

Since the Industrial Revolution, fossil fuels have been used extensively to pave the way for new innovations in science and technology. However, due to tremendous economic growth and a rising world population, fossil fuels are being consumed in unprecedented quantities. Although they have been able to meet the world's demand for energy today, their nonrenewable nature will inevitably lead to a worldwide shortage in the foreseeable future [1]. Additionally, the combustion products from these materials pollute our environment and cause global problems such as the greenhouse effect, stratospheric ozone depletion, and acid rain [2]. It should also be noted that dependence on fossil fuels places a heavy burden on a nation's energy security and independence [3]. The comfortable quality of life we take for granted today is in jeopardy, and in order to protect it, something radical must be done.

Due to our ever-increasing demand for newer technologies, alternative fuel sources must be developed to step up and eliminate our dependence on fossil fuels. Many options are being developed including thermonuclear energy, nuclear breeders, solar energy, biomass, wind energy, hydropower, geothermal energy, ocean currents, tides, and waves [4]. All of these are feasible alternatives for efficient electricity production, but none aside from biomass can be used directly as fuel, which is particularly important for transportation applications. As a result, these alternative energy sources are used to manufacture fuels, as well as generating electricity [5]. Possible candidates for fuel alternatives that are being currently researched include synthetic gasoline, synthetic natural gas (methane), methanol, ethanol, and hydrogen. Of these alternative fuels, hydrogen stands apart from the rest due to its virtually unlimited quantity, versatile nature, significantly higher efficiency

when being converted into a desirable form of energy, and ability to be used without producing pollutants. In fact, from these properties, it can be said that hydrogen is the best possible fuel source being developed today [6]. Due to the abundance of advantages that hydrogen fuel cells have over competing energy storage technologies, great amounts of research are currently going into their development and commercial adoption [7–11].

A major concern when investigating novel technologies is the safety impact on both developers and consumers. The most commonly recognized potential safety hazards of newly researched fuels are the toxicity of the fuel and its byproducts, and the flammability. Hydrogen itself does not present any toxicity concerns, and when burnt with oxygen, the only exhaust is water vapor. However, when burnt with air, lean mixtures must be used to avoid the formation of nitrogen oxides, which are similar to the byproducts from currently used fossil fuels. Due to the ability to prevent the formation of nitrogen oxides when used, hydrogen is considered a relatively safe material in terms of toxicity. However, the primary safety concern that still stands in the way of mass production and public adoption is the lower explosive limit (LEL) of hydrogen concentrations as low as 4% in air at atmospheric pressure [12].

Due to the high temperature nature of most transportation systems, flammability concerns must be quelled before we can usher in a new hydrogen-based economy. Therefore, in order for hydrogen fuel cells to be feasible for transportation applications, reliable sensors with the ability to detect hydrogen leakage at very low concentrations with a quick enough response time to prevent severe accidents are a necessity. The essential parameters to gauge the quality of hydrogen sensors for fuel cell applications are the sensitivity to low concentrations, selectivity to hydrogen gas, fast response time, reusability and durability for long-term use, and that they are economically sound for mass production.

1.2 Current Research in the Field

Due to the recognized promises of hydrogen fuel cell technology, a great deal of work has been invested over the years in the development of adequate sensors to subdue safety concerns over hydrogen usage and storage. Research

has been performed on various mechanisms to detect trace concentrations of hydrogen, which have been incorporated into a variety of different types of devices. The most common types of hydrogen sensors in use today include electrochemical sensors, metal oxide (MOX) sensors, "pellistor"-type combustible gas sensors, thermal conductivity sensors, and optical sensors making use of either evanescent waves interacting with a sensitive thin film or colorimetric devices using indicator dyes [13].

Electrochemical hydrogen sensors can be divided into three main classes including amperometric, potentiometric, and conductometric sensors. A typical electrochemical sensor consists of a sensing electrode and a counter electrode separated by a thin layer of electrolyte. Frequently, a third reference electrode is incorporated within the sensor to provide greater control of the sensing electrode. A current is passed between these electrodes in relation to the target gas concentration [14]. Electrochemical sensors, specifically amperometric sensors, are physically small, have good sensitivity, typically possess a broad linear range, and are stable with relatively long lifetimes. However, these devices have only moderate selectivity (other gases such as carbon monoxide can affect the output of the sensor), have a restricted range of operating temperatures which can affect their potential applications due to the necessary operating environments, and have a dependence on barometric pressure.

MOX sensors are fabricated with a wide band gap semiconductor material, such as tin oxide or another metal oxide as the active element in the sensor [15]. In these sensors, the target gas being detected diffuses into the porous structure, and reacts with the sensor's surface to decrease the surface concentration of oxygen. This lowers the surface potential between adjacent oxide grains, decreasing the electrical resistance. Although these sensors are small in size and able to be efficiently mass-produced, they require elevated temperatures for operation, suffer from very poor selectivity to a specific target gas, and are highly susceptible to humidity variations. In addition to these constraints on their operating environment, MOX sensors are typically very slow to respond and recover to their base point.

A pellistor sensor uses heated ceramics embedded within a noble metal catalyst such as platinum to provide a catalytic surface for hydrogen in air combustion. The device is heated electrically, and the coated surface, which catalyzes combustion when exposed to hydrogen or other combustible va-

pors, causes localized heating on the surface of the sensor. A thin platinum wire is encapsulated within the ceramic layer. When the surface of the device is heated due to the hydrogen combustion, the resistance in the wire increases, and the hydrogen concentration is derived from this change in resistance. This sensor type has become the industry standard for the detection of combustible vapors, however, it cannot differentiate between different combustible gases. Additionally, these devices require significant electrical power to maintain the elevated temperature for the device's operation.

Thermal conductivity sensors operate similarly to pellistor-type sensors; however, they are not heated to a temperature that induces combustion. Instead, they are heated only to a temperature in which the resistance of the sensing element deviates from the linear limit of Ohm's law, reducing the required electrical power for operation. When a sufficiently large electrical power is applied, the ability to dissipate heat to the surrounding environment is exceeded, resulting in an increase in the temperature of the sensing probe element, which causes a deviation from a linear I-V plot. The thermal conductivity of the surrounding gas affects the shape of the I-V curve, causing a change in the measured resistance. The resistance change can be translated to the target gas concentration, assuming that the thermal conductivity of the target gas is known. Thermal conductivity sensors are generally stable devices; however, like the pellistor sensors, they are generally non-selective. One advantage to this sensor type is that unlike the other mentioned hydrogen sensing technologies, thermal conductivity sensors do not require the presence of oxygen for their operation. This allows them to be used for applications that involve a nitrogen purge.

Optical sensors generally make use of a sensitive thin film for hydrogen detection due to the fact that hydrogen is non-absorbing in the ultraviolet, visible, or infrared ranges. A popular material that is both highly sensitive and highly selective to hydrogen gas is palladium (Pd) [16]. When gaseous hydrogen molecules (H_2) come in contact with palladium, some of the hydrogen atoms disassociate from their molecular state and adsorb onto the metal's surface falling into the interstitial sites, forming a palladium hydride (PdH_x). This adsorption results in structural changes as the palladium, denoted as being in the α phase, gradually transitions to the palladium hydride β phase [17]. This phase transition occurs at a specific H_2 concentration ranging from 0.1% to 2%, depending on the thickness and quality of the palladium

film. The primary source of interest in the use of palladium as a hydrogen sensing agent is the fact that it is capable of absorbing up to 900 times its own volume of H_2 [18].

During this transition, the lattice constant of the metal changes a maximum of 3%, which decreases the conductance of the film as a function of H_2 concentration. The conductance differential can be measured electrically, allowing one to easily determine the corresponding H_2 concentration, and as such, electrical sensors using Pd films have been developed [19]. Additionally, palladium has shown its merit in optical applications due to a change in reflectance and transmittance when exposed to hydrogen. This change is caused by an increase in the Fermi level and subsequent decrease in both the real and imaginary components of the dielectric function as the Pd forms PdH_x. This decrease of the dielectric function results in a decrease in reflectivity as a function of H_2 concentration [20]. Furthermore, Pd-based sensors are considered reversible due to the electrical and optical properties mostly resetting back to their original values as H_2 is allowed to escape from the film, though frequent repeated transitions over time can cause some deterioration.

The shift in electrical properties has proven itself beneficial in sensor designs that measure a change in electrical conductivity as a function of H_2 concentration [21, 22], and nanowires that detect a shift in electrical resistance [23, 24]. The shift in the film's mechanical properties is used as an essential component to microelectromechanical system (MEMS) H_2 sensors [25–29]. The shift in optical properties is used in a wide variety of photonic sensor geometries including inexpensively-deposited films that can be interrogated by external lasers [30, 31], optical fiber-based sensors with integrated thin-films [32–38], and as this thesis will present, semiconductor laser structures with integrated thin-films.

1.3 Thesis Outline

As has been shown, there is a strong push for photonic-based gas sensing due to its high sensitivity, fast response times, and reduced chance of sparking, which could be disastrous for flammable gases like H_2. However, almost all commercial photonic sensors for H_2 detection make use of its absorption spectrum, such that the H_2 sensing mechanism is a measurement of the light

absorbed by the gas. The photonic source itself generally does not experience any innate sensing abilities. Research has been done on photonic based H_2 sensors in which the light output of a device directly correlates to the H_2 concentration; however, these implementations are either highly impractical for mass fabrication and deployment for fuel cell leak detection, or are based on optical fibers, which can be quite large. Semiconductor laser structures can be inexpensively mass-produced and arrayed, are low-power, and are usually only orders of microns in size. Additionally, semiconductor lasers are already being mass-fabricated inexpensively for a wide variety of applications. The goal of this thesis is not to create the world's most sensitive H_2 sensor, or even to invent a new type of laser for H_2 detection, but rather to develop an easy, practical, inexpensive means by which to functionalize already well-established semiconductor laser structures as a platform for H_2 sensing of concentrations below the LEL for fuel cell leak detection applications. Additionally, this same platform can be expanded into a wide variety of sensing applications other than H_2 by replacing the Pd film with a different catalyst layer.

Semiconductor lasers can generally be separated into two categories: in-line edge-emitting lasers, and vertically-emitting lasers. Each configuration has its own benefits depending on the specific application and implementation; therefore, pursuing a means to functionalize both types is desired. Of each category, a wide variety of specific geometries and designs have been developed. The laser designs pursued in this thesis were chosen such that the sensitive Pd film can be located as close to the optical mode as possible, leading to the highest sensitivity. Therefore, a ridge-waveguide structure was chosen for the edge-emitting lasers, and an etched photonic crystal pattern has been chosen for the vertically-emitting lasers. The results that will be shown for these devices indicate that both configurations are capable of detecting H_2 at the necessary concentrations; however, the single mode nature of the vertically-emitting laser leads to superior wavelength measurement results. Therefore, work was done to develop a single-mode edge-emitting laser as an alternative to the standard ridge-waveguide edge-emitting laser. This was done by analyzing both a distributed Bragg reflector (DBR) laser and a distributed feedback (DFB) laser. The scope of this thesis covers the design, simulation, fabrication, analysis, and optimization of these semiconductor laser structures.

CHAPTER 2

RIDGE-WAVEGUIDE EDGE-EMITTING LASER SENSOR

A laser cavity is formed when a gain medium is surrounded on each end by a reflecting surface, which provides optical feedback of stimulated photons. In the case of in-plane semiconductor laser cavities, the gain medium is formed using a semiconductor quantum well (commonly referred to as the active region), and the reflectors are formed with simple cleaved facets. Since the semiconductor material will naturally cleave along the crystal axis, the cleaved facets are very smooth and their reflectivities can be determined from the index contrast between the semiconductor and air. For the case of a GaAs-based laser as used here, this facet reflectivity is approximately 31%. The lasing wavelength is defined by the material gain, which is set by the quantum wells, and the resonant wavelength of the structure. The resonant wavelengths for a basic edge-emitting laser (EEL) can be determined using a simple Fabry-Pérot cavity, such that the wavelength, λ, can be determined from

$$\lambda = \frac{2\,n\,L}{m} \tag{2.1}$$

where n is the refractive index of the cavity (the semiconductor, in this case), L is the length of the cavity (determined by where the semiconductor is cleaved), and m is an arbitrary integer value that determines the mode order. It is clear from the use of an arbitrary integer value that the Fabry-Pérot cavity has many resonant wavelength values. The separation between each of these resonant wavelengths, known as the free spectral range, is given by

$$\Delta\lambda = \frac{\lambda_0^2}{2\,n\,L} \tag{2.2}$$

where λ_0 is the central wavelength of the nearest peak. The wavelengths at which the laser will lase are determined by the overlap between these resonant wavelengths of the cavity, and the material gain curve, which depends on the quantum well material, thickness, strain, and operating temperature.

In order to make an EEL that produces a narrow beam of light emission, we must consider the lateral confinement of current, carriers, and photons. A great many techniques have been developed over the years that provide successful lateral confinement, with some designs being more practical than others [39–43]. However, for these H_2 sensing applications, a confinement technique that exposes, to the ambient environment, portions of the laser which have a strong overlap with the optical mode is required. It was chosen to pursue an ridge-waveguide structure, which consists of a narrow, etched ridge in which the surfaces of the etched trenches on each side of the ridge are located just above the active region, which overlaps with the evanescent portions of the optical mode. If a material like Pd is placed along the surface of these trenches, then as the mode travels down the laser cavity, it will be in constant interaction with this film, and the optical output properties of the laser will depend on the optical properties of the film. Therefore, if the optical properties of the film were to change while the laser is in operation, the optical output from the laser would change in response. Since it is known that Pd experiences a shift in refractive index when it forms PdH_x, this would enable H_2 detection by monitoring the output of the laser.

2.1 Device Design

The ridge-waveguide edge-emitting laser (EEL) sensor, as shown in Fig. 2.1, contains a narrow ridge (3–6 μm wide) with trenches etched down close to the active region of the material. A thin layer of Pd (10–30 nm thick) is then deposited over the device, such that it is located at the bottom of the etched trench of each side of the ridge. This location allows for the evanescent portions of the optical mode of the laser to overlap with the Pd film as it propagates through the cavity. When the device encounters H_2, the PdH_x is formed, which has a different complex refractive index from pure Pd. Therefore, incorporating this film in the laser structure such that the optical mode interacts with the Pd, causes the output of the device to change when the film is exposed to H_2. This principle allows for measurement of the H_2 concentration as a function of the device's output power and/or wavelength. For the fabricated device, this change yields a power increase and a peak wavelength redshift. The magnitude of this power and wavelength shift is roughly linearly proportional to the H_2 concentration.

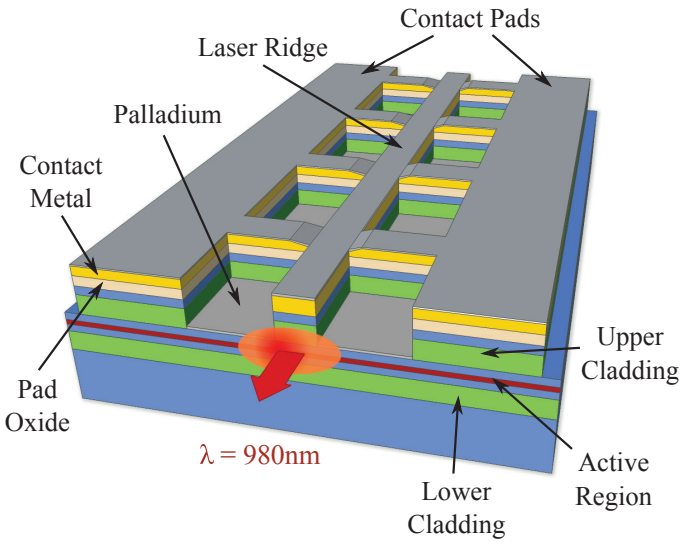

Figure 2.1: Illustration of the ridge-waveguide edge-emitting laser H_2 sensor.

The ridge-waveguide EEL structure has gone through several design iterations since its initial conception, and has been changed to account for practical fabrication and testing methods. The initial scheme for the devices was to develop an entire chip of hydrogen sensors with a large array of varied parameters. After measurements were made, solid conclusions about the effects of each parameter could be drawn, and the optimization process for these devices would be performed. Additionally, aspects of an appropriate testing setup were considered. Several of the earlier designs were fabricated and tested, and either produced poor lasing results, or presented characterization difficulties. The structure shown in Fig. 2.1 is the most recent device design, and has been shown to be easy to test, and acceptably sensitive to hydrogen [44,45]. The layer structure for the material that has been used for the device fabrication and simulation is shown in Table 2.1. It is designed to lase at a wavelength of 980 nm.

2.2 Simulation Methods

The goals for the device simulations are to determine what effects the shift in refractive index of the Pd film has on the laser's output power and wavelength, and to see what effect the ridge waveguide width and operating temperature have on the device's sensitivity. The simulation is performed by

Table 2.1: Layer structure for the ridge-waveguide edge-emitting laser sensors

Layer	**Material**	**Thickness (nm)**	**Dopant Species**	**Concentration (cm^{-3})**
Cap	GaAs	100	C (p)	$> 1 \times 10^{19}$
Cladding	$Al_{0.8}Ga_{0.2}As$	500	C (p)	$3 - 8 \times 10^{17}$
Core	GaAs	80	—	—
QW	$In_{0.2}Ga_{0.8}As$	8	—	—
Core	GaAs	80	—	—
Cladding	$Al_{0.8}Ga_{0.2}As$	1000	Si (n)	1×10^{18}
Buffer	GaAs	100	Si (n)	$> 1 \times 10^{18}$
Substrate	GaAs	—	Si (n)	—

first calculating the electric and magnetic field profiles using the finite element method (FEM) in COMSOL Multiphysics, and obtaining an effective index for the guided mode. This is repeated for a variety of ridge widths to determine what impact the width has on the overall sensitivity of the device. A profile of the normalized electric field for a two-dimensional cross-section of the device is shown in Fig. 2.2, with the overlap between the optical mode and Pd film labeled.

The values for the refractive index of Pd at a wavelength of 980 nm in the absence of H_2 are taken as $n = 1.62$ and $\kappa = 4.31$, which are the values reported at a wavelength of 835 nm from [46]. After being exposed to 4% H_2 (the lower explosive limit), the new values for the refractive index are $n = 1.45$ and $\kappa = 3.86$.

To quantify the impact of the ridge width on the device's sensitivity, the mode overlap with the Pd film was calculated using the FEM simulation results according to

$$\Gamma_{Pd} = n_{Pd} \cdot \frac{\frac{1}{\eta_0} \int_{\text{Pd Layer}} |\mathbf{E}|^2 \, \mathrm{d}S}{\mathrm{Re}\left\{ \int_{\text{Total}} \mathbf{E} \times \mathbf{H}^* \, \mathrm{d}S \right\}} \tag{2.3}$$

which represent the optical confinement factor for the Pd layer. The value for this confinement factor can be interpreted to represent how much interaction the optical mode has with the Pd film, suggesting that larger values for Γ_{Pd} correspond to higher sensitivities to changes in the Pd's optical properties.

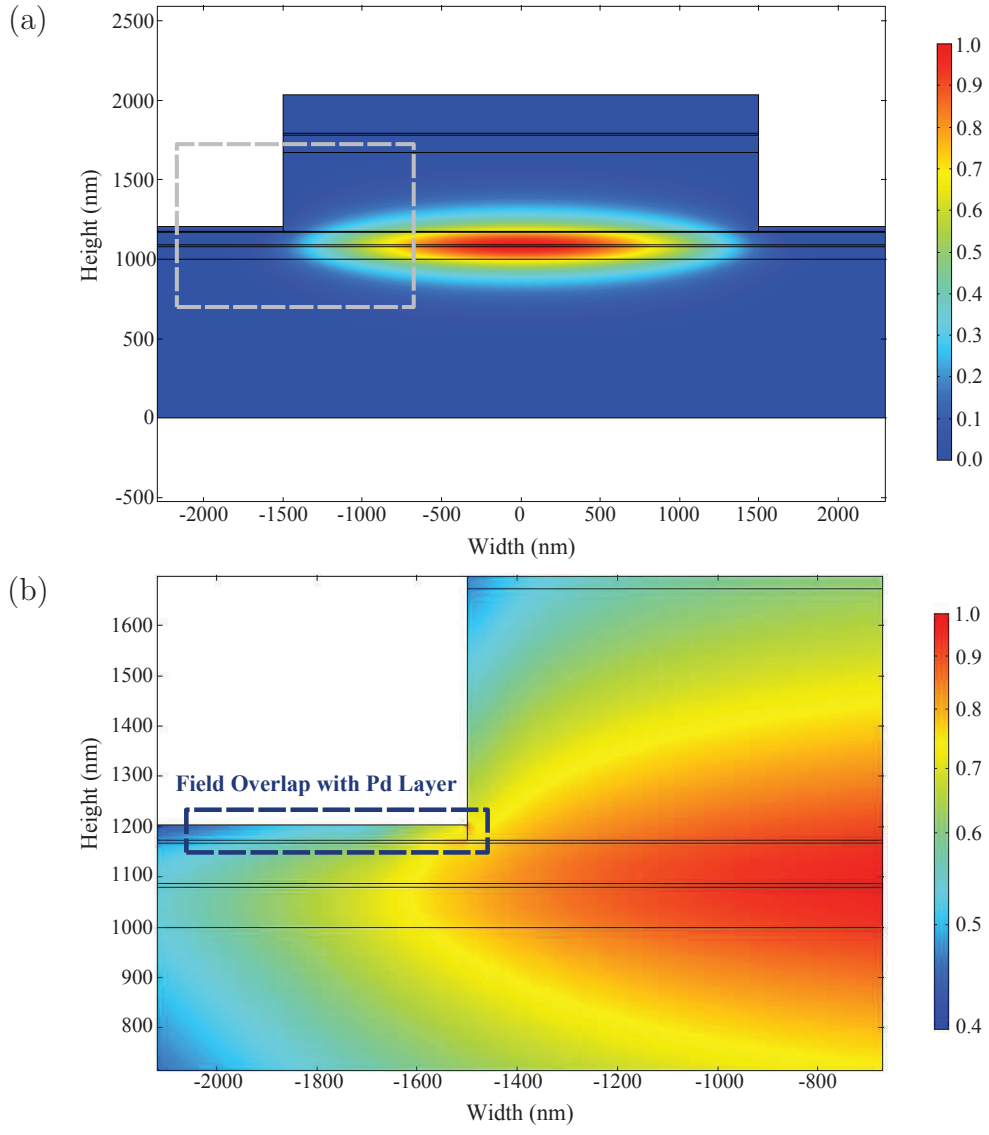

Figure 2.2: (a) Profile of the normalized electric field in the ridge-waveguide structure, and (b) zoomed-in view of the log of the normalized electric field, showing the overlap between the field and the Pd layer.

The theoretical shift of laser output power in response to H_2 exposure is calculated using an analytical model for laser diodes. First, the threshold gain g_{th} is calculated according to

$$\Gamma_{QW} \cdot g_{th} = \alpha_{i,0} + \alpha_{i,Pd} + \alpha_m \tag{2.4}$$

where Γ_{QW} is the optical confinement factor in the quantum well calculated from the FEM simulation, $\alpha_{i,0}$ represents the propagation loss due to sidewall roughness and free carrier absorption, $\alpha_{i,Pd}$ expresses the propagation loss due to the Pd layer, and α_m represents the mirror loss. The optical confinement factor in the quantum well is determined to be $\Gamma = 4.25\%$, and is changed a negligible amount after H_2 exposure. The internal loss $\alpha_{i,0}$ used is a standard value of 5 cm^{-1} from [39], while α_m is calculated from

$$\alpha_m = \frac{1}{L} \ln\left(\frac{1}{R}\right) \tag{2.5}$$

with L representing the cavity length of 450 μm and R representing the facet reflectivity given by

$$R = \left| \frac{n_{air} - \tilde{n}_{eff}}{n_{air} + \tilde{n}_{eff}} \right|^2 \tag{2.6}$$

where n_{air} represents the refractive index of air and $\tilde{n}_{eff}$ represents the complex effective mode index found in the FEM simulation. Finally, $\alpha_{i,Pd}$ from (2.4) is calculated using

$$\alpha_{i,Pd} = \frac{4\pi}{\lambda} \cdot \kappa_{eff} \tag{2.7}$$

with κ_{eff} representing the imaginary component of the effective index found in the FEM simulation.

After computing the threshold gains according to (2.4) both before and after H_2 exposure, the threshold carrier densities are determined using a material database obtained from Nonlinear Control Strategies SimuLase that matches the layer structure used for the experimental measurements. This gain database as a function of wavelength for a variety of carrier densities is shown in Fig. 2.3. The values of peak material gain as a function of the two-dimensional sheet carrier density for a variety of temperatures provided by the SimuLase database are shown in Fig. 2.4. The data points represent the

information included in the database and the fit curves have been modeled according to

$$g = g_0 \cdot \ln\left[\frac{N + N_s}{N_{tr} + N_s}\right] \tag{2.8}$$

using values for the transparency carrier density, N_{tr}, provided by the gain database, and standard values for the linearity parameter, N_s, from [39] as starting points for the fit.

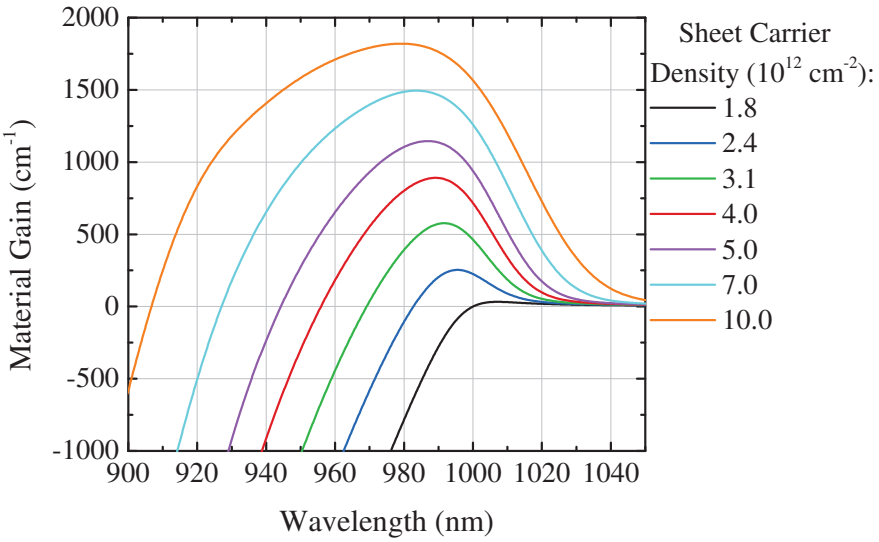

Figure 2.3: Material gain for the EEL laser layer structure as a function of wavelength for select sheet carrier density values.

The data from these gain curves is then interpolated to produce the threshold carrier densities for the 3 μm and 4 μm ridge width devices before and after H_2 exposure for operating temperatures of 20°C and 60°C. The carrier density values are then used in

$$I_{th} = \frac{q\,V}{\eta_i}\left(A\,N_{th} + B\,N_{th}^2 + C\,N_{th}^3\right) \tag{2.9}$$

to produce the theoretical threshold currents. In this equation, V represents the volume of the active region and η_i represents the internal efficiency, in which a standard value of 0.8 from [39] is used. The variables A, B, and C are the recombination coefficients due to non-radiative, spontaneous, and Auger processes, respectively. Standard values of $A = 1{\times}10^8$ s^{-1}, $B = 8{\times}10^{-11}$ cm^3/s, and $C = 6{\times}10^{-30}$ cm^6/s for an 80 Å $In_{0.2}Ga_{0.8}As/GaAs$ quantum well designed to lase at 980 nm from [39] were used. Once the threshold currents have been

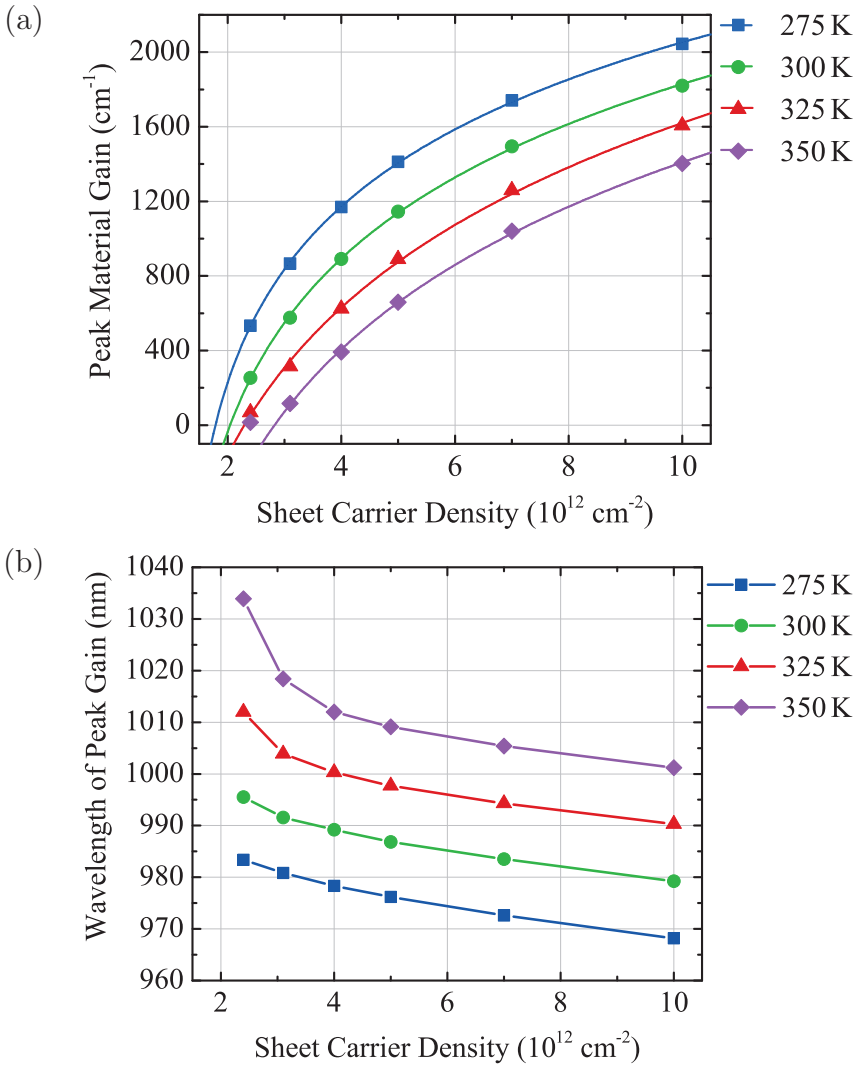

Figure 2.4: Modeled (a) peak material gain versus sheet carrier density with curve fits, and (b) wavelength of peak gain versus sheet carrier density, at a variety of temperatures.

determined, the laser output power can be calculated using

$$P_0 = \eta_i \left(\frac{\alpha_m}{\alpha_{i,0} + \alpha_{i,Pd} + \alpha_m} \right) \frac{h\nu}{q} (I - I_{th}) \tag{2.10}$$

After calculating the laser output powers, L-I curves can be computed for the 3 μm and 4 μm ridge widths at operating temperatures of 20°C and 60°C before and after H_2 exposure. This can be used to determine what effect these parameters have on the sensor's performance. Finally, assuming the longitudinal and transverse mode numbers are unchanged, the expected

lasing wavelength shift can be calculated according to

$$\frac{\Delta\lambda}{\lambda} = \frac{\Delta n_{eff}}{n_{eff}} \tag{2.11}$$

In this equation, n_{eff} represents the real component of the effective index produced from the FEM simulations, Δn_{eff} represents the shift in this effective index with the introduction of H_2, and λ represents the design wavelength of 980 nm. The actual shift may be smaller or of the opposite sign if the mode numbers change due to H_2 exposure.

2.3 Simulation Results

The results of the FEM simulation that illustrate the effect of the waveguide ridge width on the sensitivity of the devices are presented in Fig. 2.5. This figure shows that narrower ridge widths produce significantly higher confinement factors in the Pd layer, suggesting that these devices will be far more sensitive to H_2 exposure than wider ridges. Also, at higher H_2 concentration, the confinement in the Pd increases.

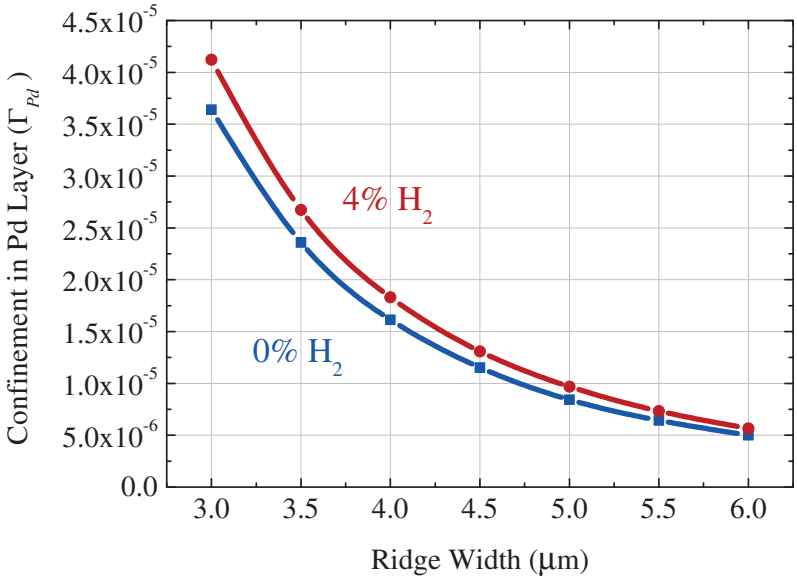

Figure 2.5: Modeled confinement of the optical mode in the 30 nm-thick Pd layer as a function of ridge width before and after H_2 exposure.

Additionally, the results from the analytical calculations are tabulated in Table 2.2. Plots of the simulated L-I curves for the 3 μm and 4 μm

ridge width lasers before and after H_2 exposure for operating temperatures of 20°C and 60°C are shown in Fig. 2.6. The data presented in the table and simulated L-I curves further suggest that the 3 μm device exhibits a larger power and wavelength shift than the 4 μm device, and that an elevated operating temperature will improve the sensitivity of these devices regardless of ridge width, at the penalty of a larger threshold current.

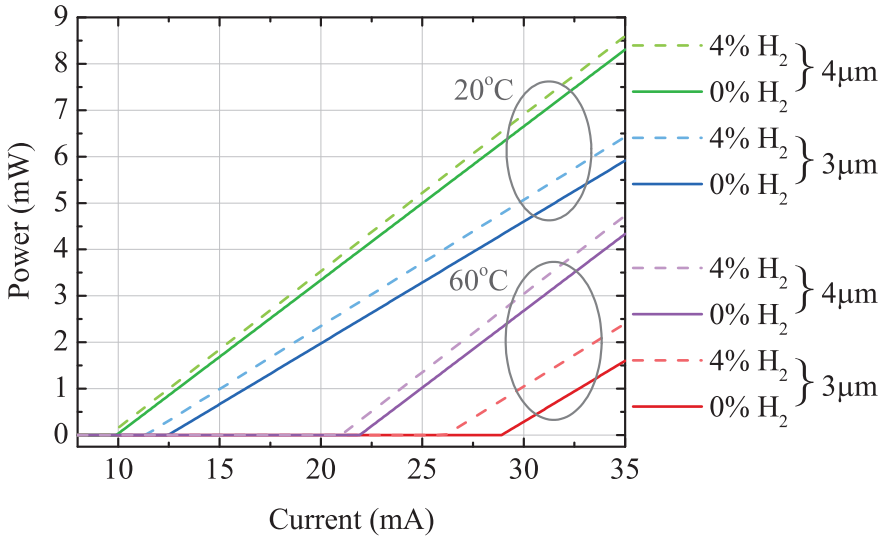

Figure 2.6: Simulated L-I curves for the 3 μm and 4 μm ridge width lasers before and after H_2 exposure under operating temperatures of 20°C and 60°C.

Table 2.2: Simulation results for the ridge-waveguide edge-emitting laser sensors

Parameters	**Symbol**	**H_2**	**3 μm Ridge**	**4 μm Ridge**
Effective Index	$\tilde{n}_{eff}$	0%	$3.283-i1.63\times10^{-4}$	$3.285-i7.63\times10^{-5}$
		4%	$3.287-i1.49\times10^{-4}$	$3.288-i6.96\times10^{-5}$
Confinement in Pd	Γ_{Pd}	0%	3.64×10^{-5}	1.61×10^{-5}
		4%	4.12×10^{-5}	1.83×10^{-5}
Mirror Loss	α_m	0%	27.96 cm^{-1}	27.95 cm^{-1}
		4%	27.93 cm^{-1}	27.92 cm^{-1}
Pd Loss	$\alpha_{i,Pd}$	0%	20.96 cm^{-1}	9.78 cm^{-1}
		4%	19.07 cm^{-1}	8.93 cm^{-1}
Threshold Gain	g_{th}	0%	1269.85 cm^{-1}	1007.22 cm^{-1}
		4%	1224.60 cm^{-1}	986.38 cm^{-1}
Threshold Carrier Density (20°C)	N_{th}	0%	5.24×10^{12} cm^{-2}	4.11×10^{12} cm^{-2}
		4%	5.01×10^{12} cm^{-2}	4.03×10^{12} cm^{-2}
Threshold Carrier Density (60°C)	N_{th}	0%	7.61×10^{12} cm^{-2}	5.94×10^{12} cm^{-2}
		4%	7.29×10^{12} cm^{-2}	5.82×10^{12} cm^{-2}
Threshold Current (20°C)	I_{th}	0%	12.47 mA	9.91 mA
		4%	11.35 mA	9.54 mA
Threshold Current (60°C)	I_{th}	0%	28.90 mA	21.91 mA
		4%	26.15 mA	20.99 mA
Differential Efficiency	η_d	0%	0.41	0.52
		4%	0.43	0.53
Wavelength Shift	$\Delta\lambda$	$0 \rightarrow 4\%$	1.11 nm	0.88 nm

2.4 Device Fabrication

In addition to simulations, these devices have been successfully fabricated. The fabrication process (detailed in Appendix B.1) begins with the deposition of the insulating SiO_2 layer on the sample by plasma enhanced chemical vapor deposition (PECVD). The sample is then patterned using photolithography and etched using a CF_4 plasma. These steps are performed to transfer the pad oxide pattern onto the sample. The pad oxide covers the contact pad areas, as well as the interconnects between the contact pads and the ridge. The actual laser ridge is uncovered.

Next, photolithography is used to define the location of the contact metal. This contact metal will serve as a self-aligned wet etch mask for the laser ridge. A top-side p-type contact, Ti/Pt/Au (15/10/200 nm), is deposited, and the unwanted metal is lifted off in acetone. A phosphoric acid etch mixture, H_3PO_4:H_2O_2:H_2O (1:1:10), is used as the wet etchant. It is known to etch both the GaAs contact layer and the AlGaAs upper cladding at comparable etch rates. The total etch depth is 600 nm, which is 80 nm above the active region. It should be noted that this etch produces undercutting on each side of the etched ridge, producing a narrower ridge width than designed by the photolithography mask.

Finally, the patterned Pd layer (30 nm thickness) is deposited and lifted off using the same procedure as the contact metallization. The purpose of the patterning and lift-off as opposed to a blanket deposition is to prevent unwanted electrical shorting between adjacent devices.

After the Pd layer is patterned, the sample is lapped and polished to a much thinner size to reduce series resistance of the device and to facilitate cleaving. After the sample is thinned, the backside n-type contacts, Ge/Au/Ni/Au (20/50/30/50 nm), are deposited, and the sample is annealed at 400°C for 30 seconds in an N_2 ambient to alloy the n-type contacts as well as anneal the Pd layer.

After all processing is complete, the laser facets are carefully cleaved. This cleaving allows for control of the laser's cavity length, which is a potentially critical parameter for the operation of this sensor. A longer cavity length allows for a greater interaction length between the optical mode and the Pd layer; however, a shorter cavity allows for a wider longitudinal mode spacing, which may improve wavelength measurements. The cavity length

chosen for these devices is 450 μm. Figure 2.7 shows SEM images of the finalized devices.

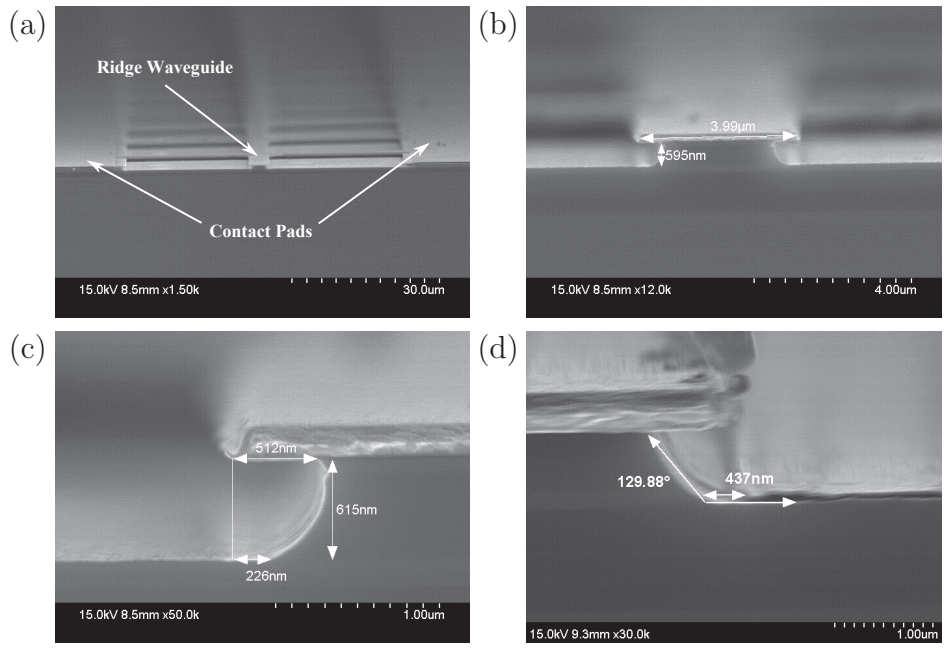

Figure 2.7: SEM images of the fabricated EEL sensors (a) zoomed-out, labeling the contact pads and laser ridge, (b) zoomed-in on a 4 μm-wide laser ridge, (c) zoomed-in on a ridge sidewall showing measurements of the wet etch undercutting, and (d) zoomed-in on a ridge sidewall showing the sidewall angle.

2.5 Experimental Measurements

Due to the simulation results suggesting that a narrower ridge width would be more sensitive, a 3 μm- and 4 μm-wide device are used for these measurements. Figure 2.8 shows L-I curves of the 3 μm device before and after a two hour 2% hydrogen exposure. As shown, above threshold the laser's output power is higher after being exposed to H_2. The greatest shift in power seems to be at 95 mA injection current. Therefore, this point was chosen for the further measurements to yield the greatest sensitivity. Figure 2.9 shows the output spectra of the device pumped at 95 mA after being exposed to 0.5%, 1.0%, 1.5%, and 2.0% H_2 in N_2. As the H_2 concentration is increased, the spectrum redshifts and the power intensity increases. According to the spectra, this redshift is roughly 50 pm per percent H_2.

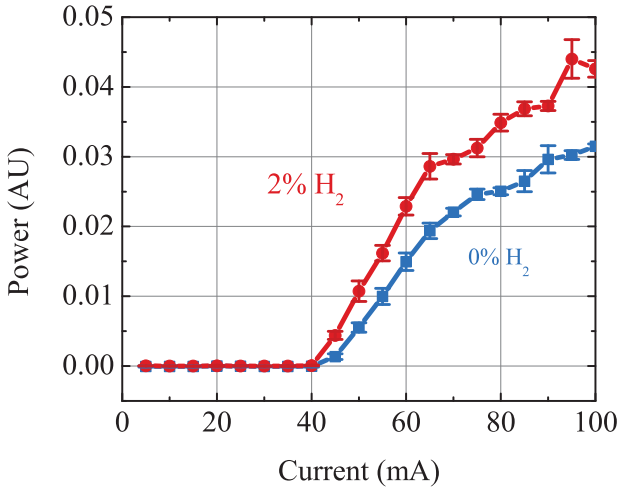

Figure 2.8: L-I Curves of the 3 μm ridge width EEL sensor before and after exposure to 2% H_2.

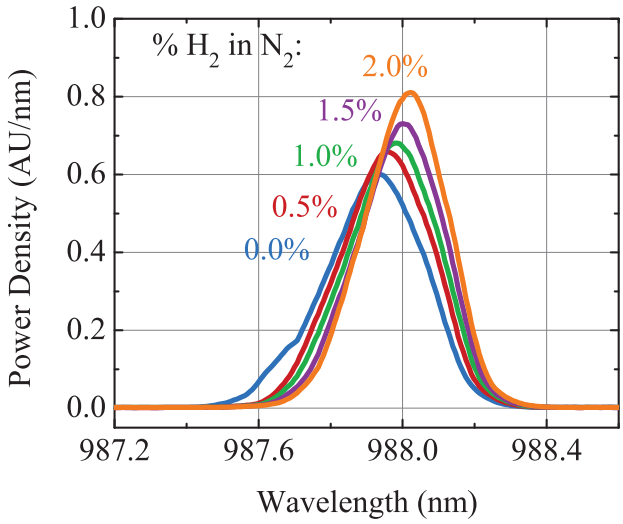

Figure 2.9: Spectra for the 3 μm ridge width EEL sensor for various concentrations of H_2 between 1–2% demonstrating the peak wavelength shift.

The next measurements performed were time-dependent studies in which a constant injection current of 95 mA was applied, and only the H_2 concentration was varied. The laser output power and spectra were simultaneously monitored during these measurements. Figure 2.10(a) shows how the laser's power shifts during these varying H_2 exposures. As shown, the power increases when the H_2 is turned on, and the device recovers back to its original power when the H_2 is turned off. Additionally, each power increase is propor-

tional to the concentration of H_2 flowing into the chamber. The power shift for this device is roughly 15% per percent H_2. Likewise, Fig. 2.10(b) shows how the peak wavelength and the full width at half maximum (FWHM) center shift as the H_2 concentration is varied. Like the power measurements, these wavelength measurements exhibit shifts proportional to the H_2 concentration, and recover back to their base points when the H_2 is turned off. For both the power and wavelength measurements, the response time is roughly 3 minutes.

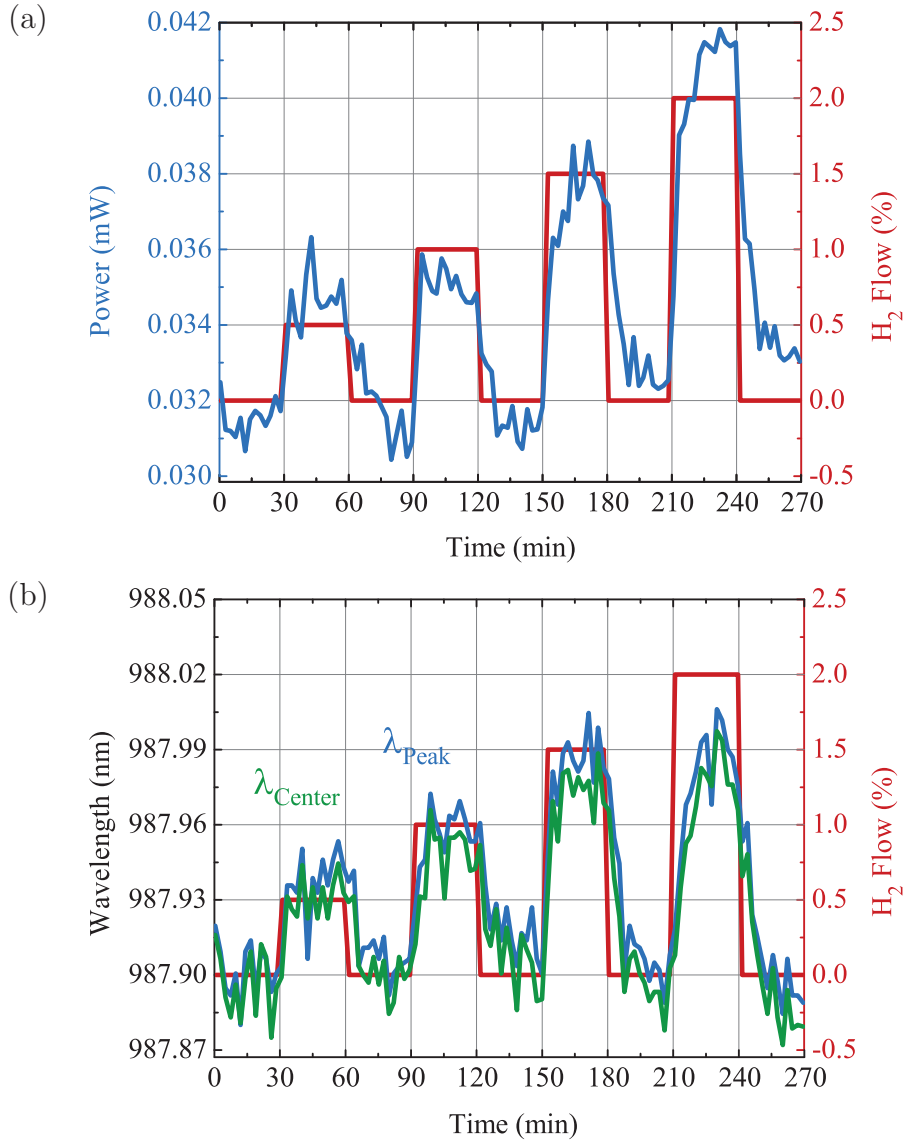

Figure 2.10: H_2 pulse measurements showing (a) output power, and (b) peak wavelength and FWHM center for the 3 μm ridge width EEL sensor.

To study the effects of the ridge width on the device's performance, the measurement results from the 3 μm-wide device were compared to those of a 4 μm-wide device. Figure 2.11 shows the L-I curves for the 4 μm device before and after exposure to 2% H_2, which can be directly compared to the L-I curves for the 3 μm device shown in Fig. 2.8. Figure 2.12 shows the output spectra for both of these devices before and after exposure to 2% H_2 at an operating temperature of 20°C. As shown, the power shift in the L-I curve for the 3 μm device is far more significant than that of the 4 μm device. Additionally, the spectrum from the 4 μm device does not shift noticeably. The 4 μm ridge width laser has multiple peaks, and adding H_2 causes power to transfer from one peak to the other. It is clear that the single-peak nature of the 3 μm device is necessary for sensor measurements using wavelength. The 3 μm device, however, shows a clear redshift after the H_2 exposure. As the simulation results suggest, the 3 μm device is clearly more sensitive to H_2 than the 4 μm device.

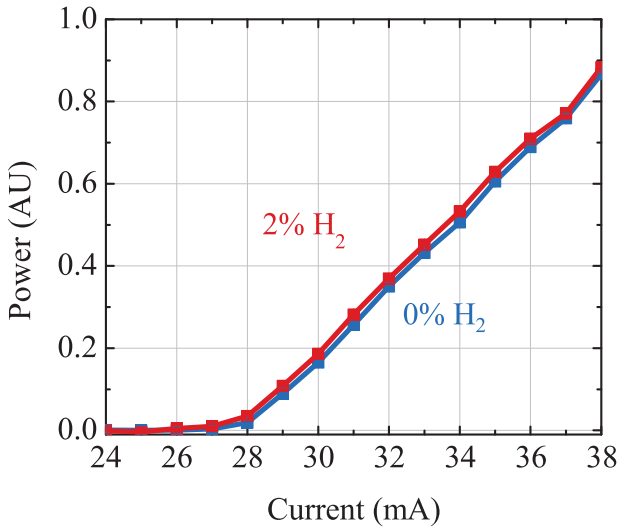

Figure 2.11: L-I Curves of the 4 μm ridge width EEL sensor before and after exposure to 2% H_2.

An important parameter to consider when it comes to the device sensitivity and the environments in which that device can operate is the operating temperature. As the laser is heated, the output power will decrease; however, the Pd film should be able to absorb H_2 easier, improving the response time and sensitivity. Therefore, the sensor was measured under a variety of operating temperatures using the temperature stage built into the test

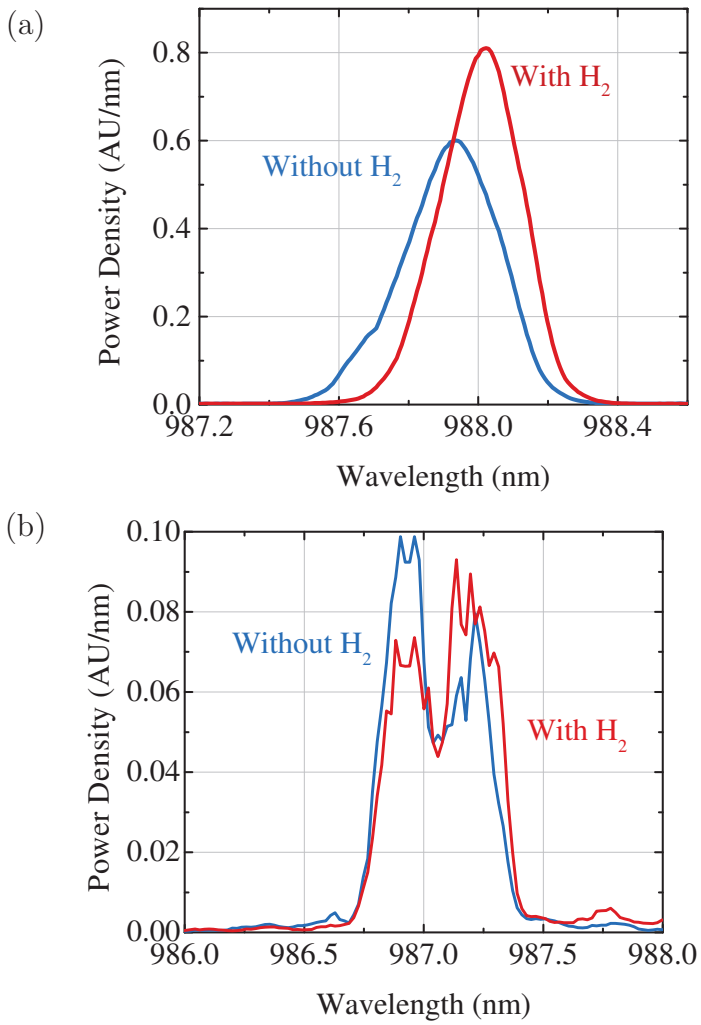

Figure 2.12: Lasing spectra before and after H_2 exposure showing a comparison between the (a) 3 μm ridge width, and (b) 4 μm ridge width EEL sensors.

chamber. Figure 2.13 shows the L-I curves for the 3 μm device for various operating temperatures before and after soaking in 2% H_2. After the device has been soaked in H_2, the threshold current decreases and the output power increases. It should also be noted that as the operating temperature is increased, the threshold current and the sensitivity to H_2 increases. The increase in power with respect to H_2 exposure and the increase in threshold current with respect to operating temperature follow the same trend as the simulation results. It should be noted, however, that the measured threshold current and differential efficiency are not as good as predicted, but this is likely due to defects introduced during the wafer growth.

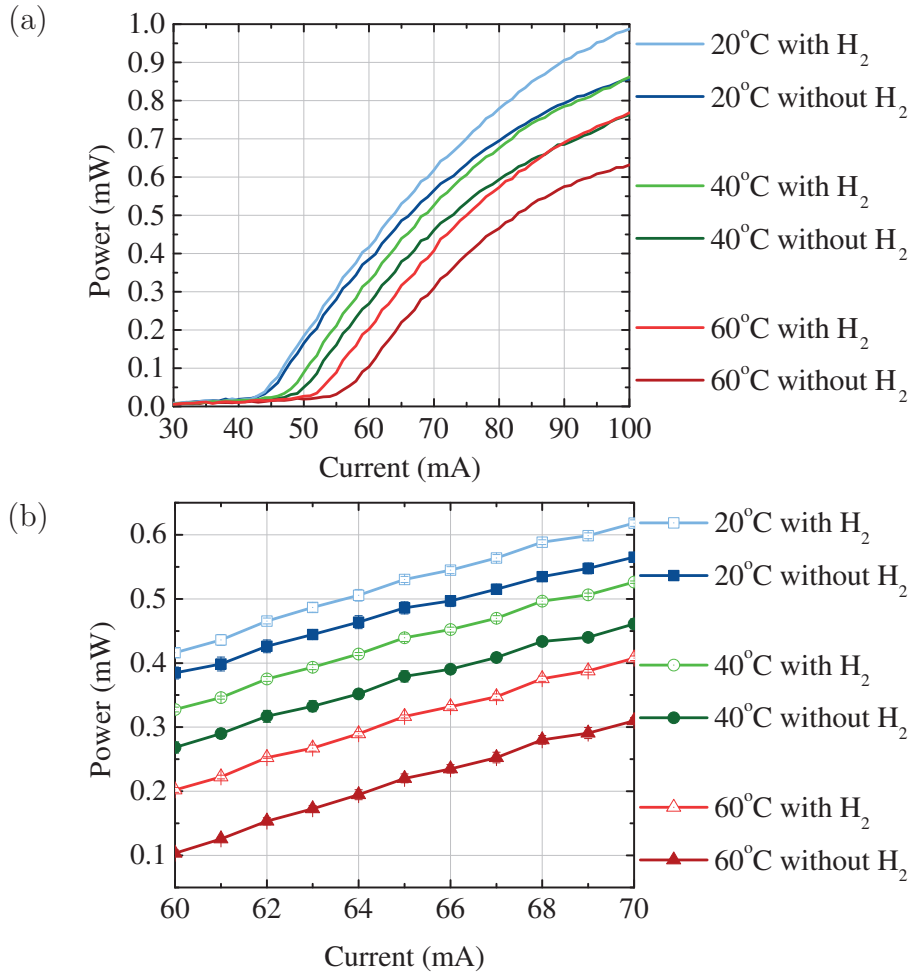

Figure 2.13: L-I curves from the 3μm ridge width sensor before and after H_2 exposure for various temperatures showing (a) a zoomed-out, and (b) a zoomed-in view of the power shift.

Additionally, to observe the effect of temperature on the sensor's response time, an H_2 pulse measurement is taken. The result of this measurement is shown in Fig. 2.14. Due to the increase in threshold current with increased temperature, Fig. 2.14 is plotted at constant baseline power for comparisons. For the 20°C measurement, an injection current of 60 mA is used, and is then increased to 66 mA for the 40°C measurement, and 74 mA for the 60°C measurement. It is clear from these results that the increased temperature decreases both the response and recovery times of the sensor. It is believed that all three temperature measurements are of roughly the same sensitivity (i.e. ΔP is the same) due to the different levels of injection current.

The same L-I measurements were performed for the 4 μm device for various

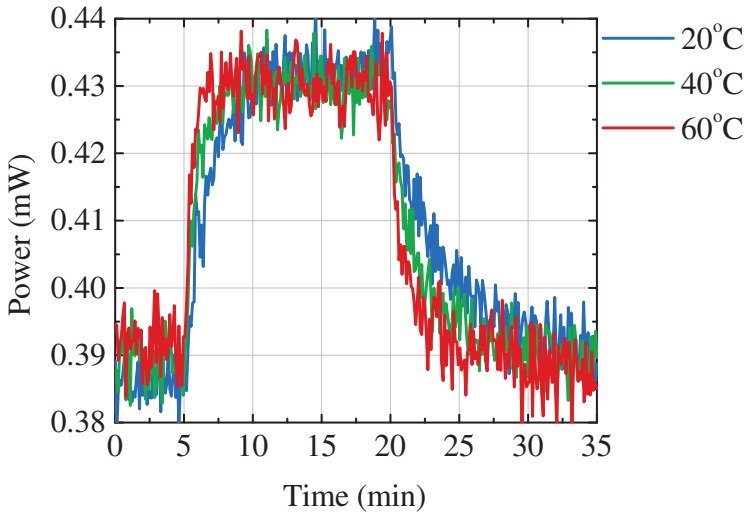

Figure 2.14: H_2 pulse measurements at various temperatures for a 3 μm ridge width sensor showing the effect of operating temperature on response time.

temperatures with and without H_2. The results for these measurements are shown in Fig. 2.15. Like the 3 μm device, the power increases when exposed to H_2. Additionally, the threshold current and sensitivity increase with increased operating temperature.

Additionally, H_2 pulse measurements were taken for the 4 μm device under various operating temperatures. Figure 2.16(a) shows the pulse comparisons with injection current values comparable to those of the 3 μm device. However, as shown in Fig. 2.15, the threshold current for the 4 μm device is considerably lower, resulting in a higher output power for the same injection current. Therefore, Fig. 2.16(b) is also provided showing H_2 pulse results for the 4 μm device at a lower injection current so that the baseline power is comparable to that of the 3 μm device in Fig. 2.14. For an operating temperature of 20°C, an injection current of 32 mA is used. This injection current is then scaled similarly to the 3 μm device for the higher operating temperatures. It is clear from Fig. 2.16 that the 4 μm device is less sensitive than the 3 μm device, and is slower to respond and recover. To illustrate this, Fig. 2.17 shows the pulse measurement results of both the 3 μm and 4 μm devices at 20°C for a similar baseline power.

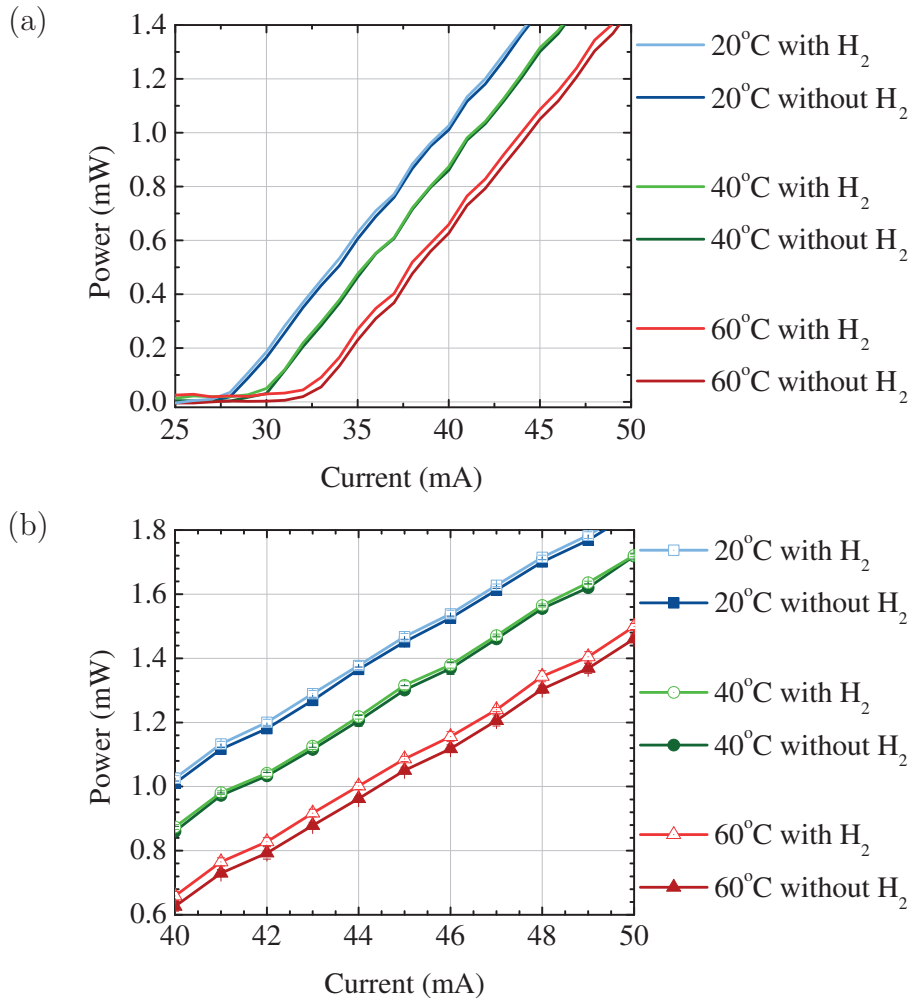

Figure 2.15: L-I curves from the 4μm ridge width sensor before and after H_2 exposure for various temperatures showing (a) a zoomed-out, and (b) a zoomed-in view of the power shift.

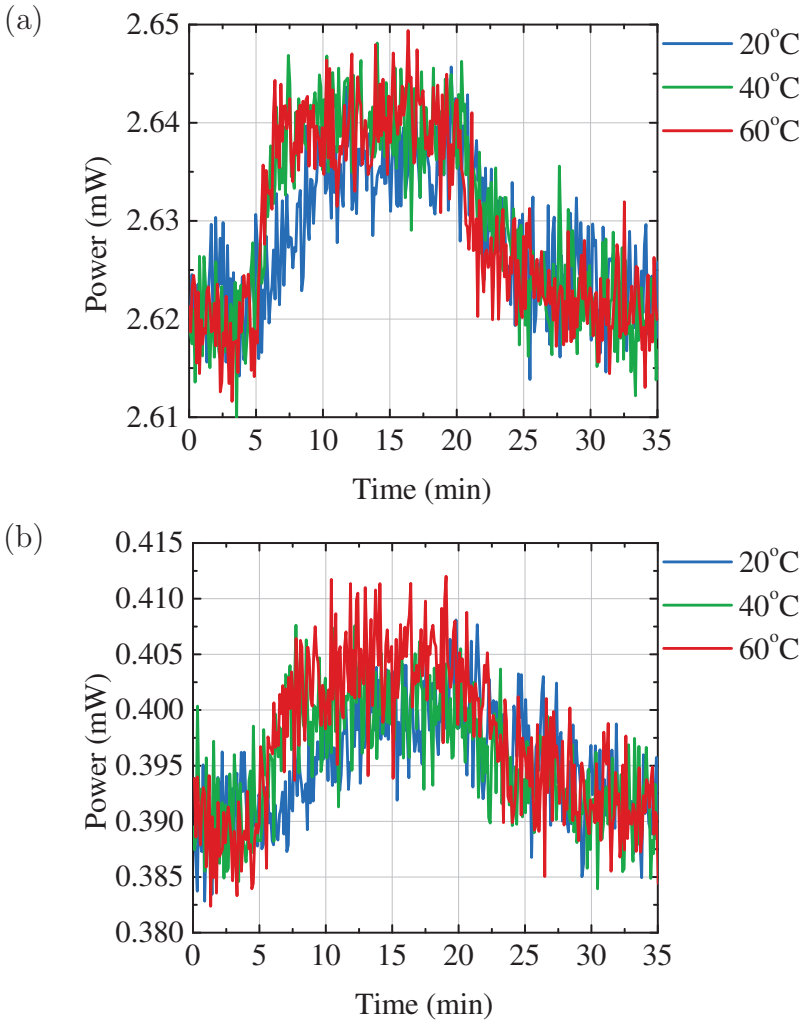

Figure 2.16: H_2 pulse measurements at various temperatures for a 4 μm ridge width sensor showing the effect of operating temperature on response time. (a) High-power measurements, keeping the injection current at the same level as that of the 3 μm ridge width device, and (b) low-power measurements, keeping the base power at the same level as that of the 3 μm device.

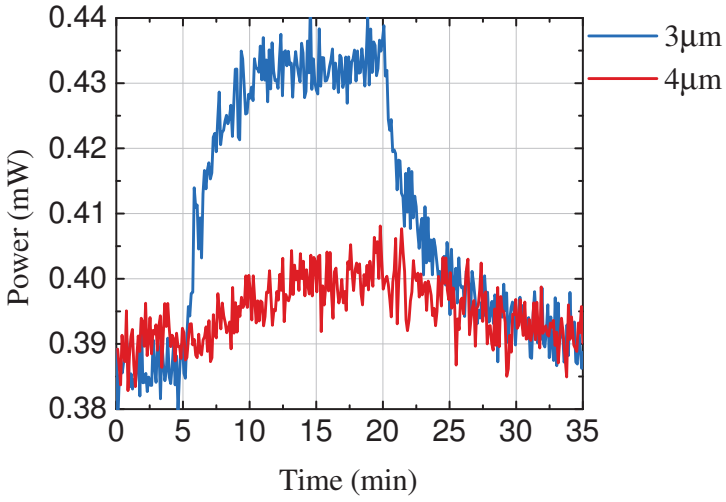

Figure 2.17: H_2 pulse measurements at 20°C for the 3 μm ridge width and 4 μm ridge width sensors showing the effect of ridge width on response time and power shift.

2.6 Discussion

It is clear that these devices are capable of detecting H_2 concentrations well below the LEL. This demonstrates that a simple, well-established semiconductor laser structure can be easily and inexpensively functionalized for applications in H_2 detection with adequate sensitivities and response times for fuel cell leak detection.

The laser output power measurements show a shift in response to H_2 as would be expected from the simulation results; however, the experimentally measured wavelength shift does not fully agree. Although the direction of the wavelength shift is in agreement with the simulation results, the magnitude is significantly smaller. This is likely due to a combination of three factors. First, the derivation for the predicted wavelength shift from (2.11) describes the redshift of all modes of the laser. The gain peak also experiences a redshift for lower threshold carrier densities due to H_2 exposure as predicted in Fig. 2.4(b). The mode that aligns closest to the gain peak after exposure is not necessarily the same mode that was aligned previously. Second, as shown in Fig. 2.7(c), the wet etch that forms the ridges undercuts on each side of the ridge, and the contact metal that masked the etch shadows the Pd deposition. This causes less overlap between the mode and the Pd film,

leading to reduced sensitivity. Third, accurate values for the refractive index of Pd before and after H_2 exposure at a wavelength of 980 nm for the same deposition and annealing conditions of this film are not available.

In order to fully enhance the wavelength shift in response to H_2 concentration, it has been suggested to pursue a single-mode EEL, which would prevent the mode-hopping effects that are believed to reduce the measured wavelength shift in this multi-mode EEL. Additionally, considering a plasma-enhanced dry etch as opposed to the phosphoric acid wet etch would prevent the sidewall undercutting. The results that will be presented in Chapter 3 for the photonic crystal vertically-emitting laser sensor further suggest that a single-mode laser can produce superior wavelength measurements for H_2 detection. Therefore, enhancements to this presented design to enable single-mode operation of an EEL geometry are pursued in Chapters 4 and 5 for the distributed Bragg reflector and distributed feedback lasers.

Though it should be noted that if wavelength measurements are not the desired detection technique for a specific application, this ridge-waveguide EEL structure still produces sufficient power measurements, and is a considerably simpler structure to fabricate. Additionally, even though the wavelength shift can be unpredictable and difficult to control due to mode-hopping, the measured spectra for the 3 μm device in Fig. 2.9 and Fig. 2.12(a) still show a peak wavelength redshift of approximately 51 pm per percent H_2, with a total wavelength shift of 88 pm at 2% H_2. Although these values are significantly smaller than the predicted shift from the simulation results, they may still be sufficiently accurate depending on the implementation.

CHAPTER 3

PHOTONIC CRYSTAL VERTICAL-CAVITY SURFACE-EMITTING LASER SENSOR

Unlike the previous edge-emitting laser design, which produces light output from two cleaved end facets of a horizontal cavity, vertical-cavity surface-emitting lasers (VCSELs) provide light output orthogonal to the surface of the sample. Surface-emitting semiconductor lasers are used in many applications and have advantages over edge-emitting lasers such as the ability to non-destructively probe and test devices during fabrication without having to package first, the capability of producing dense two-dimensional laser arrays, the ease of coupling to optical fibers due to the circular geometry and low divergence circular beam, lower threshold current due to the reduced cavity volume, and are no longer required to be lapped, polished, and cleaved [47–50]. These advantages, coupled with the VCSEL's compatibility with standard fabrication technologies, has enabled high volume, low-cost manufacturing.

The VCSEL design uses two distributed Bragg reflectors (DBRs) formed by a stack of repeating, epitaxially-grown layers with contrasting refractive indices such that the thickness of each layer is equal to $\lambda/4n$, with λ as the designed operating wavelength, and n as the refractive index of the layer. The DBR formed by this stack serves as a high reflectivity mirror which reflects light only at the design wavelength. The active gain layers are placed between the two DBRs such that they are spatially aligned near the peak of the longitudinal standing wave pattern formed in the micro-cavity between the DBRs.

A photonic crystal (PhC) is a material in which a periodic arrangement of refractive index variations, such as etched air holes in a semiconductor substrate, form a photonic band gap. This structure is analogous to a crystalline semiconductor in which a periodic arrangement of electrons form an electronic band gap. Defects in the photonic crystal structure, such as a missing air hole in an otherwise uniformly arranged series of air holes, form

an optical cavity with resonant frequencies located within the photonic band gap.

VCSELs with two-dimensional PhCs integrated on the top surface using periodically etched air holes have exhibited single-mode operation at a variety of operating wavelengths [51–55]. This single mode behavior in PhC VCSELs is useful for applications including optical communications [56], short-range optical interconnects [57], and optical storage [58].

The verified operating principle behind the EEL H_2 sensor is that the Pd film can be integrated into the device design such that there is a large overlap between the film and the optical mode, and that this film is exposed to the ambient environment. Additionally, as the experimental results demonstrated, a single-peak lasing spectrum is necessary to detect H_2 concentration as a function of laser wavelength. The PhC VCSEL provides a naturally single-mode device template in which the bottom of the etched holes are, like the trenches of the EEL sensor, exposed to the atmosphere and have a strong overlap with the optical mode.

The effective mode index of the PhC depends on the nature of the etched holes in the top DBR. Since modal confinement and top DBR reflectivity depend critically on the refractive indices and loss of the PhC material and the air within the etched holes, depositing a sensitive material such as Pd into these holes should enable the adaptation of this PhC VCSEL design for H_2 sensing applications.

Additionally, due to the lossy nature of the Pd film, and the field profile of the optical mode contained within the PhC defect, it was believed that the placement of Pd inside the etched air holes would help to improve the side mode suppression ratio (SMSR) of the already single-mode VCSEL. As mentioned before, the single-mode nature of the PhC VCSEL is crucial to accurate wavelength measurements; therefore, in addition to the change in optical properties of the Pd film, the performance of the sensor is further improved due to the enhancement in the single-mode nature of the PhC VCSEL. A full discussion of this concept, along with theoretical and experimental results is presented in Appendix C.

PhC VCSELs with a thin layer of Pd deposited on the top DBR were first fabricated and tested, and their experimental results were presented, demonstrating the effective use of this type of device as a hydrogen sensor [59]. Further work was then performed to model the PhC VCSEL structure

and simulate an estimated shift in wavelength, and additional experimental results were carried out to compare the PhC VCSEL sensor to a non-PhC VCSEL control sample with a thin layer of Pd deposited on the top DBR [60]. First, the simulation results will be presented with the theoretical wavelength shift, and then the full experimental results including a comparison with the control VCSEL will be provided.

3.1 Device Structure

A diagram of the PhC VCSEL used for this research is shown in Fig. 3.1, and a cross-section view of the entire layer structure is shown in Fig. 3.2. Not all of the exact details of the experimentally-measured VCSELs are known, so the following device structure, which was used for simulation purposes, is inspired by a combination of the known details of the fabricated devices and standard values used for VCSELs of similar design. The DBRs consist of alternating layers of $Al_{0.15}Ga_{0.85}As$ and $Al_{0.90}Ga_{0.10}As$, with 24.5 pairs in the top DBR, and 34.5 pairs in the bottom DBR. Between these reflectors is a high Al concentration AlGaAs layer ($Al_{0.98}Ga_{0.02}AS$), which is used to form an oxide aperture that helps confine the optical mode. The active region consists of 3 GaAs QWs separated by $Al_{0.3}Ga_{0.7}As$ barriers designed to lase at a wavelength of 850 nm, and padded with $Al_{0.6}Ga_{0.4}As$ spacers to help align the active region to a peak of the longitudinal standing wave.

3.2 Simulation Methods

There are a variety of methods that have been used to model PhC VCSELs with varying degrees of accuracy [61–63]. Here, the electric and magnetic field profiles for the PhC structure were calculated using the finite element method (FEM) in COMSOL Multiphysics, and mode-matching techniques were used in MATLAB to convert these results into reflection and transmission coefficients at each interface. The modeling was done by considering each layer of the DBR as a separate two-dimensional domain. A top-down view of one of the two-dimensional layers showing the PhC structure and the normalized electric field is provided in Fig. 3.3.

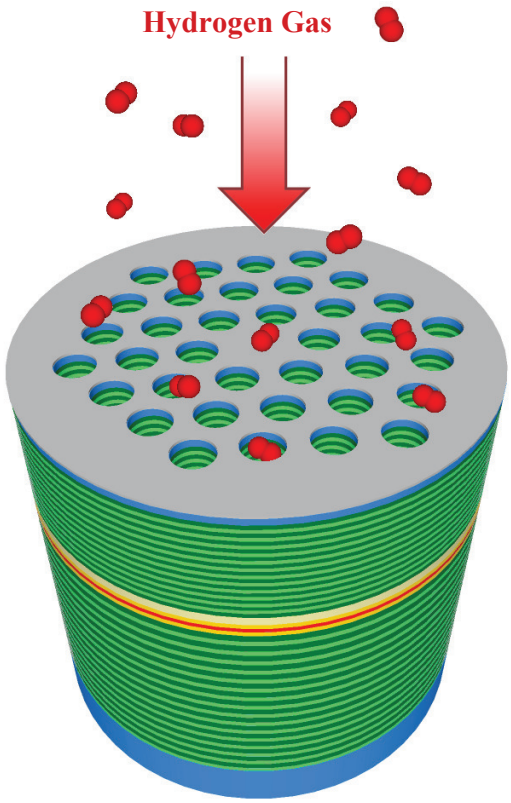

Figure 3.1: Illustration of the photonic crystal vertical-cavity surface-emitting laser H_2 sensor.

The top-most layer of the upper DBR is a 10 nm sheet of Pd with periodic air holes, and is defined by the Pd deposited on the surface of the device that did not fall into the etched holes. Since, as shown in Fig. 3.3, the dominant mode of the PhC VCSEL is centered almost entirely in the center defect of the PhC, this layer is modeled as a consistent, solid layer of Pd. This layer was simulated as the Pd without any H_2 influence and then again as the PdH_x after exposure with 4% H_2 in N_2. The rest of the top DBR is comprised of two alternating concentrations of AlGaAs ($Al_{0.15}Ga_{0.85}As$ and $Al_{0.90}Ga_{0.10}As$), with a hexagonally ordered set of air holes surrounding a defect in the center. The refractive index data for these layers at a wavelength of 850 nm (the lasing wavelength of the VCSEL) are $n = 3.5298$ for the $Al_{0.15}Ga_{0.85}As$ layer and $n = 3.0627$ for the $Al_{0.90}Ga_{0.10}As$ layer [64]. The air holes are etched 80% of the way through the top 24.5 pair DBR, and at the bottom of these air holes is a 10 nm layer of Pd. For the modeling of this particular 10 nm-thick cross-section, the same two-dimensional PhC model

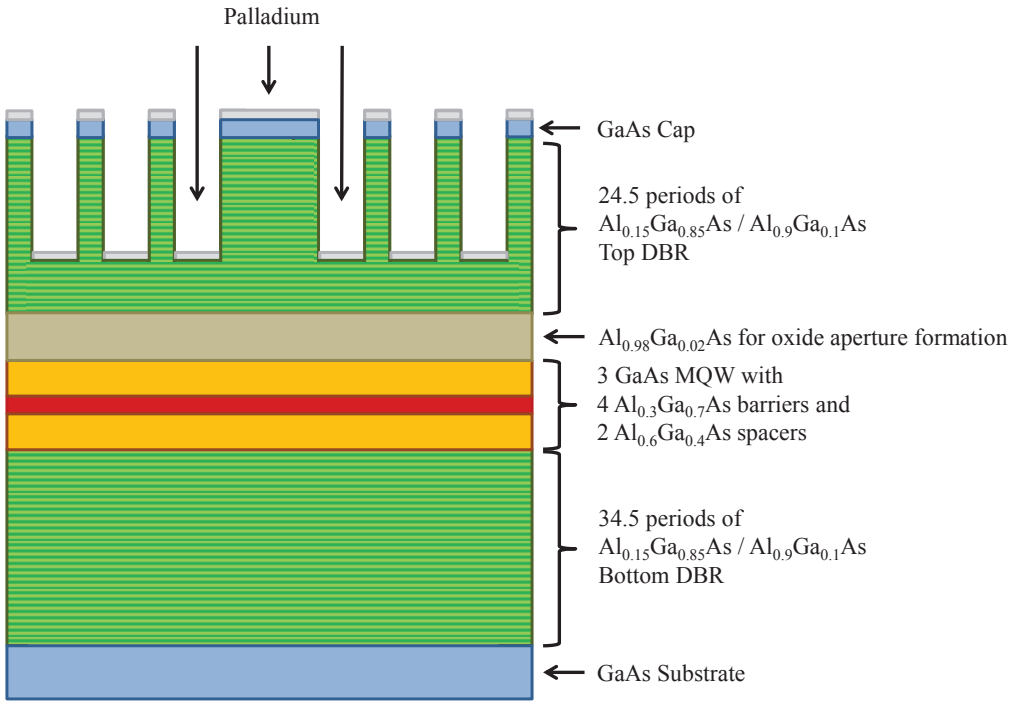

Figure 3.2: Cross-section view of the layer structure through the center of the PhC pattern.

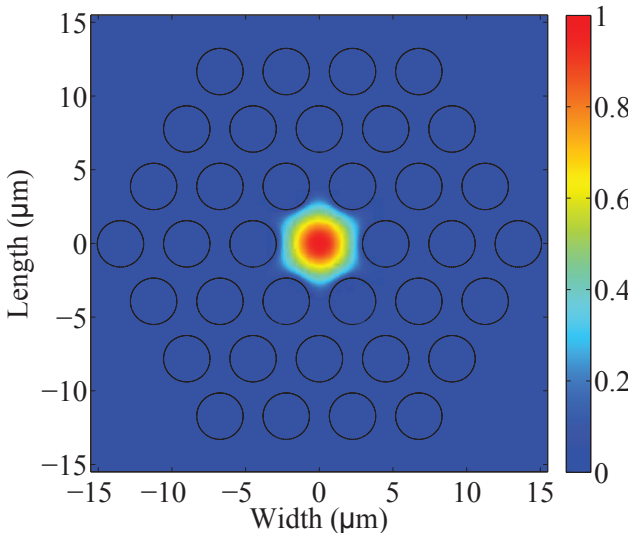

Figure 3.3: Top-down view of the PhC structure with the normalized electric field for the modeled PhC VCSEL.

is used; however, the air holes are replaced with solid Pd discs. Simulations were also done for both with and without H_2. The refractive indices for Pd with and without H_2 are the same as those used for the EEL sensors, taken

from [46]. Underneath the air holes is the remaining 20% of the top DBR, and is comprised of solid layers of alternating AlGaAs concentrations.

After using COMSOL to produce the electric and magnetic field components for each of the two-dimensional domains, mode matching is performed at the interface between each layer, and optical coefficients are calculated for the entire DBR using the transmission matrix method (TMM) as described in [65]. The mode matching is done by first normalizing the fields for each layer such that the electric and magnetic field components satisfy the relation

$$\frac{1}{2}\int(\mathbf{E_1}\times\mathbf{H_1})\cdot\hat{z}\mathrm{d}S=\frac{1}{2}\int(\mathbf{E_2}\times\mathbf{H_2})\cdot\hat{z}\mathrm{d}S=1 \tag{3.1}$$

Then, the transmission matrix components at the interface of these two layers are determined by

$$T_{11}=T_{22}=\frac{1}{4}\int(\mathbf{E_2}\times\mathbf{H_1}+\mathbf{E_1}\times\mathbf{H_2})\cdot\hat{z}\mathrm{d}S \tag{3.2a}$$

$$T_{12}=T_{21}=\frac{1}{4}\int(\mathbf{E_2}\times\mathbf{H_1}-\mathbf{E_1}\times\mathbf{H_2})\cdot\hat{z}\mathrm{d}S \tag{3.2b}$$

It should be noted that these equations only take the first-order mode into consideration. In order to calculate the full transmission coefficients, the integral must be performed over all existing modes. However, assuming that the PhC VCSEL operates as a single mode device as it is designed, this approximation is valid.

The top DBR is treated as four distinct sections. The top-most section is the solid Pd layer. The next section includes 19 pairs of alternating AlGaAs concentrations with the PhC holes etched through. The transmission matrix for this section is computed by using the propagation constant for each section determined in COMSOL to calculate the propagation matrices, and the mode-matching technique to calculate the interface transmission matrices between each layer. All of these matrices are then multiplied together to produce a transmission matrix for this element of the top DBR. The next section contains the single layer where the Pd at the bottom of the etched holes is located. The transmission matrix for this layer is again computed using the mode matching technique using the COMSOL models with the Pd discs instead of the air holes. Finally, for the top DBR, the remaining 4.5 periods are solid AlGaAs layers, and are computed using the traditional transmis-

sion matrix technique for DBRs without the need for mode matching. The transmission matrix for propagation through a layer is given by

$$T = \begin{bmatrix} e^{j\beta L} & 0 \\ 0 & e^{-j\beta L} \end{bmatrix} \tag{3.3}$$

where the propagation constant β is defined by the refractive index of the material at the design wavelength. The two air interfaces at each of the cleaved facets are modeled according to

$$T = \frac{1}{t_{12}} \begin{bmatrix} 1 & r_{12} \\ r_{12} & r_{12}^2 + t_{12}^2 \end{bmatrix} \tag{3.4}$$

with

$$r_{12} = \frac{n_1 - n_2}{n_1 + n_2} \tag{3.5a}$$

$$t_{12} = 2\frac{\sqrt{n_1 \times n_2}}{n_1 + n_2} \tag{3.5b}$$

where n_1 and n_2 represent the refractive indices of adjacent layers.

The transmission matrices are then multiplied together to produce an overall transmission matrix for the top mirror. The entirety of the bottom DBR is computed using the traditional transmission matrix technique since the entire bottom DBR consists of simple, un-patterned layers. The reflection coefficient of the two mirrors can be easily determined from the final transmission matrices as T_{21}/T_{11}, with T_{21} and T_{11} as defined by (3.2). The reflectivity of the top DBR is dependent on the Pd refractive index, so when H_2 is added to the system, the reflectivity and phase of the top DBR will change, which will produce a shift in the wavelength to maintain the gain and the phase conditions for lasing. The complex resonant wavelength of the VCSEL structure can be used to determine the photon lifetime as in (3.6a), which can then be used to determine the mirror loss as in (3.6b), which is used to determine the threshold gain.

$$\tau_{photon} = \frac{1}{2\,\omega_i} \tag{3.6a}$$

$$\alpha_m = \frac{1}{c \cdot \tau_{photon}} \tag{3.6b}$$

The effective indices for the top DBR PhC layers with air holes are $n = 3.5284$ for the $Al_{0.15}Ga_{0.85}As$ layer and $n = 3.0610$ for the $Al_{0.90}Ga_{0.10}As$ layer. Since the mode is contained almost entirely within the defect, the refractive index of the air holes contributes very little to the effective index. Therefore, these effective index values are very close to the refractive indices of the solid layers. The bottom of the etched air holes is located within one of the $Al_{0.90}Ga_{0.10}As$ layers. Therefore, the $Al_{0.90}Ga_{0.10}As$ PhC layer with Pd discs instead of air holes is simulated with and without H_2. The effective index of this layer without H_2 yields $n = 3.0610$ and $\kappa = 3.8547 \times 10^{-5}$. With 4% H_2, the effective index is $n = 3.0610$ and $\kappa = 3.2315 \times 10^{-5}$. The real components of these effective indices are nearly identical and are very close to the $Al_{0.90}Ga_{0.10}As$ refractive index. The imaginary component, however, experiences a noticeable shift when in the presence of H_2.

A shifts in both the reflection amplitude and phase are observed when H_2 is introduced. This shift in reflection amplitude impacts the mirror loss of the device, which in turn shifts the threshold gain. For 3 GaAs multiple quantum wells (MQWs) surrounded by $Al_{0.3}Ga_{0.7}As$ barriers designed to lase at 850 nm, the gain curves for various carrier densities were computed at 330 K, the expected temperature of the active region at threshold under CW operation. Using the mirror loss for the cases with and without H_2, threshold gain coefficients are computed for these cases. For GaAs active material, the refractive index decreases with carrier density as $\mathrm{d}n/\mathrm{d}N = -1.0 \times 10^{-20}$ cm^3 [66]. The shift in carrier density of the QW changes the optical path length of the cavity. This shift adds to the phase shift in the top DBR's reflectivity and produces a redshift in the peak wavelength when H_2 is added. The gain spectrum was computed using SimuLase at several carrier densities and the gain and phase conditions were iteratively solved to determine the lasing wavelength and threshold carrier density. The gain spectrum at threshold for 0% and 4% H_2 is shown in Fig. 3.4.

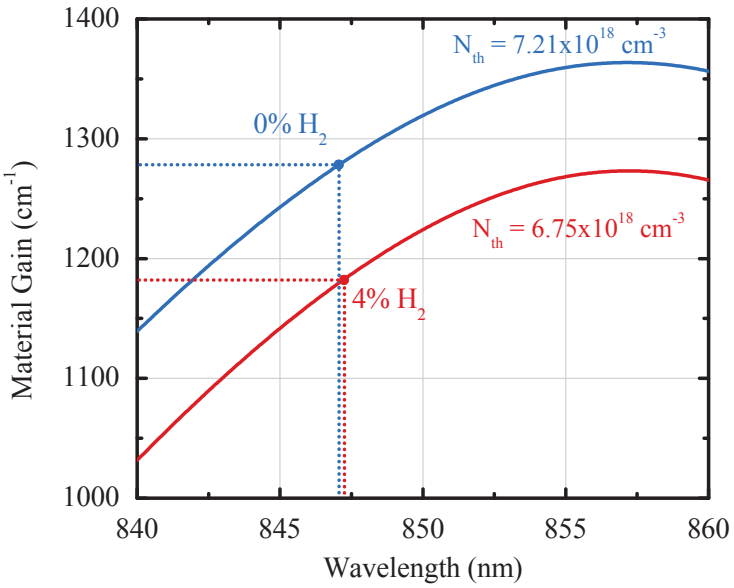

Figure 3.4: PhC VCSEL structure material gain curves for the two necessary carrier concentrations for threshold gain before and after exposure to 4% H_2. The threshold gain and lasing wavelength are indicated by the dotted lines.

3.3 Simulation Results

After performing the calculations on the full structure, an expected peak wavelength shift of 21.6 pm was found for 4% H_2 in N_2. Table 3.1 shows this and the other results from the simulation. As shown, the top DBR reflectivity increases when exposed to H_2, which decreases the mirror loss, and leads to a redshift in the peak wavelength.

Table 3.1: Simulation results for the photonic crystal vertical-cavity surface-emitting laser sensors

Parameter	**Symbol**	**Value**
Top DBR Reflectivity (0% H_2)	R_1	99.67%
Top DBR Reflectivity (4% H_2)	R_1	99.72%
Bottom DBR Reflectivity	R_2	99.98%
Top DBR Phase (0% H_2)	$\angle R_1$	π - 0.0758
Top DBR Phase (4% H_2)	$\angle R_1$	π - 0.0750
Bottom DBR Phase	$\angle R_2$	π - 0.0703
Mirror Loss (0% H_2)	α_m	22.8 cm^{-1}
Mirror Loss (4% H_2)	α_m	20.4 cm^{-1}
Optical Confinement Factor	Γ	0.02565
Carrier Density (0% H_2)	N	7.21×10^{18} cm^{-3}
Carrier Density (4% H_2)	N	6.75×10^{18} cm^{-3}
Total Wavelength Shift	$\Delta\lambda$	21.6 pm

3.4 Experimental Measurements

The PhC VCSEL was grown using metal-organic vapor phase epitaxy (MOVPE) for lasing near 850 nm. The PhC was patterned using photolithography and was etched through 80% of the top DBR using inductively coupled plasma (ICP) reactive ion etching (RIE). A detailed description of the geometry, fabrication, and testing of the non-functionalized devices can be found in [51]. After the VCSEL was fully fabricated and packaged, a 10 nm layer of Pd was deposited, allowing the Pd to be located at the top surface of the device as well as on the bottom of the etched air holes. As a control, another VCSEL of the same material and dimensions without the etched PhC was fabricated,

and a layer of Pd was deposited on the top surface of its DBR. It was believed that the Pd at the bottom of the etched air holes of the PhC VCSEL should allow for a more significant overlap between the resonant mode and the Pd film, which would produce greater shifts in the output power and peak wavelength. Additionally, the single mode behavior from the PhC VCSEL was predicted to make shifts in the peak wavelength more noticeable. The control sample allows determination of what impact, if any, the surface coating of Pd on the top of the DBR has on the device's sensing properties.

The sensor was measured by sealing the VCSEL within the custom-machined polycarbonate chamber. The leads of the packaged VCSEL were soldered to the printed circuit board with traces connecting to contact pads outside of the chamber. The light output from the VCSEL is coupled onto a fiber external to the chamber, which leads to the OSA. During the measurements, a steady stream of 5000 sccm of N_2 is flowed, and small concentrations of H_2 are turned on and off as desired to monitor the change in optical properties. Output power is measured by integrating the measured spectrum from the OSA. Since the collection lens is located outside of the testing chamber, the sample cannot be properly positioned at its appropriate focal point. Therefore, the magnitude of the power measurements were quite small. For comparison between the two samples, the data for the power measurements were normalized to unity at a current of 20 mA.

Initially, the laser spectrum was measured and the output power calculated as the current was increased, producing L-I curves for both a purely N_2 ambient, and an ambient containing trace amounts of H_2. Figure 3.5 shows L-I curves for the PhC VCSEL and standard VCSEL before and after being soaked in 4% H_2 for an hour. Five runs were collected and averaged to check repeatability and determine error bars.

As shown, the PhC VCSEL experiences a statistically significant increase in output power and lasing efficiency after being exposed to H_2 while the standard VCSEL shows no noticeable change. Additionally, spectra were collected for both of these devices under exposures to a variety of H_2 concentrations. As shown in Fig. 3.5 for the PhC VCSEL with injection currents between 15–19 mA, the output power after being exposed to H_2 is larger than the power before being exposed to H_2. The largest fractional power shift occurs near threshold. At 15 mA, a 60% power increase is observed for 4% H_2. However, at 20 mA injection current, the power drops with H_2.

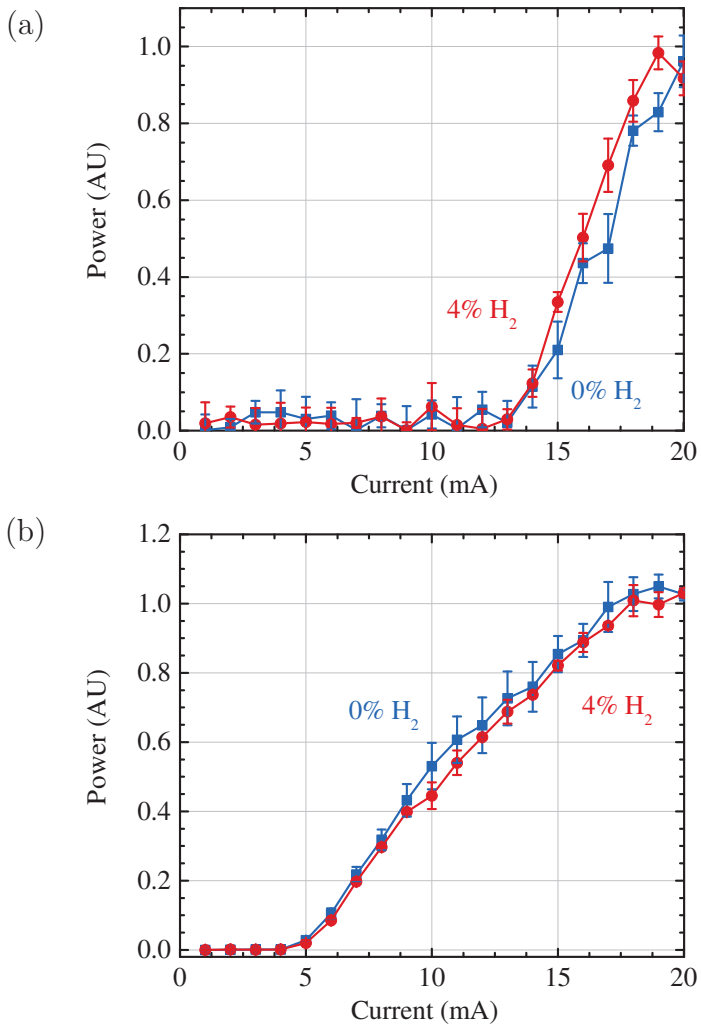

Figure 3.5: L-I curves before and after soaking in 4% H_2 for an hour for the (a) PhC VCSEL, and (b) standard VCSEL.

Thus, we investigate the output spectra in Fig. 3.6 at 15 mA and 20 mA after soaking the sensor in various H_2 concentrations for one hour each. The PhC VCSEL shows a single-mode peak that redshifts by an almost constant amount for each increase of H_2 concentration, while the standard VCSEL shows multi-mode behavior with no discernible shift after H_2 exposure. Additionally, the PhC VCSEL spectra at 20 mA injection current follows the same trend regarding the output power as shown in Fig. 3.5.

Figure 3.7 shows how the peak wavelength shifts as a function of injection current before and after H_2 exposure. The 130 pm/mA redshift seen in both devices is attributed to device heating. For the PhC VCSEL, there is a consistent redshift in peak wavelength with H_2 concentration for all injection

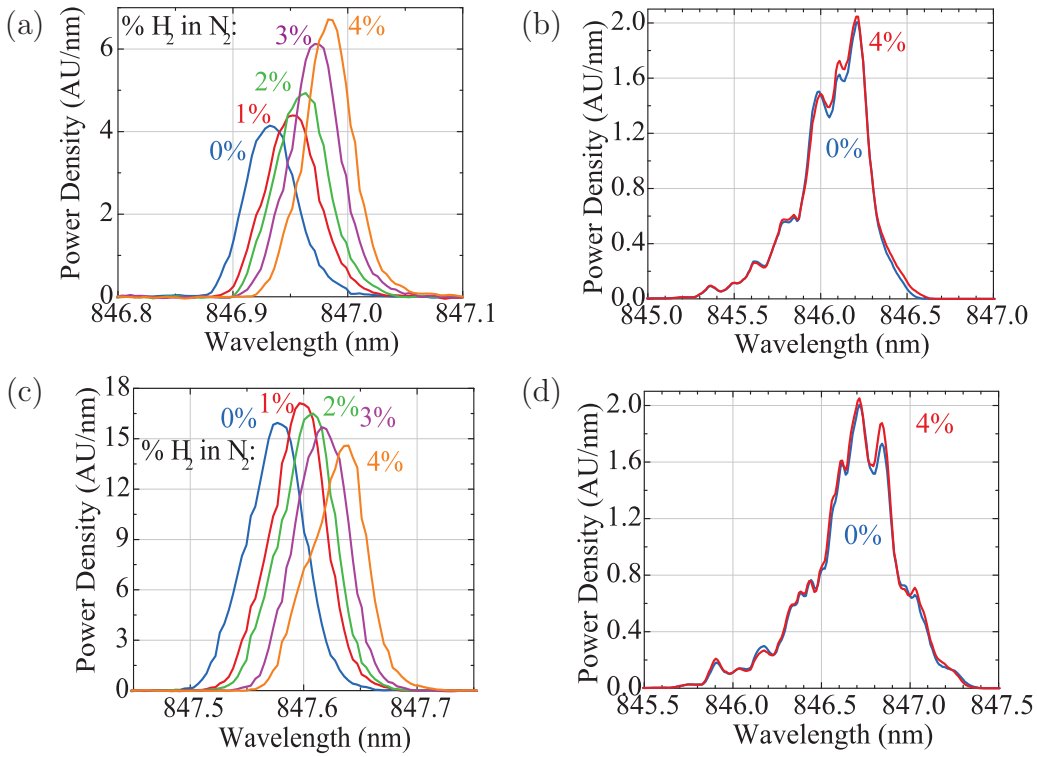

Figure 3.6: Sensor spectra after soaking in various H_2 concentrations for an hour each at 15 mA injection current for (a) the PhC VCSEL, and (b) the standard VCSEL, and 20 mA injection current for (c) the PhC VCSEL, and (d) the standard VCSEL.

currents. The run to run variation in the wavelength at fixed current and H_2 concentration for the PhC VCSEL is 2 pm, which is very small compared to the 52 pm wavelength shift for 4% H_2. However, for the standard VCSEL, the two curves overlap, showing no significant shift in the peak wavelength for any injection current.

Next, time dependent H_2 pulse measurements were performed to observe the response and recovery time for the devices as they are injected with a constant current of 19 mA, where the absolute power shift is greatest. Both the output power and the spectrum were observed as varying concentrations of H_2 were pulsed on and off. The results from this study are shown in Fig. 3.8 and Fig. 3.9. For the PhC VCSEL, both power and wavelength begin to shift immediately as the H_2 is pulsed on and off, and typically takes about 2–5 minutes to fully saturate, depending on H_2 concentration. Additionally, the magnitude of the response scales with H_2 concentration, allowing for the concentration to be approximated by either the power or wavelength shift.

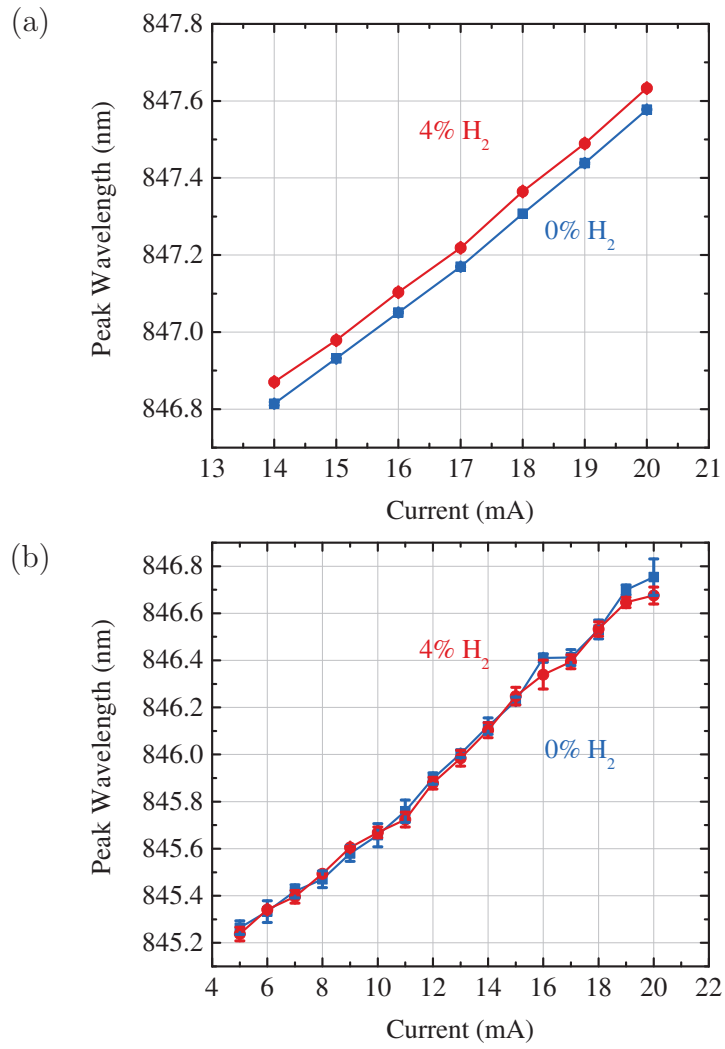

Figure 3.7: Peak wavelength as a function of injection current for the (a) PhC VCSEL, and (b) standard VCSEL.

The standard VCSEL, however, shows no noticeable shift in either power or wavelength when exposed to H_2. The power measurement just shows steady noise while the wavelength measurement reveals mode-hopping.

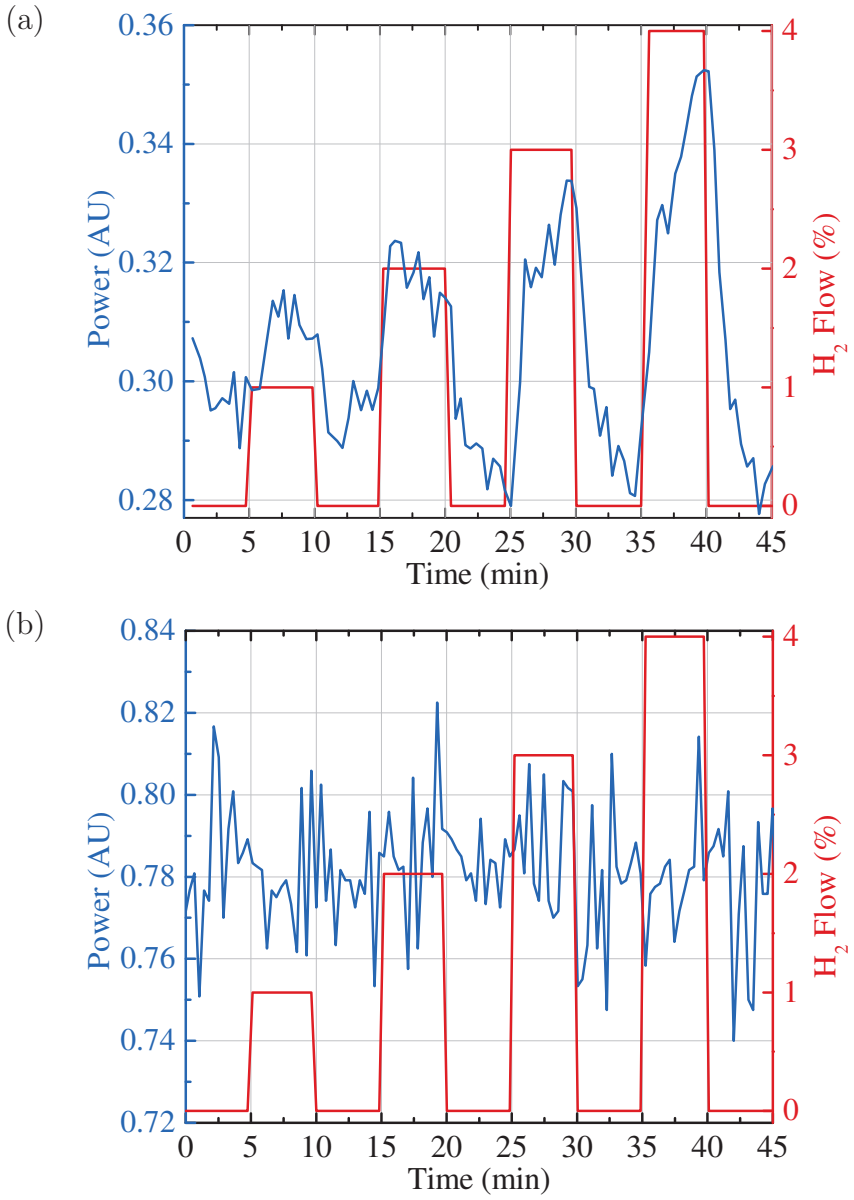

Figure 3.8: H_2 pulse measurements of the output power for the (a) PhC VCSEL, and (b) standard VCSEL.

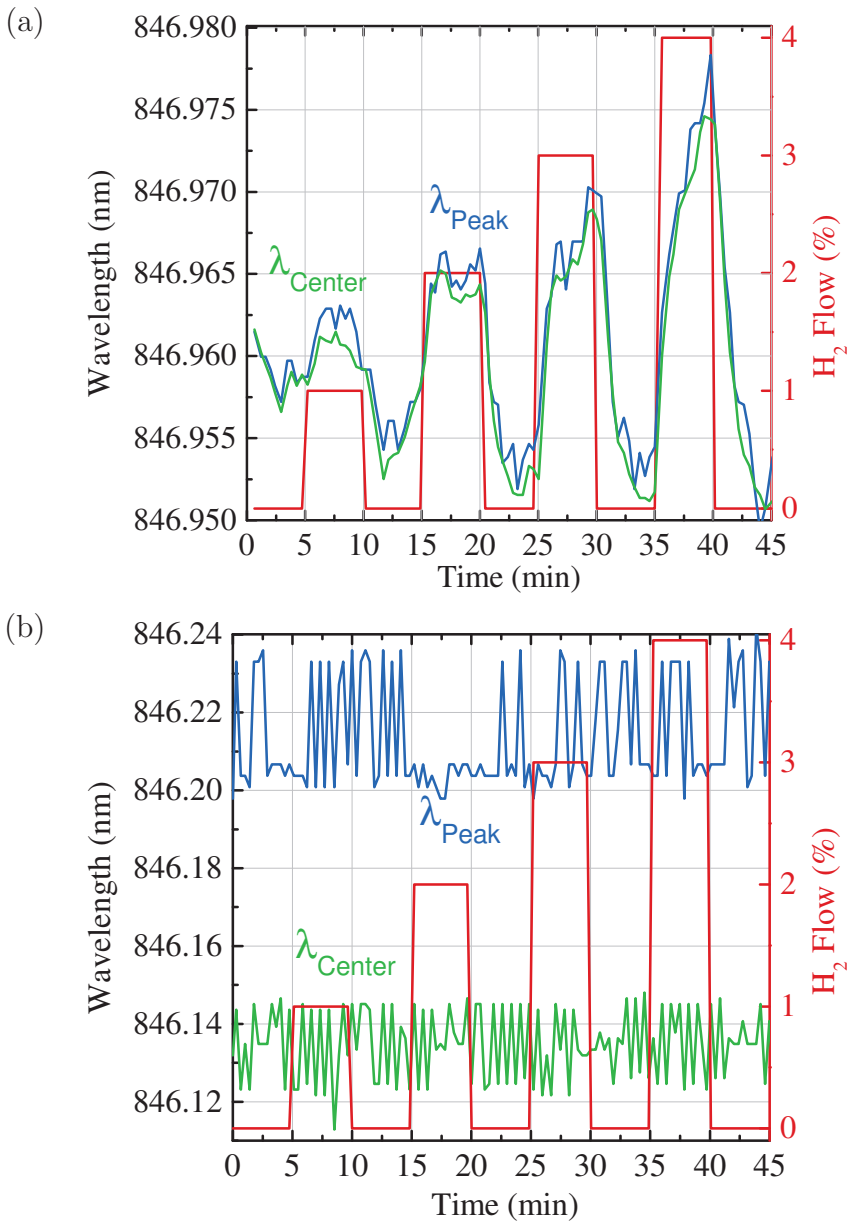

Figure 3.9: H_2 pulse measurements of the peak wavelength and FWHM center for the (a) PhC VCSEL, and (b) standard VCSEL.

3.5 Discussion

From the simulation, two primary effects determine the theoretical wavelength shift. Since the device's lasing wavelength is determined by the gain and phase conditions, any shift in round trip gain or phase with the addition of H_2 can lead to a wavelength shift. The phase condition depends on the phases of the top DBR, the bottom DBR, and the cavity. This condition is met when the sum of these three phases is equal to an integer multiple of 2π. Since the bottom DBR's reflectivity and phase do not depend directly on the H_2 concentration due to the lack of Pd integration, the phase in the top DBR and cavity are of the most importance. It should be noted that as the lasing wavelength shifts due to the H_2 presence, so too does the phase of the bottom DBR. As shown in Table 3.1, the phase of the top DBR increases when H_2 is added to the system. This effect alone is capable of producing a wavelength shift. Assuming that both the cavity phase and the bottom DBR phase are constant, the shift in the top DBR phase only yields a 2.5 pm redshift. However, the refractive index of the active material depends on the carrier density. Thus, the optical path length of the cavity depends on the reflectivity of the top and bottom DBRs, and so changing the reflectivity in the top DBR will impact the lasing wavelength produced from the gain condition. If the phase of the top and bottom DBRs are kept constant, and only the wavelength shift due to the change in optical path length of the cavity is considered, the lasing wavelength redshifts 18.6 pm. The total theoretical wavelength shift of 21.6 pm is due to both of these effects and their interaction; however, it is clear that the carrier density dependent refractive index of the active material is the more significant phenomenon.

The total wavelength shift from the simulation results is of the same order of as the experimental wavelength shift for the PhC VCSEL sensor. The experimental value for the shift at 4% H_2 was about 2.4 times larger than the value predicted from the simulation. This discrepancy is likely due to inaccuracies in the model parameters. In particular, the refractive index values of the Pd layer with and without H_2 are known to depend on the Pd thickness, porosity, and deposition conditions. The wavelength shift in the simulations is highly dependent on the Pd thickness and its refractive index shift after being introduced to H_2. If the model's refractive indices before and after H_2 exposure are inaccurate, or if the experimentally deposited thickness has any

variation, this will translate to significant alterations in the wavelength shift. Additionally, if the PhC holes are not etched perfectly straight, or if the experimentally deposited Pd is not deposited at exactly normal incidence, there will be a thin annular coating of Pd on the inside of the etched holes. Due to the very small penetration depth of the fundamental mode into the Pd holes, this very thin coating creates a much greater effective thickness of Pd within the PhC, which in turn causes a larger shift. Finally, from the experimental data, it is observed that as H_2 is introduced, the voltage across the device increases by an amount related to the H_2 concentration as the current is held constant. This suggests that as Pd absorbs H_2, the resistance of the device increases. The conductance of Pd films generally decreases with H_2 [67]. Thus, the resistance of the PhC VCSEL top contact increases since some current spreads along the top most Pd layer. At 4% H_2, the resistance increased by 0.3 Ω, which would heat the device by about 0.2 K and produce an additional redshift of about 5 pm. Small contributions from each of these potential inaccuracies can realistically explain the discrepancy between the theoretical and experimental models.

The wavelength and power shifts for the standard VCSEL were not visible for any concentration of H_2; however, the PhC VCSEL shows very noticeable changes. This is believed to be primarily a result of the single mode nature of the PhC VCSEL. The multi-mode spectrum for the standard VCSEL makes it difficult to distinguish any measurable shift, but the single peak for the single mode PhC VCSEL moves consistently with H_2 concentration. This is in good agreement with the results from the EEL sensor. Additionally, the Pd located at the bottom of the etched air holes in the PhC VCSEL contributes a small enhancement to the wavelength and power shifts. However, since most of the mode is concentrated in the PhC defect, only a very small portion of this mode overlaps the Pd in the holes.

As shown in Fig. 3.7, the peak wavelength shift for 4% H_2 appears to be independent of current. Therefore, a fit was performed on the peak wavelength shift, $\Delta\lambda$ (in pm) versus the H_2 concentration percentage with data taken at 0, 1, 2, 3, and 4% H_2 and currents of 14–20 mA. A power law, $\Delta\lambda = b\,(H_2\%)^c$ was used to capture the nonlinear behavior at low concentration. The fit produced $b = 19.4 \pm 1.1$ and $c = 0.727 \pm 0.050$. Additionally, a 95% prediction interval can be applied to this set of data yielding an estimate of the range of expected wavelength shifts for any specified concentration of

H_2. Using the Hubaux and Vos method [68], an approximate value for the minimum detection limit (MDL) of the sensor is found to be 0.8% hydrogen. This is calculated by finding the point in which the upper prediction limit intersects the y-axis, following this point horizontally to the lower prediction limit, and then proceeding vertically to the x-axis, which defines the MDL. The Hubaux and Vos method is typically applied to a linear regression; however, it is assumed that this method still produces a valid approximation for this nonlinear fit. The results from this fit and a graphical representation of how the MDL was calculated are shown in Fig. 3.10. This demonstrates that after calibration in a N_2 ambient, the peak wavelength shift can be used to accurately determine the H_2 concentration, independent of the sensor's injection current.

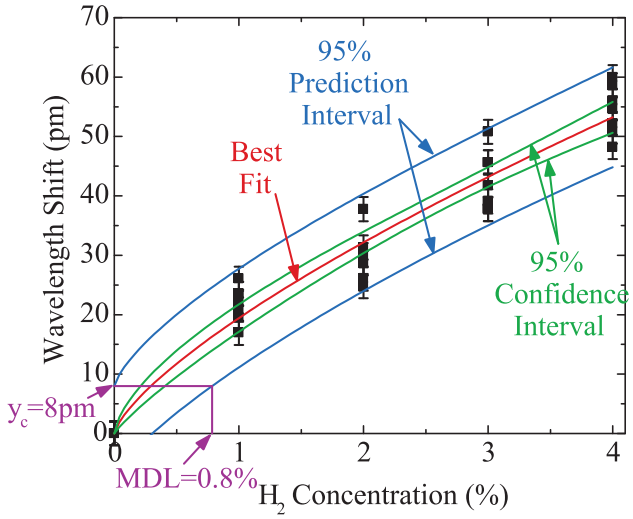

Figure 3.10: Fitting parameters for the wavelength shift of the PhC VCSEL sensor including an approximate MDL of 0.8% H_2.

In conclusion, this device that been shown to experimentally produce consistent, repeatable shifts in both output power and wavelength as a function of H_2 concentration. At 15 mA injection current, near threshold, the sensor produces an increase in output power of about 60% at 4% H_2. Additionally, the device produces a redshift in the peak wavelength independent of current of about 52 pm at 4% H_2. By comparing the PhC VCSEL sensor to a standard VCSEL with Pd deposited on the top surface, it has been determined that the single-mode nature of the PhC VCSEL is necessary to observe the H_2-induced changes in power and wavelength.

Although the wavelength redshift is smaller for the PhC VCSEL than for

the EEL sensor (by about a factor of 4), there are no issues with mode-hopping. The smaller wavelength shift is due to the decreased interaction length. For the EEL sensor, Pd coats the entire cavity length, so the optical mode is in constant overlap. For the PhC VCSEL, the only interaction regions are the 10 nm layer at the bottom of the etched air holes and the 10 nm layer on the top surface. Thicker layers of Pd inside the etched air holes should be pursued for the PhC VCSEL to increase the interaction length. Such a thin layer was chosen for this design because a blanket deposition was performed, so the Pd needed to be optically-thin on the top surface, or it would block all of the light from exiting. However, as the simulation results suggest, this Pd on the top facet makes a significant impact on the sensitivity of the PhC VCSEL. Therefore, some optimization is needed to keep an optically-thin layer of Pd on the top facet in the PhC detect region, but deposit a much thicker Pd layer into the etched air holes. This would add additional fabrication expenses and complications which may be undesirable, but would surely improve the sensitivity. However, depending on the specific implementation, the sensitivities presented for the 10 nm blanket deposition may very well be suitable.

CHAPTER 4

DISTRIBUTED BRAGG REFLECTOR LASER SENSOR

The ridge-waveguide edge-emitting laser is a simple, laterally-emitting design that shows sufficient power shifts in response to H_2 concentration; however, due to its multi-mode nature, the wavelength shifts are unpredictable due to mode-hopping. The EEL presented in Chapter 2 uses a simple Fabry-Pérot cavity with cleaved facets as mirror. Although these facets provide adequate reflection, they are wide-band, allowing them to reflect all wavelengths of light. Therefore, the lasing wavelength is a function of the many resonant wavelengths produced by the Fabry-Pérot cavity, and the gain spectrum of the quantum well. However, the PhC VCSEL presented in Chapter 3 uses distributed Bragg gratings (DBRs) to produce reflection at only the target wavelength. This, coupled with the strong confinement provided by the photonic crystal, provides the single-mode output. It is desired to use this same concept on an edge-emitting geometry to enable H_2 detection as a function of a single wavelength spectrum shift.

The DBR laser H_2 sensor is a direct analogue to the PhC VCSEL, only it emits in-plane rather than vertically. A ridge-waveguide structure is still used so that the Pd can be located close to the active region, only instead of a blanket coating, the Pd is deposited in thin strips at each end of the device with strip widths of $\lambda/4\,n_{eff}$, with λ being the design wavelength and n_{eff} being the effective refractive index of the waveguide. When the Pd interacts with the H_2, the refractive index of the Pd layer changes, which then changes the effective refractive index of the waveguide in those regions, detuning the DBR to a different target wavelength. This shift in wavelength can then be measured, and due to the single-mode nature of the DBR laser, there will be no issues with mode-hopping. Additionally, as the Pd forms PdH_x, the reflectivity on these mirrors will change, which like for the other laser designs, will shift the output power.

4.1 Device Design

The DBR edge-emitting laser sensor is similar in operation principle and structure to the ridge-waveguide EEL, except the Pd layer does not cover the entire area of the device. Instead, thin Pd strips are placed at each end of the ridge-waveguide structure, forming a DBR. When H_2 interacts with the Pd film, this detunes the DBRs and changes their reflectivities, resulting in both a wavelength and power shift of the laser output [69]. Additionally, the DBRs provide single-mode operation of the laser, which should provide similar wavelength measurement results as the PhC VCSEL, without the mode-hopping effects observed in the standard ridge-waveguide EEL sensor. The DBRs at each end of the ridge act as mirrors, and in most DBR lasers are used instead of the cleaved facet. However, due to the low reflectivity of the mirror formed by thin Pd strips alone due to a small effective index contrast, an impractically-long DBR would be necessary to provide adequate reflectivity for lasing. Therefore, at the end of each DBR there is a cleaved facet.

An illustration displaying the device structure is shown in Fig. 4.1. The device is formed by a resonant cavity sandwiched between two DBRs made of Pd strips and terminated by cleaved facets. The cavity length used is 1 mm, the length of each grating is 150 μm, and each grating contains 1000 periods. This laser structure is designed to operate at a wavelength of 980 nm, and the width of each Pd strip is equal to $\lambda/4n_{eff} = 75$ nm. The ridge width for the waveguide is 1 μm and the Pd thickness is 10 nm. The gain contact is used to electrically pump the device while the phase and grating contacts are used to tune the DBR reflection peaks. In the simulation, the effect of these tuning contacts is approximated by small adjustments to the cavity length, and the distance between the DBR and cleaved facet. Additionally, the figure shows a proposed insulating planarization layer on each side of the ridge in the cavity to provide a large contact pad area for probing and wire-bonding.

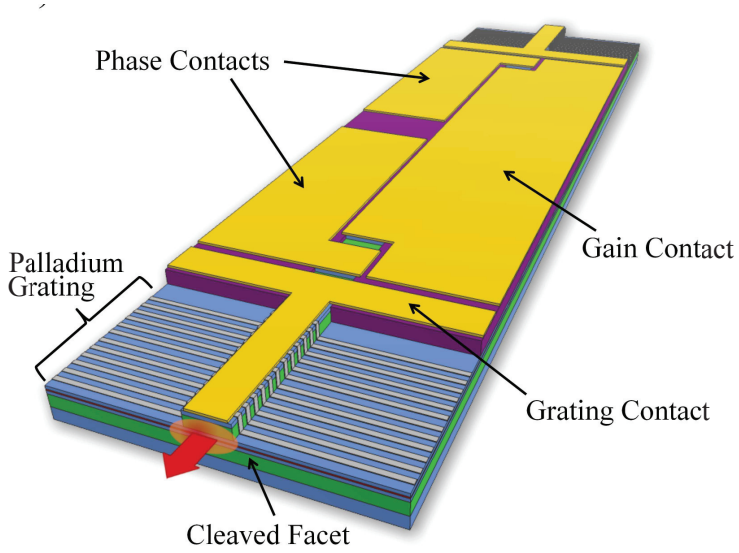

Figure 4.1: Illustration of the distributed Bragg reflector laser sensor.

4.2 Simulation Methods

Since this structure is similar in design to the ridge-waveguide EEL sensor, with DBR mirrors that are similar in concept to the PhC VCSEL sensor, the simulation method used here employs techniques developed for each of these previous structures. For the DBRs, the transmission matrix method (TMM) is used according to the same technique as for the PhC VCSEL sensor. For the electrical properties, the gain database that was used for the ridge-waveguide EEL sensor is used, due to the identical layer structure.

The first stage of the simulation is to determine an effective refractive index (n_{eff}) of the ridge-waveguide for the cases of no Pd, with Pd before exposure to H_2, and with Pd in the presence of H_2. This is performed by modeling each two-dimensional cross-section of the ridge-waveguide using FEM in COMSOL Multiphysics. Figure 4.2 shows a cross-section of the waveguide with the normalized electric field used to compute this effective index. Additionally, this FEM simulation provides values for the normalized group delay, τ_g, coupling coefficients, κ_s and κ_m, and the optical confinement factor, Γ, all used in later stages of the simulation.

The resonance condition for the device structure is simulated using the TMM, in which each uniform section is represented by an individual transmission matrix, and the entirety of the device is then described by cascading all of these individual transmission matrices. A two-dimensional simulation

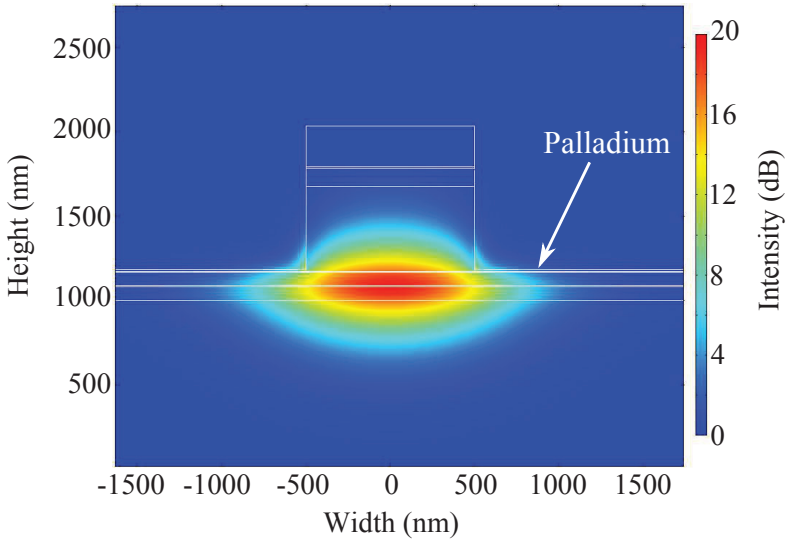

Figure 4.2: Profile of the normalized electric field for the DBR laser sensor showing its overlap with the Pd film.

was performed for this grating comparing the results of the transmission matrix method to an FEM simulation. Unfortunately, the traditional transmission matrix method based on the change in n_{eff} slightly exaggerates the reflection at the interface between the ridge without Pd and the ridge with Pd. This slight error would then be exacerbated as 2000 of these interface matrices are present for each grating. Therefore, in order to accurately represent the reflectivity of the grating, the coupled mode theory is used to generate a transmission matrix representing one full period. The transmission matrix is calculated using the method presented in [70] for curved waveguide structures by taking the limit as the radius of curvature approaches infinity. The values for τ_g, κ_s, and κ_m derived from the FEM simulation are used here. This matrix can then be successfully cascaded to represent the full grating. This methodology has been verified by computing the transmission matrix for a simplified two-dimensional grating using the coupled mode theory, and it has been confirmed that the results obtained using this technique agree with FEM results for the same structure. After using the traditional transmission matrix method for the cavity and cleaved facet interfaces, and the coupled mode theory for the gratings, a transmission matrix that describes the entire device is obtained.

4.3 Simulation Results

By analyzing the components of the device's transmission matrix, the resonant wavelength and mirror loss can be determined. With the addition of H_2, the resonant wavelength redshifts, yielding a total difference of 129.5 pm. Additionally, the reflection and transmission spectra of the DBR before and after exposure to H_2 can be derived, and are presented in Fig. 4.3. As shown, the reflection decreases and the transmission increases in the presence of H_2.

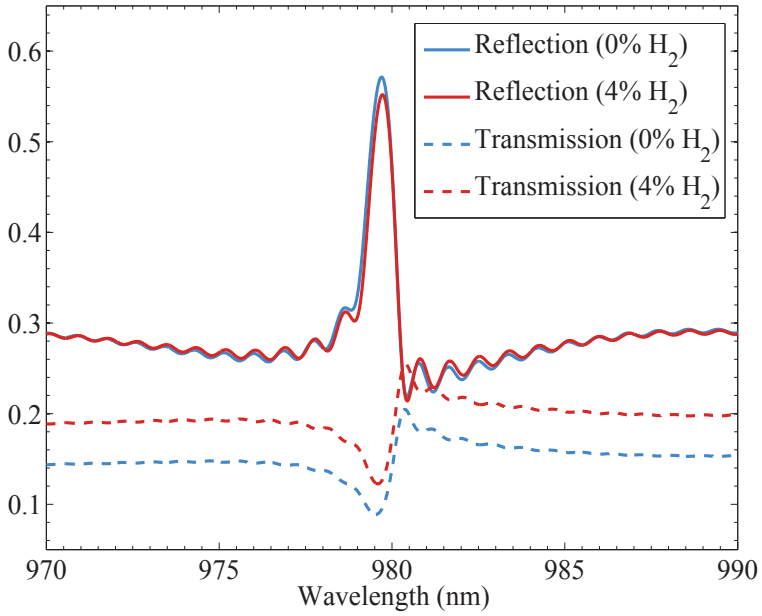

Figure 4.3: Simulated reflection and transmission spectra of the DBR before and after 4% H_2 exposure for the DBR laser sensor.

In addition to the shift in output wavelength, a shift in output power is also desirable. This is simulated by first computing the necessary threshold gains from the internal loss and mirror loss before and after H_2 exposure, and the optical confinement factor obtained from the FEM simulation. The mirror loss can be derived from the imaginary component of the complex resonant frequency given by the structure's transmission matrix. In the presence of H_2, the mirror loss decreases. After computing the threshold gains both before and after H_2 exposure, the threshold carrier densities are determined using the material database obtained from Nonlinear Control Strategies SimuLase that matches the material structure for this simulation. Next, a relationship between carrier density and threshold current for the device structure was

determined using RSoft LaserMOD. Using this relationship and the values for the threshold carrier densities, threshold currents are found for the cases of with and without H_2. Next, the differential efficiency that determines the slope of the L-I curve is derived using the calculated mirror losses, and typical values for internal loss, $\alpha_i = 5$ cm^{-1}, and internal efficiency, $\eta_i = 0.8$ are assumed. The full simulated L-I curve showing the output power as a function of injection current is shown in Fig. 4.4. A summary of the important calculated values for this structure in this simulation is provided in Table 4.1.

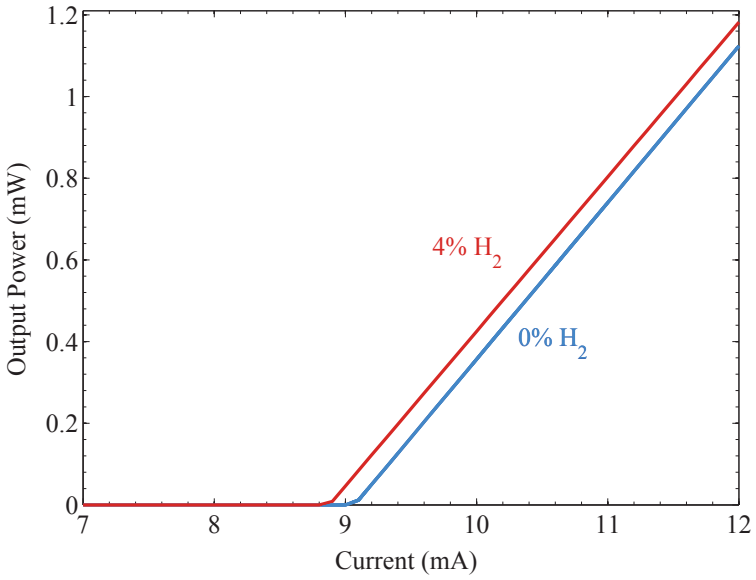

Figure 4.4: Simulated L-I curves for the DBR laser sensor before and after 4% H_2 exposure.

4.4 Discussion

Simulation results for a H_2 sensor utilizing thin strips of Pd periodically deposited near each facet of an edge-emitting laser to form a H_2-sensitive DBR have been presented. It is shown that this device is capable of producing measurable wavelength and power shifts near the lower explosive limit of H_2 in air. For a concentration of 4% H_2, the wavelength redshifts by 129.5 pm, and when biased near threshold, the power increases by 43%.

Although these values are suitable for detecting H_2 concentrations in the

Table 4.1: Simulation results for the distributed Bragg reflector laser H_2 sensors

Parameter	**Symbol**	**Value at 0% H_2**	**Value at 4% H_2**
DBR Reflectivity	R	57.14%	55.20%
Resonant Wavelength	λ	979.89 nm	980.02 nm
Mirror Loss	α_m	15.66 cm^{-1}	14.85 cm^{-1}
Threshold Gain	g_{th}	477.11 cm^{-1}	458.33 cm^{-1}
Threshold Current	I_{th}	9.07 mA	8.88 mA
Differential Efficiency	η_d	0.606	0.598
Wavelength Shift	$\Delta\lambda$	—	129.5 pm
Percent Power Shift (@ 9.5mA)	ΔP	—	43%

desired range, and would be able to operate in single-mode, the overall sensitivity is poorer than that of the standard ridge-waveguide EEL. The predicted wavelength shift is almost an order of magnitude smaller. This, like as was for the case of the PhC VCSEL, is due to the decreased interaction length. For the DBR laser, there is only Pd located in each of the deposited strips forming the DBR, so that the mode only interacts with the changing optical properties in these regions, while the standard ridge-waveguide EEL sensor has Pd everywhere on the cavity.

This device design was not fabricated. Due to the simulation results suggesting that the overall sensitivity would be poor, and the testing would be difficult due to having to separately modulate each of the contacts to enable lasing, a new device design was conceived that would theoretically yield higher sensitivities, and be much easier to test. This new sensor is based on a distributed feedback design, and is presented in Chapter 5. However, the DBR laser sensor does allow for mirror tuning by modulating the injection current into each of the gratings; therefore, there could be potential applications where that characteristic is beneficial for sensing.

CHAPTER 5

DISTRIBUTED FEEDBACK LASER SENSOR

The standard Fabry-Pérot laser uses cleaved facets for mirrors, which provide optical feedback to the system. The DBR laser replaces these hard mirrors with distributed mirrors designed to reflect at only a target wavelength. A distributed feedback (DFB) laser also uses gratings of contrasting refractive index, however, the gain is included in the gratings.

Since the periodicity of the DFB laser is the same as that of the DBR laser, such that each grating has a length of $\lambda/4\,n_{eff}$, it will produce a high reflectance at the grating's design wavelength. However, unlike the DBR laser, we are not interested in the reflection from this grating, but rather the transmission through it. Ordinarily, without gain, this structure would not be able to transmit light at the desired wavelengths; however, the reflectivity spectrum produces a series of peaks and nulls, with each null corresponding to a peak transmission. Therefore, as light propagates through the structure, it is constantly reflected at each of the grating surfaces, greatly slowing down the group velocity through the device, which increases the interaction time. This increased interaction time allows the wavelengths corresponding to nulls in the reflectivity spectrum to experience gain, and causes the DFB laser to emit light at the peaks of the transmission spectrum, which correspond to the band edges of the reflectivity [71].

There are many transmission peaks in this spectrum, but the ones closest to the design wavelength will have the slowest group velocity, and thus the largest amount of interaction with the gain medium. Therefore, as the gain is increased due to pumping injection current, the DFB laser will lase at the two transmission peaks closest to the grating's design wavelength. Ordinarily, this double-mode behavior is undesirable, so several methods have been used to break the degeneracy, with the most commonly-used being the placement of a $\lambda/2\,n_{eff}$ cavity in the center of the DFB. This cavity provides destructive interference for one of the modes, ensuring that the DFB laser operates with

only a single mode.

It was learned from the DBR laser sensor results that the interaction length with the Pd film needs to be kept as high as possible to maximize the sensitivity. Additionally, the Pd strips that formed the DBR did not provide adequate effective index contrast, and this caused the reflectivity of the mirrors to be very low, requiring cleaved facets. Finally, the DBR laser sensor had multiple contacts that all needed to be tuned, which would have made testing difficult. The DFB laser structure presented here alleviates all of these concerns. Like for the standard ridge-waveguide EEL, Pd is deposited on the entire cavity length of the DFB. The grating is formed using an apodization of the ridge-waveguide, providing an index contrast due to varying ridge widths, which provides a much larger index contrast. Finally, the DFB laser by its very nature only requires a single gain contact, as was the case for the standard ridge-waveguide EEL sensor. Essentially, this design is identical to the standard ridge-waveguide EEL, only an apodization of the ridge sidewalls causes it to lase in only a single mode, and the periodic interconnects to contact pads have been removed due to unwanted reflections that would interfere with the DFB grating reflectivity. Additionally, the simulation results suggest that the lossy nature of the Pd film breaks the degeneracy between the two DFB laser modes, eliminating the need for a $\lambda/2\,n_{eff}$ cavity.

5.1 Device Design

This device, shown in Fig. 5.1, is very similar to that of the ridge-waveguide EEL sensor. The layer structure for the material has been previously shown in Table 2.1, and the waveguide ridge has been etched down 600 nm to the core region. The ridge widths of this structure vary between 3 μm and 2.7 μm for each period (a 150 nm apodization on each side of the ridge). Based on the experimental results for the ridge-waveguide EEL laser sensors, the material lased at a wavelength of 988 nm, so the DFB grating was designed at this wavelength. The length of each section in the grating is equal to $\lambda/4\,n_{eff}$, which for $\lambda = 980$ nm, is 75 nm. The Pd layer was chosen to be 30 nm in thickness, and the total cavity length was chosen to be 500 μm. The simulated DFB laser sensor also assumes an anti-reflective coating on each of the facets to prevent unwanted reflections from Fabry-Pérot modes.

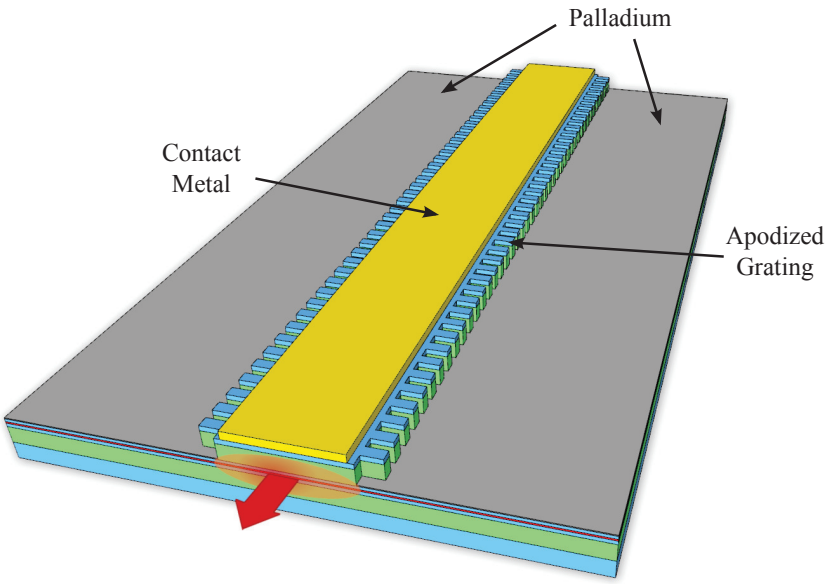

Figure 5.1: Illustration of the distributed feedback laser sensor.

5.2 Simulation Methods

The simulation method employed is the transmission matrix method (TMM) that was used for the PhC VCSEL sensor in Chapter 3.2. Calculations of the reflection for a single period of the grating were compared to a three-dimensional simulation of a single period, and it was confirmed that the TMM model produced sufficiently similar values. The effective index values were computed similarly to the ridge-waveguide EEL laser sensor using COMSOL Multiphysics for two dimensional cross-sections of the 3 μm and 2.7 μm ridge widths both before and after exposure to H_2. Since the transmission peak of the DFB structure is dependent on gain, values for the gain were added to the refractive indices produced by COMSOL, so the operation of the laser under various amounts of gain could be studied. The transmission matrices were then cascaded together to form a singular transmission matrix representing the entire structure, which was then used to compute the total transmission through the device.

The gain values were steadily increased until it was determined that the device had reached the threshold gain. The peaks of the transmission spectra at the threshold gain values predict the lasing wavelength of the device. This is performed for the cases of both before and after H_2 exposure, which produce a predicted wavelength shift in response to H_2. Next, from the

threshold gain values, both the mirror loss α_m and the loss due to the Pd layer $\alpha_{i,Pd}$ can be determined, which are used to produce the differential efficiency. Using the same SimuLase gain database as the ridge-waveguide EEL sensor, the threshold gain values are then used to determine the threshold carrier density, which is then used to calculate the threshold current. From the threshold current and differential efficiency, simulated L-I curves can be produced. All calculations were performed assuming an operating temperature of 20°C. The in-depth derivation of these values has been presented in Chapter 2.2

5.3 Simulation Results

Figure 5.2 shows the transmission as a function of wavelength for the DFB laser sensor for a variety of gain values. This shows how a DFB laser operates, and how the inclusion of gain due to pumping causes the band edges of the reflectivity spectrum to lase.

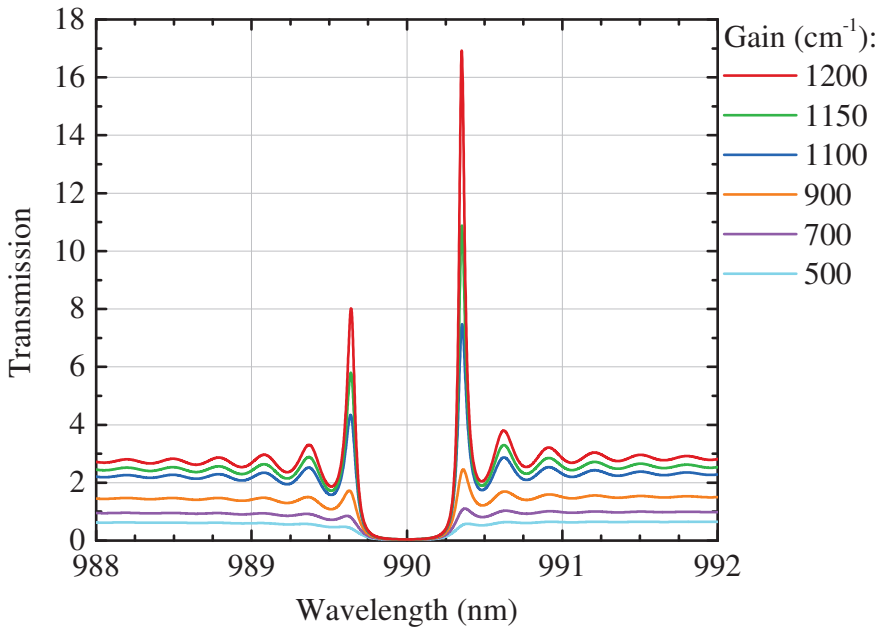

Figure 5.2: Transmission through the DFB as a function of wavelength for increasing values of gain. This demonstrates how the DFB laser preferentially selects a single-mode output on the band edge of the reflectivity spectrum as the device is pumped.

Typically, a DFB laser produces two degenerate lasing modes at both of

the band edges, yet as Fig. 5.2 shows, one of these modes has significantly more transmission. It was predicted that this breaking of the degeneracy was due to the inclusion of Pd, so an identical DFB structure without the Pd layer was simulated. The transmissions as functions of wavelength for both of the DFBs with and without Pd are shown in Fig. 5.3. As shown for the case of the DFB without Pd, both of the band edges are generate, and as a result, the laser will lase at both of these wavelengths. However, the inclusion of Pd breaks this degeneracy, producing single-mode output. In most commercial DFB lasers, this degeneracy must be broken by including a $\lambda/2\,n_{eff}$ cavity in the center of the device to produce destructive interference for one of these modes. This is an additional design parameter that typically must be carefully controlled that can instead be eliminated by using Pd. Also, since this cavity is no longer required, these devices can potentially be fabricated using low-cost interference lithography rather than e-beam lithography.

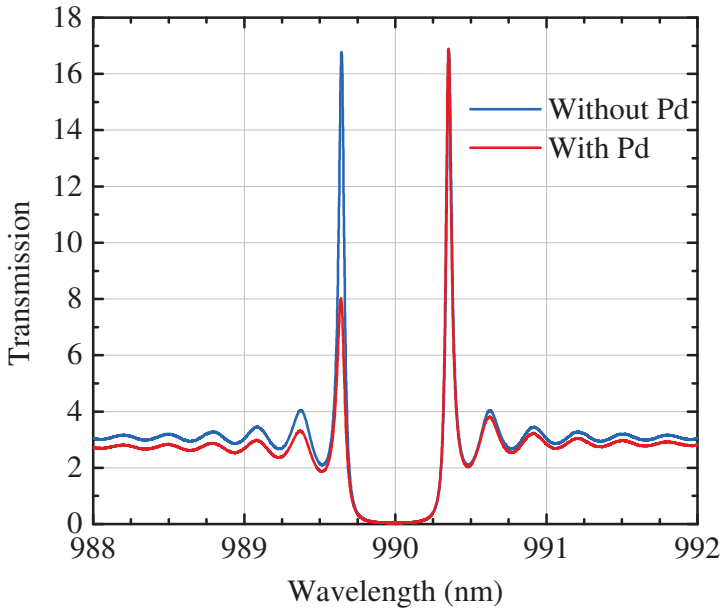

Figure 5.3: Transmission through the DFB as a function of wavelength for the cases of with and without Pd showing that the inclusion of Pd breaks the degeneracy and preferentially selects one of the two DFB lasing modes.

Next, the transmission spectra for the Pd-coated DFB before and after H_2 exposure were computed, and are presented in Fig. 5.4. After adding H_2, the reflection spectrum of the DFB broadens, causing the band edges to spread out. For the mode that was preferentially-selected due to the inclusion of Pd, this causes a peak wavelength redshift due to H_2 exposure.

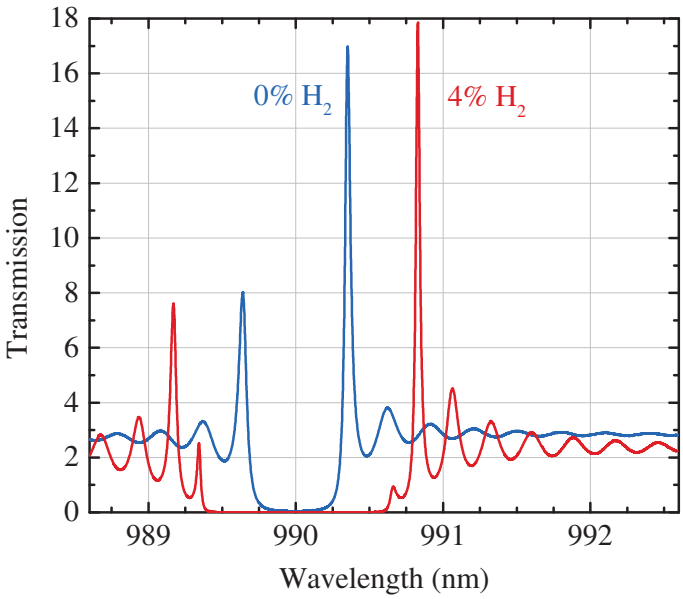

Figure 5.4: Transmission through the Pd-coated DFB with and without exposure to H_2 showing the peak transmission shift, which corresponds to the predicted wavelength shift.

The results from the analytical calculations are tabulated in Table 5.1. Plots of the simulated L-I curves for the DFB laser before and after H_2 exposure are shown in Fig. 5.5. As shown, the output power increases significantly with the exposure to H_2 due to a large decrease in threshold current.

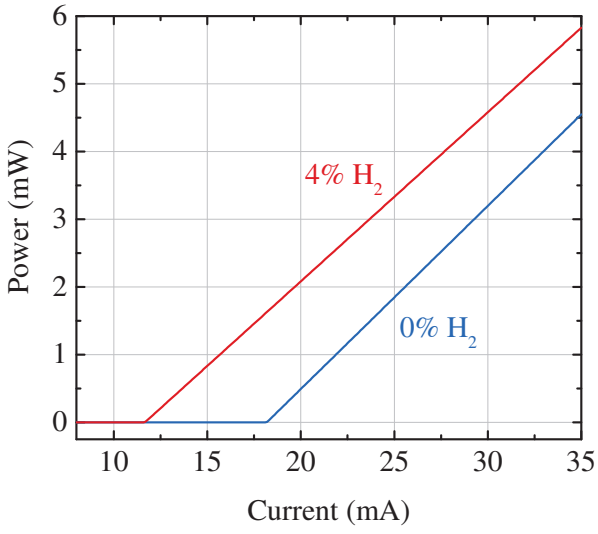

Figure 5.5: Simulated L-I curves for the DFB laser sensor before and after H_2 exposure.

Table 5.1: Simulation results for the distributed feedback laser sensors

Parameters	**Symbol**	**H_2**	**Value**
Mirror Loss	α_m	0%	32.22 cm^{-1}
		4%	25.42 cm^{-1}
Pd Loss	$\alpha_{i,Pd}$	0%	23.056 cm^{-1}
		4%	21.08 cm^{-1}
Threshold Gain	g_{th}	0%	1418.15 cm^{-1}
		4%	1211.65 cm^{-1}
Threshold Carrier Density	N_{th}	0%	6.06×10^{12} cm^{-2}
		4%	4.95×10^{12} cm^{-2}
Threshold Current	I_{th}	0%	18.18 mA
		4%	11.66 mA
Differential Efficiency	η_d	0%	0.43
		4%	0.39
Wavelength Shift	$\Delta\lambda$	$0 \rightarrow 4\%$	0.48 nm

5.4 Device Fabrication

These devices were fabricated such that they could be easily measured in the H_2 gas chamber, which requires wire-bonding. Since the ridge width is too narrow to wire-bond, a larger contact pad is needed. Instead of depositing Pd on both sides of the apodized ridge waveguide, a benzocyclobutene (BCB) planarization layer was used to form a large contact pad on one side of the ridge that can be easily wire-bonded. An illustration of this design modification is shown in Fig. 5.6.

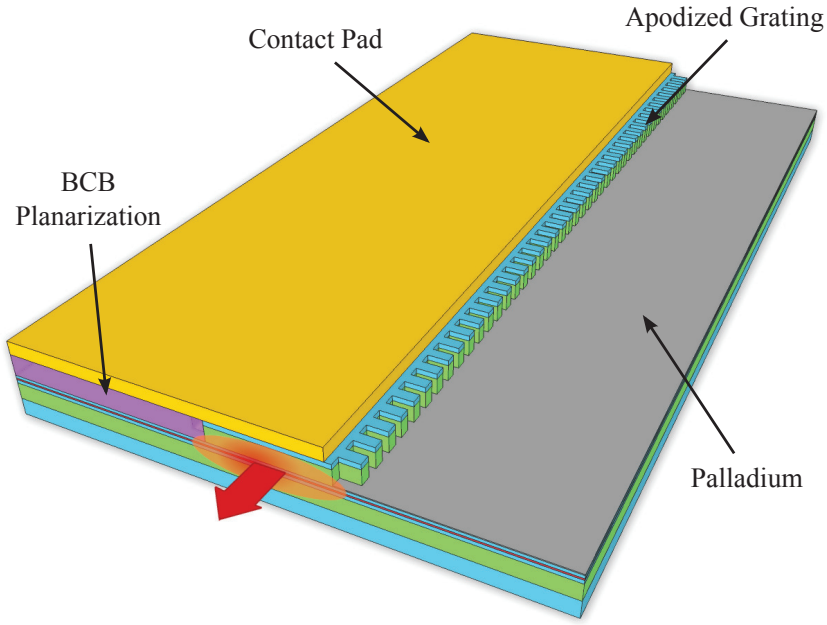

Figure 5.6: Illustration of the fabricated DFB laser sensor with BCB planarization layer.

The fabrication process (as detailed in Appendix B.3) starts with the deposition of an SiO_2 layer using plasma enhanced chemical vapor deposition (PECVD). This SiO_2 layer is then patterned using electron-beam lithography, and etched using a Freon plasma reactive ion etch (RIE) to pattern the apodized ridge. The remaining patterned oxide is used as an etch mask in a $SiCl_4$-based inductively coupled plasma (ICP) RIE to transfer this oxide ridge pattern to the GaAs material below.

Next, a thin (20 nm) layer of SiO_2 is deposited over the entire sample to promote BCB adhesion and passivate the etched sidewalls. BCB is then spun onto the sample and cured. The BCB is then etched back using a Freon plasma RIE reaching the surface of the SiO_2 layer, in which the Freon RIE

mixture is changed to etch the BCB and SiO_2 at similar rates to planarize the BCB to the top surface of the GaAs ridge.

Next, the top-side p-type contact Ti/Pt/Au (15/10/200 nm) is deposited, and the unwanted metal is lifted off in acetone. This contact metal as an etch mask in a Freon RIE etch to remove all BCB from the portions of the sample that do not possess contact metal. This exposes the area on the opposite side of the ridge for the Pd deposition.

Next, the sample is lapped and polished, and backside n-type contacts Ge/Au/Ni/Au (20/50/30/50 nm) are deposited and annealed at 400°C for 30 seconds in an N_2 ambient to form an alloy. Finally, a blanket deposition of Pd (20 nm) is performed on the top-side of the sample. The sample is then cleaved into bars to define the 500 μm cavity length. SEM images of the fabricated devices are shown in Fig. 5.7.

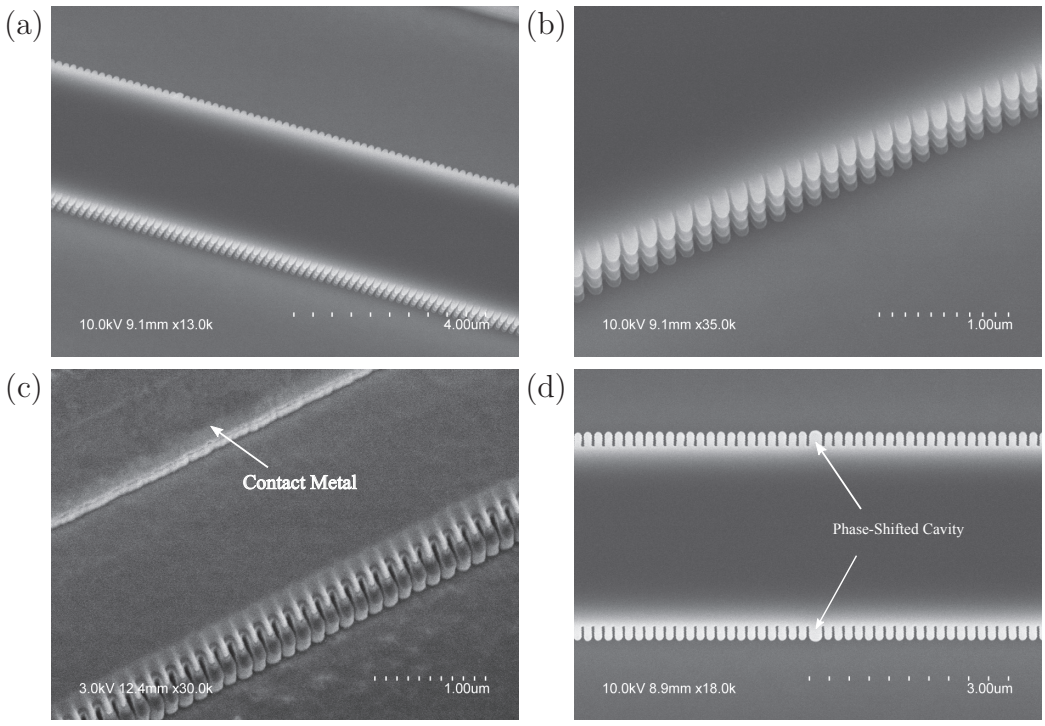

Figure 5.7: SEM images of the fabricated DFB laser sensors (a) zoomed-out showing the apodization on both sides of the ridge, (b) zoomed-in on the sidewall profile of the apodized grating, (c) a fully-fabricated device including the BCB planarization layer and contact metal, and (d) top-down view of the grating showing a phase-shifted cavity that was unused for the experimental measurements, but available in the device design.

5.5 Experimental Measurements

Of particular interest in the DFB laser sensor is the predicted single-mode lasing spectrum. The output spectrum of the device was measured before exposure to H_2 to demonstrate how the inclusion of Pd into the device structure helps to break the degeneracy between the two transmission peaks, providing single-mode output. This spectrum is shown in Fig. 5.8, and has a side mode suppression ratio (SMSR) of approximately 30 dB. All spectra were collected at an injection current of 70 mA at 20°C.

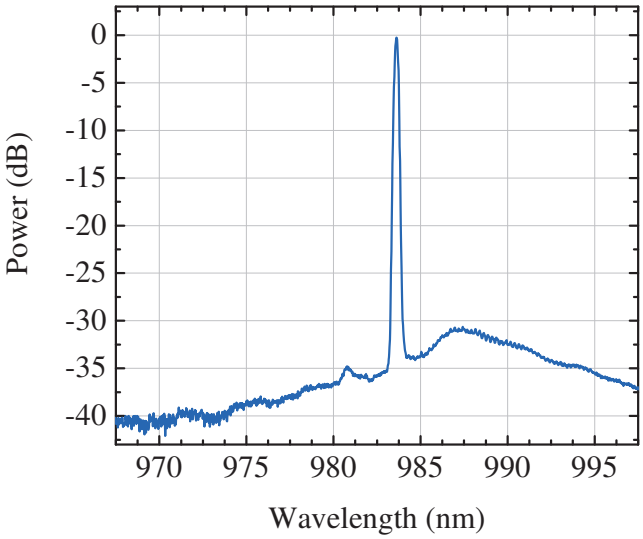

Figure 5.8: Measured spectrum of the DFB laser sensor showing the single-mode characteristics.

Next, this spectrum was monitored as the DFB laser sensor was soaked in various concentrations of H_2. The output spectra for the various H_2 concentrations is shown in Fig. 5.9. As shown, the output wavelength redshifts with the inclusion of H_2. The wavelength shift is 68.4 pm for a 1% H_2 exposure.

The output power response to H_2 exposure was then measured. Figure 5.10 shows the measured L-I curve of the DFB laser sensor before and after exposure to 1% H_2. As for the ridge-waveguide EEL sensors, the threshold decreases and the efficiency increases as H_2 is added, showing an increase in output power for a constant injection current. Next, H_2 pulse measurements were performed to observe the response and recovery times of the device during H_2 exposures. The pulse test results are shown in Fig. 5.11 with an injection current of 65 mA. The increase in output power is proportional to

the H_2 concentration, and this sensor seems to be able to easily detect H_2 concentrations well below 1%, which seems to be more sensitive overall than the other semiconductor laser designs.

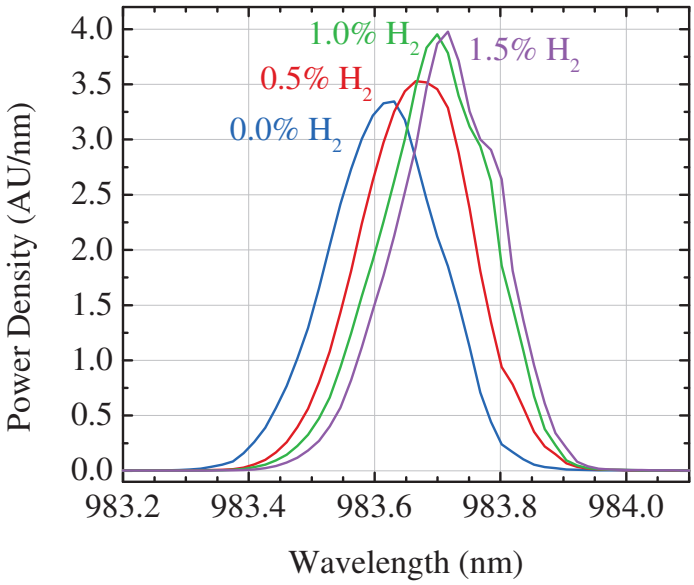

Figure 5.9: Measured sensor spectra after soaking in various H_2 concentrations showing a wavelength redshift for increasing H_2 concentration.

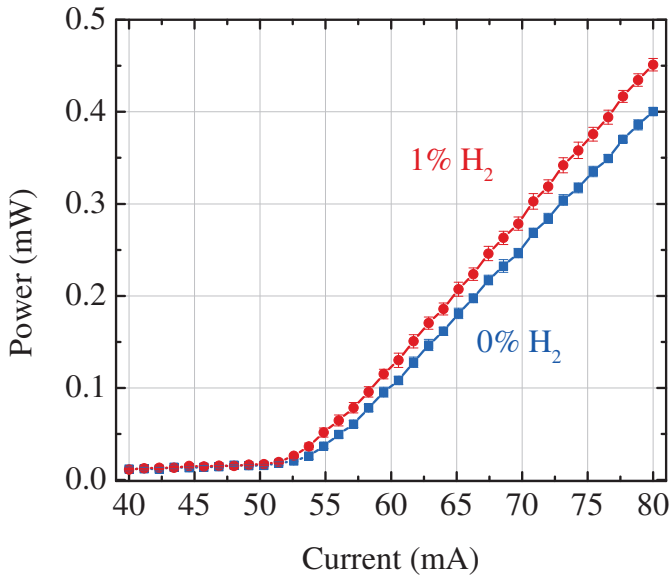

Figure 5.10: Measured L-I curves for the DFB laser sensor before and after soaking in 1% H_2.

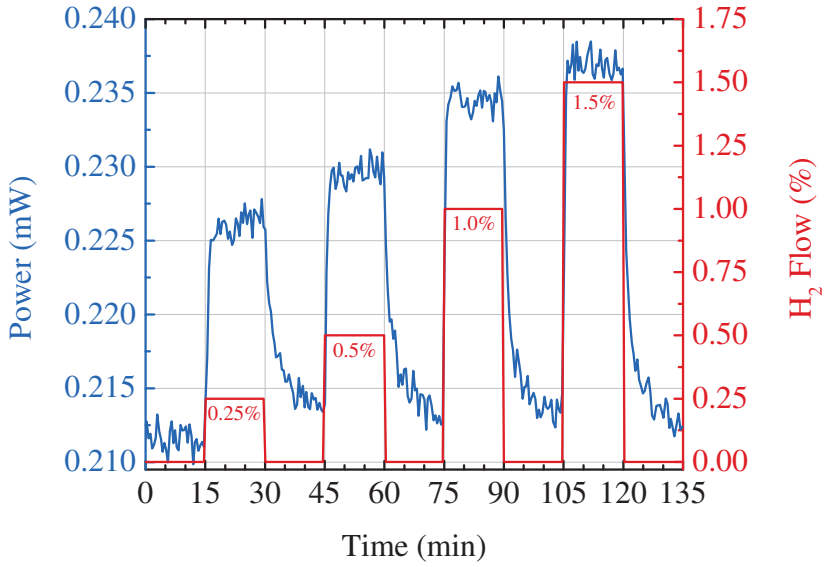

Figure 5.11: H_2 pulse measurements of the output power for the DFB laser sensor.

5.6 Discussion

The DFB laser sensor is essentially a modification of the standard ridge-waveguide EEL sensor, but with an apodized grating along the entire ridge, causing the device to lase with single-mode output. Due to the single-mode nature of this device, much larger wavelength shifts can be measured due to the lack of mode-hopping that was seen in the multi-mode EEL sensor. Additionally, this is a superior alternative to the DBR laser sensor due to the increased interaction area, increased reflectivity along the grating eliminating the need for cleaved facets, and a simpler testing procedure due to a single contact pad.

Additionally, since the DFB laser does not require cleaved facets, this geometry is suitable for coupling to in-line photodetectors. Theoretically, an array of these devices can be fabricated on a single chip, multiplexed together, and then measured on photodetectors also fabricated on the same chip. This allows for advanced measurement techniques including differential measurements by only functionalizing some of the devices and leaving the others de-functionalized, or by using a catalyst layer other than Pd for functionalization so that multiple traces gas species can be detected simultaneously using a single chip, which can be used to prevent cross-sensitivities and greatly improve the selectivity.

CHAPTER 6

CONCLUSION

In this dissertation, an effective process for the development of a practical, inexpensive means in which to functionalize already well-established semiconductor laser structures as a platform for H_2 sensing of concentrations below the lower explosive limit for fuel cell leak detection applications has been presented. Four different laser structures consisting of both in-plane and vertically-emitting geometries have been studied. All four of these basic structures are already widely manufactured, and functionalization to enable H_2 detection could be performed easily. Each of these device structures has proven to show a shift in laser output power and lasing wavelength relative to the concentration of H_2. All sensors exhibit minimum detection limits below the lower explosive limit, and would be appropriate for fuel cell leak detection.

By analyzing these different laser structures, several conclusions can be made about the design considerations that must be taken into account for the engineering of semiconductor lasers for sensing due to evanescent mode overlaps. The first, is that a single-mode output is necessary for predictable, clear wavelength shift-based measurements, and is beneficial for output power-based measurements. Next, the interaction area between the optical mode and the sensitive layer must be kept as large as possible. Ideally, the optical mode should interact with the sensitive film throughout its entire propagation in the cavity.

The laser structures developed here are all appropriate for the intended application, and all structures have their own advantages and disadvantages depending on the specific intended implementation. The ridge-waveguide EEL is by far the simplest of the structures, and will also be the most inexpensive to fabricate. This structure does not require an epitaxially-grown stack of alternating layers like the PhC VCSEL structure, and does not require electron-beam lithography to pattern as is true for the DBR and DFB

laser sensors. Unfortunately, it only shows moderate power and wavelength shifts, and the wavelength shifts it does produce are not reliable due to mode-hopping. The PhC VCSEL has its own clear advantages due to the fact that it is vertically-emitting. Just as all VCSEL structures have advantages over in-plane lasers depending on the application, so too does the PhC VCSEL sensor. The DBR and DFB laser sensors both provide in-plane emission like the ridge-waveguide EEL, and are more suitable for on-chip multiplexing and detection. The DBR laser sensor is unfortunately not nearly as sensitive as the DFB laser, and is much more difficult to fabricate and test; however, the dual DBRs allow for tuning of the mirror reflectivities, which is a property that can possibly be exploited for differential measurements. The DFB laser sensor is clearly the most well-balanced of the in-plane geometries due to its easy fabrication process and testing procedure, high sensitivity, and ability to array without the need for cleaved facets. Additionally, any one of these laser sensor designs can be easily functionalized to detect a target gas, or even biological agent other than H_2 by simply switching out the Pd film with a different catalyst. Therefore, this work presents not only a means in which to produce inexpensive, micron-sized H_2 sensors for fuel cell leak detection applications, but also has wider implications in a broad variety of fields where sensing is important.

APPENDIX A

MEASUREMENT SETUP AND PROCEDURE

A.1 Testing Setup

The hydrogen sensing measurements need to be taken in a custom-machined airtight chamber to properly control the H_2 concentration inside of the chamber and to prevent leaking into the atmosphere for safety purposes. Additionally, the chamber volume needs to be kept as small as possible so that the total H_2 concentration within the chamber can stabilize and purge quickly, so that accurate response times can be quantified. Due to this requirement, the photodetector cannot be placed inside of the chamber and the measurements must be taken by coupling the light onto an optical measurement apparatus external to the chamber. Therefore, the chamber needs either to be transparent to light at infrared frequencies or have a window for the output light to pass through. It was chosen to use a transparent material for the chamber.

The test chamber that has been designed and machined consists of a polycarbonate piece that surrounds the sample and allows gas to flow through, a printed circuit board (PCB) on which to solder and wire-bond the sample and probe using contact pads located outside of the chamber, and a copper temperature modulation stage.

The sample to be measured is first soldered onto a small (5 mm $\times$ 5 mm) copper square using a high temperature solder capable of withstanding the necessary wire-bonding temperatures. The purpose of this square is to elevate the sample above the O-ring that is used to seal the chamber. Otherwise, the opaque O-ring, which surrounds the sample, will block the light coming from the device in the case of the edge-emitting lasers. Next, this square is soldered to the center of the PCB. Surrounding the pad on which the sample is soldered are several small contact pads that, via backside traces, connect to larger pads surrounding the perimeter of the printed circuit board. The

proper contacts on the device to be tested are wire-bonded to these smaller pads. The larger pads are connected to a current source to be used for electrical pumping of the laser diode. Next, a polycarbonate piece with a hollowed-out cylindrical chamber is placed over the sample, and connects to a copper temperature modulation stage placed below the printed circuit board. The polycarbonate piece has a gas line running through the center of the chamber, allowing for various gas mixtures to flow over the surface of the sample during measurements. An external detector is placed outside of the chamber to collect light from the device.

(a)

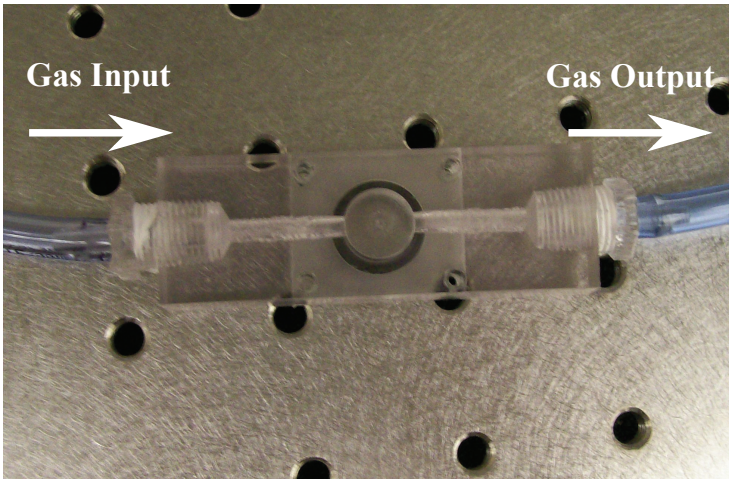

(b)

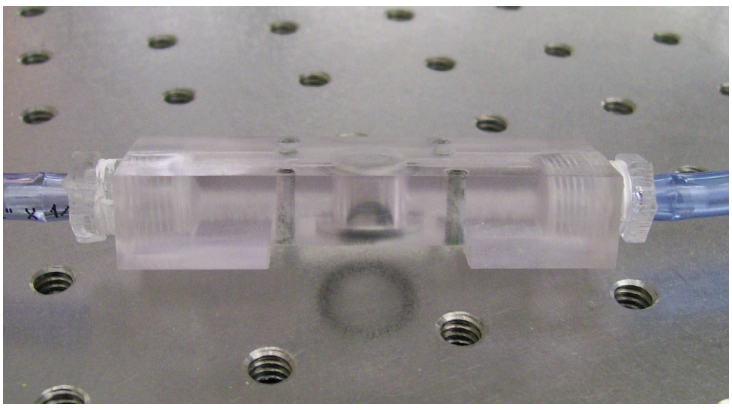

Figure A.1: Photograph of the polycarbonate measurement chamber, showing (a) a top view illustrating the direction of gas flow, and (b) a side view.

A photograph of the final machined polycarbonate chamber is shown in Fig. A.1. Polycarbonate was chosen for the testing chamber due to its 90% transmission of visible and infrared light through 3 mm of material. This allows for accurate measurements by external detectors located outside of

the chamber. Additionally, this design allows for the testing of vertically-emitting lasers through the top. The polycarbonate piece itself is 22 mm × 65 mm. The cylindrical chamber has a diameter of 10 mm and a height of 7 mm. The thickness of the chamber sidewalls are 6 mm (80% transmission of infrared light), and the thickness of the chamber top is 2 mm. The gas line running through the chamber has an 1/8″ diameter, matching the 1/8″ diameter of the gas lines leading to the test setup.

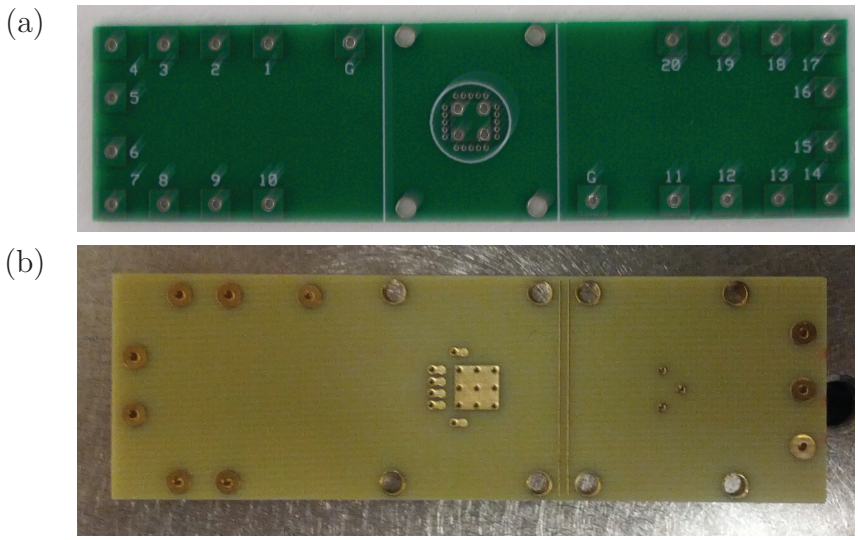

Figure A.2: Photographs of the printed circuit boards, showing (a) the first revision ordered from ExpressPCB, and (b) the second revision ordered from Pad2Pad.

The PCB has gone through two different design iterations. Photographs of both designs are shown in Fig. A.2. The first design, shown in Fig. A.2(a), was ordered from ExpressPCB, and has 20 contact pads surrounding the sample. For edge-emitting laser measurements, the PCB is cut along one of the white lines printed on the top surface, making only 10 contact pads usable. Meanwhile, the external detector is placed as close to the cut edge as possible. For vertically-emitting laser measurements, all 20 contact pads are usable. This initial design had several downsides. The first, is that the contact pads were covered by a solder mask, which significantly reduced the pad area in which to wire-bond. The second, is that the exposed portions of the contact pads were coated with a SnPb plating, which helps assist soldering, but makes the wire-bonding especially difficult. Finally, the contact pads were small and placed very close together, which only allowed every alternate

contact pad to be used due to wire-bonding difficulties. The second design iteration, shown in Fig. A.2(b) was ordered from Pad2Pad, and was modified to alleviate these complications. The contact pads included no solder mask, were plated in Au (which is easy to wire-bond), and were significantly larger. Additionally, the second half of the PCB was replaced with a design that allows for easy soldering of TO-Can packaged lasers. Like the initial design, the improved version is also intended to be cut into two pieces, separating the wire-bonding portion from the TO-Can portion. Full schematics showing the backside traces on each of the PCB designs are provided in Appendix A.3.

Both PCB designs had a 5 mm $\times$ 5 mm square in the center in which to solder the devices. Surrounding this square are small pads that are used to wire-bond to the contact pads on the device sample. Each of these gold pads connects to a larger square pad via backside traces that will be external to the chamber. These larger external pads are connected directly to the current source used for the measurements. The wire-bonding process can be difficult and has taken time to perfect a procedure that is readily repeatable. While working on this, a variety of soldering methods have been tested, as well as a variety of wire-bonding parameters and techniques.

The final soldering process is to first use Indalloy #205 solder to adhere the sample to the copper square. This solder is 60% In and 40% Pb, and melts at 181°C. Then, Indalloy #2 is used, which is 80% In, 15% Pb, and 5% Ag and melts at 154°C, to adhere the copper square to the printed circuit board. Both solders are in ribbon form. A small square of the solder is cut from the ribbon, and first melted on the contact stage in which the device is to be soldered (the copper square for Indalloy #204, and the PCB for Indalloy #2) using a hotplate. Then, this contact stage is removed from the hotplate, and the solder is allowed to cool. The sample (or the copper square, for Indalloy #2) is now placed on the cooled solder, and re-heated on the hotplate until the solder re-melts. If there are adhesion problems during the soldering process, Indalloy Flux #2 has been shown to help considerably. Finally, before wire-bonding, a coating of Arctic Silver Alumina thermal compound, which is thermally conductive but electrically insulting, is applied to all portions of the copper square to prevent short circuits between the stage and wire-bonds.

The wire-bonding process uses a gold ball-bond (100μm diameter) on the

sample's contact pad, and a wedge-bond on the PCB contact pad. The wire diameter is 20μm, and the process is performed at 130°C. The first stage of the wire-bonding process is the ball-bond. For the ball-bond, an electric spark is made at the tip of the gold wire. This melts the very tip, forming a ball. This ball is then pressed to the heated contact pad, and vibrated until the ball melts and adheres to the pad. The ball-bond will be formed on the device contact pad because it is less harsh than the wedge bond, which may damage the sample. The second stage is the wedge-bond. The wedge-bond scrapes the gold wire against the contact pad, forcefully breaking the wire. Photographs of the wire-bonding setup and a sample which has been wire-bonded are shown in Fig. A.3. The values for the wire-bonder parameters used are shown in Table A.1.

(a)

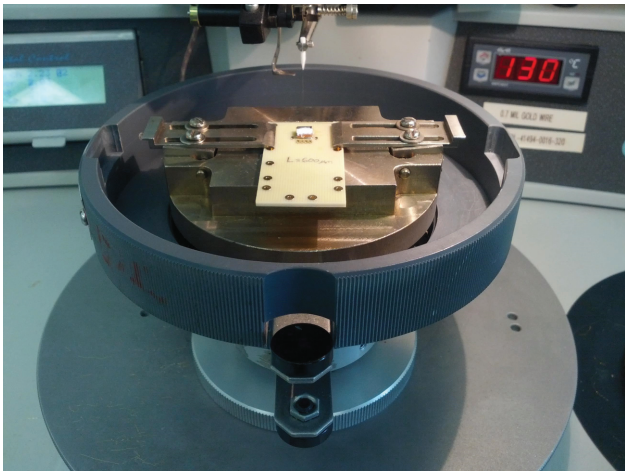

(b)

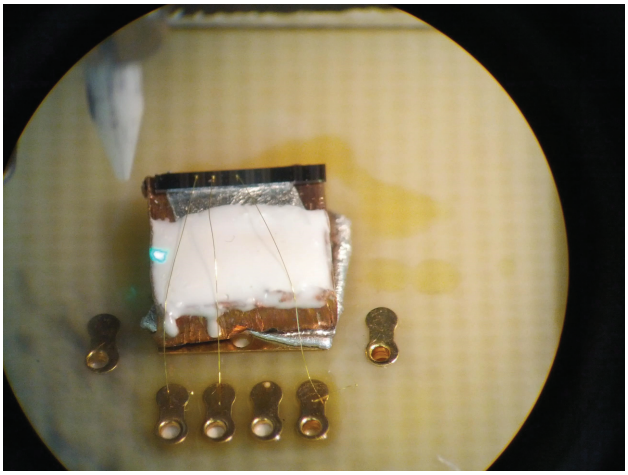

Figure A.3: Photographs of the wire-bonding process, showing (a) the PCB mounted in the wire-bonder, and (b) a microscope image of wire-bonded devices.

Table A.1: Wire-Bonder Parameters

Search = 2.23	**1**
Power = 2.03	
Time = 3.0	
Force = 3.0	

Search = 6.26	**2**
Power = 3.01	Loop = 7.0
Time = 5.1	Tail = 3.5
Force = 7.0	Ball = 4.5

The temperature modulation stage, as shown in Fig. A.4, consists of two silver-coated copper blocks with a Peltier thermoelectric cooler (TEC) sandwiched between them. The TEC transfers heat from one of the copper blocks to the other, allowing the top surface, on which the sample is placed, to be either heated or cooled to a desired operating temperature. A hole is drilled through the center of the smaller top block on a side face and a thermistor is inserted, so that it is located directly underneath where the sample will be mounted. The thermistor is then sealed in place with Arctic Silver Alumina, which is thermally conductive but electrically insulating. The thermistor is a temperature-dependent resistor, which can be used to measure the temperature of the upper block. Connections from the TEC (used to change temperature) and thermistor (used to measure current temperature) are attached to a proportional-integral-derivative (PID) controller to help regulate the temperature of the sample to a specified set-point.

Photographs of the fully-assembled test setup are shown in Fig. A.5. Full mechanical drawings for each part of the test assembly with dimensions labeled are provided in Appendix A.3.

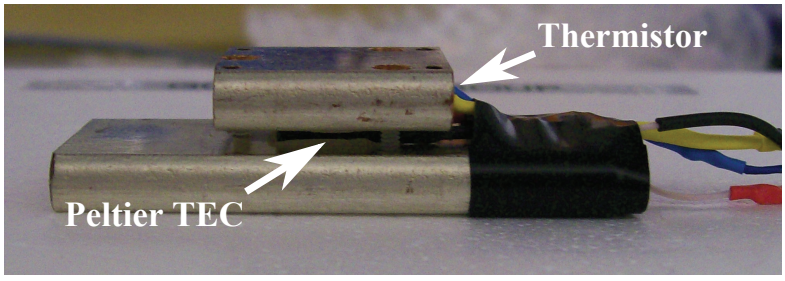

Figure A.4: Photograph of the copper temperature modulation stage with the Peltier TEC and thermistor labeled.

(a)

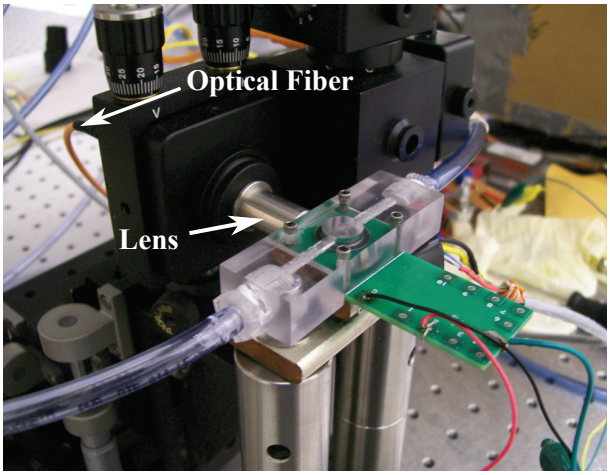

(b)

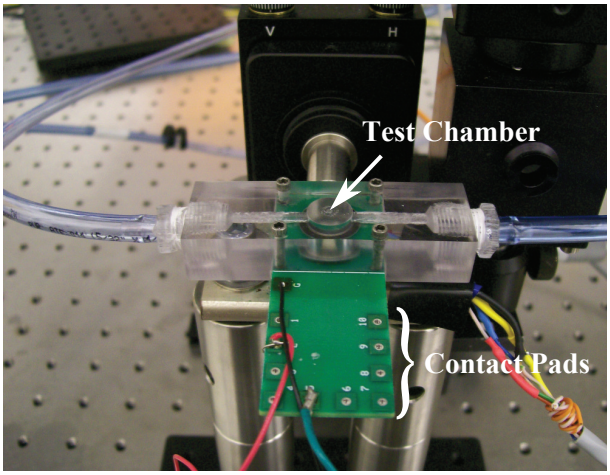

Figure A.5: Photographs of the fully-assembled measurement setup, showing (a) a side view, and (b) a front view of the test chamber aligned to a lens-coupled optical fiber.

A.2 Measurement Procedure

The measurements were taken by first attaching current probes to the outer pads of the printed circuit board (which make electrical contact to the devices under test). Next, LabVIEW code is used to control a current source, which is used to pump varying levels of current through the device, while the light output power is coupled to the external optical system. The edge-emitting lasers were pumped using an ILX LDP-3840 pulsed current source with pulse widths of 1 μs at a 1% duty cycle, while the vertically-emitting lasers were pumped using an ILX LDC-3908 continuous wave (CW) current source. During all measurements, the stage is temperature controlled to reduce drift due to device heating or to quantify the impact of operating

temperature on device performance.

For the power measurements, to ensure that all of the light is collected and that the testing stage is insensitive to slight misalignment, an integrating sphere is used. This integrating sphere is attached to a Thorlabs PDA10CS InGaAs photodetector, and the resulting photocurrent is measured on an HP 54825A oscilloscope. For the wavelength measurements, a lens is aligned to the output of the laser, coupling as much light as possible to an optical fiber, which is then sent to an HP 70951B optical spectrum analyzer (OSA) with the resolution set to 0.08 nm. While these measurements are being made, various concentrations of H_2 in a nitrogen gas (N_2) ambient are flowing through the chamber. The response of the laser's output power and wavelength in relation to the H_2 concentration are then recorded and used to verify the sensor's performance.

The gas flow system was designed to quickly switch between the gases to be measured. The system works by sending a gas mixture to the input of the test chamber, and the exhaust of the gas chamber is sent to the lab's dump line. The gases to be sent into the chamber are diluted H_2 in N_2 and pure N_2. For the input gas mixture, there is a mass flow controller (MFC) for the N_2 flow and an MFC for the H_2 flow. Since the switching time for the MFCs can take longer than desired, an electrically operated solenoid valve with a response time of 20–30 ms is used to switch between gases. All MFCs and solenoid valves are controlled using an Adlink PCI-6208V DAQ card and custom-made LabVIEW code. During operation, the MFCs are on, and N_2 is flowing into the chamber. Without applying an electrical bias to the solenoid valve, the H_2 from the MFC is sent directly to the dump, bypassing the chamber. When a voltage is applied to the solenoid valve, the H_2 is mixed with the N_2 and sent to the input of the chamber. Additionally, there is a second N_2 MFC continuously sending N_2 to the dump. This is to dilute the dumped H_2 in the lines for safety purposes.

In the future, additional test setups for different types of devices will be made, and a variety of other trace gases will be added. Each new trace gas will require an MFC and a solenoid valve, and will connect to the current H_2 flow system. Additionally, future alternative testing stations can be used by switching a series of manual valves that control which station the gases are sent to. Future gases to be added include CO, O_2, CO_2, CH_4, NO_2, and air (as an alternative carrier gas).

A.3 Test Chamber Schematics and Mechanical Drawings

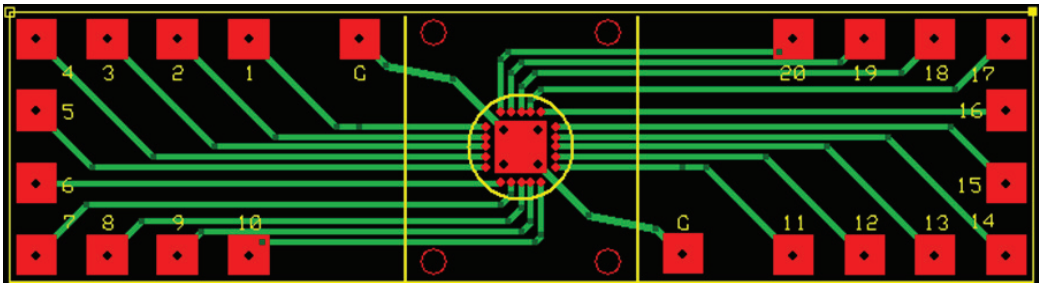

Figure A.6: Schematic of the first revision printed circuit board (ExpressPCB).

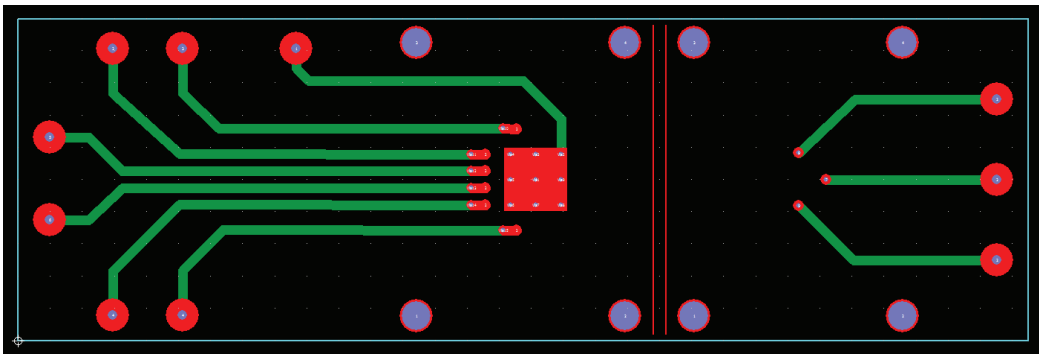

Figure A.7: Schematic of the second revision printed circuit board (Pad2Pad).

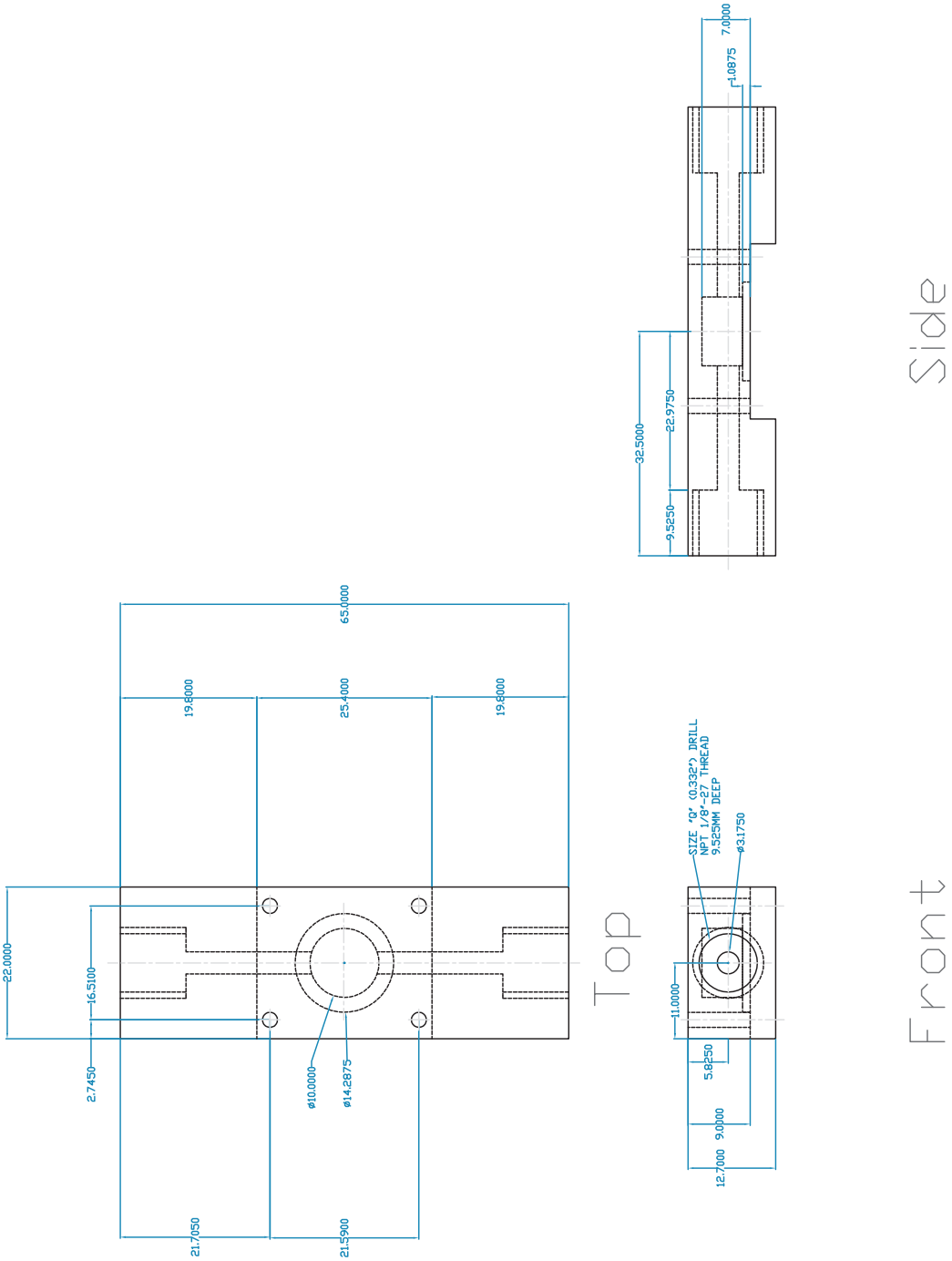

Figure A.8: Mechanical drawing of the polycarbonate chamber.

Figure A.9: Mechanical drawing of the printed circuit board.

Figure A.10: Mechanical drawing of the copper temperature stage (upper block).

Figure A.11: Mechanical drawing of the copper temperature stage (lower block).

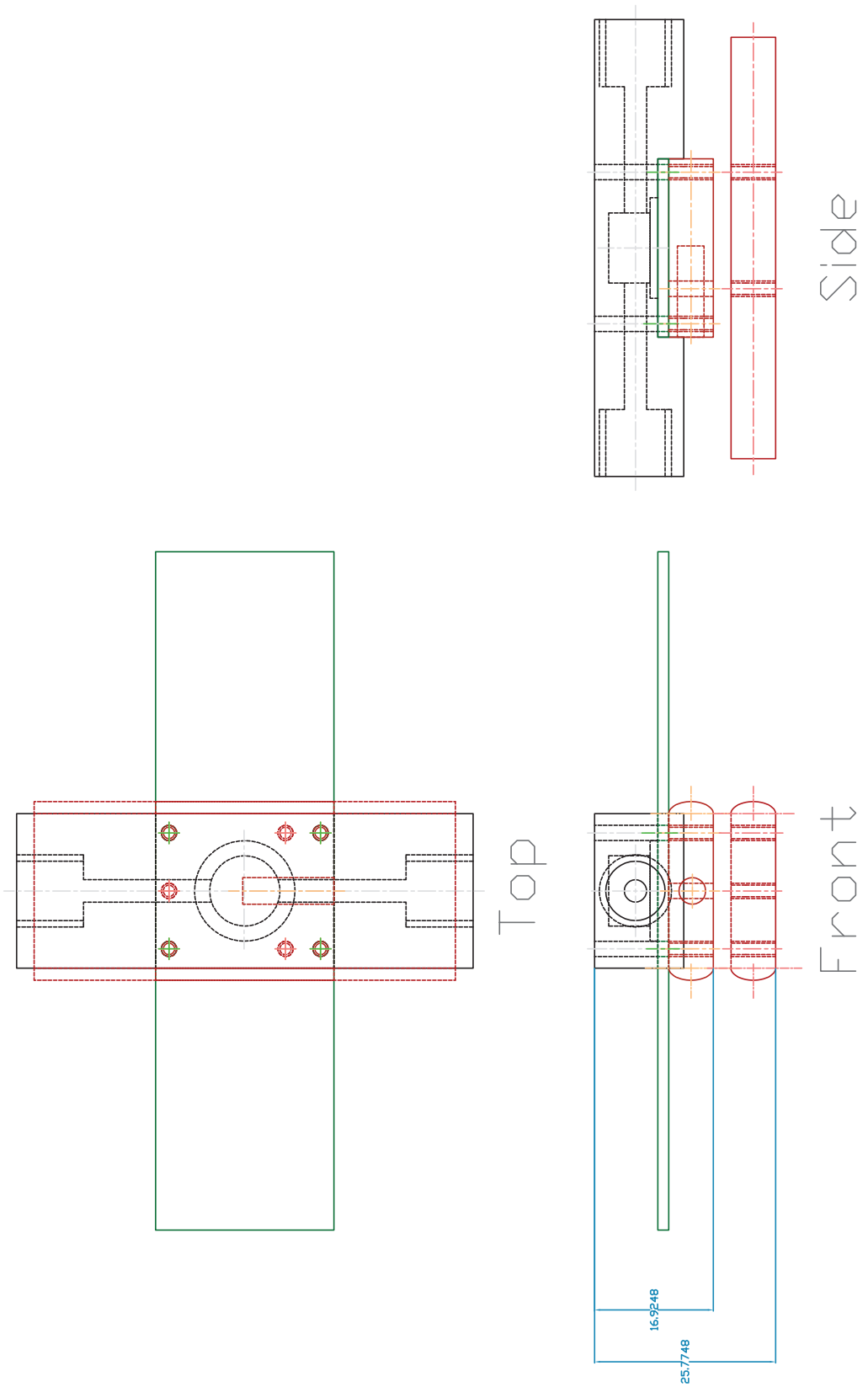

Figure A.12: Mechanical drawing of the full custom testing assembly.

APPENDIX B

DEVICE FABRICATION PROCESSES

B.1 Ridge-Waveguide Edge-Emitting Laser Sensor

This fabrication process uses the mask titled *PSL-GasSensor.gds*, dated 1/27/2010. It was made by the UCLA Nanoelectronics Research Facility.

The mask is comprised of four quadrants. Quadrant #1 (upper-right) patterns the pad oxide, quadrant #2 (upper-left) patterns the contact metal, quadrant #3 (lower-left) patterns the palladium, and quadrant #4 (lower-right) contains a pattern similar to that of the contact metal, but with wider ridges (this was originally intended for an apodized grating, but is currently unused).

The mask contains ridge widths of 3, 4, 5, 6, 8, and 10 μm. The contact pad width is 100 μm, with 26 μm distance between the pad and the ridge, and 222 μm distance between adjacent devices. The fabrication process is designed to etch 600 nm deep, so that the bottom of the etch ends at the top of the core region (does not etch through the quantum well).

Clean Sample

- Acetone (using sonication) → Methanol → IPA → Water → IPA → dry with N_2

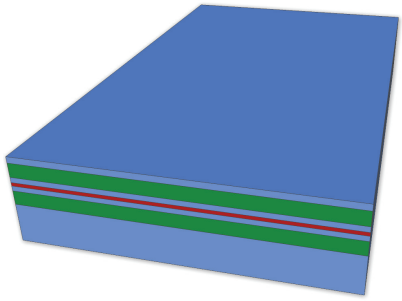

Deposit SiO_2

- PlasmaLab PECVD
  - Power: 35 W
  - Pressure: 1000 mTorr
  - Temperature: 300°C
  - N_2O Flow Rate: 114 sccm
  - SiH_4 Flow Rate: 11 sccm
  - Deposition Time: 11 min
  - Deposition Rate: 10.8 nm/min
  - Desired Thickness: ∼120 nm

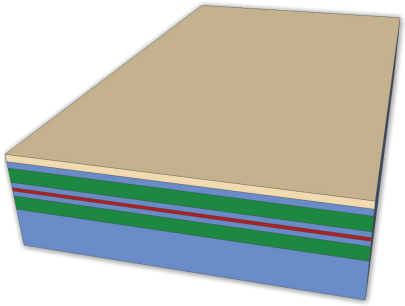

Photolithography: Pattern Oxide

- Mask Quadrant #1
- AZ 5214 as positive photoresist

Etch Oxide

- PlasmaLab Freon RIE
  - Power: 90 W
  - Pressure: 35 mTorr
  - CF_4 Flow Rate: 60 sccm
  - Etch Time: 8 min
  - Etch Rate: 23 nm/min
  - Desired Etch Depth: ∼184 nm

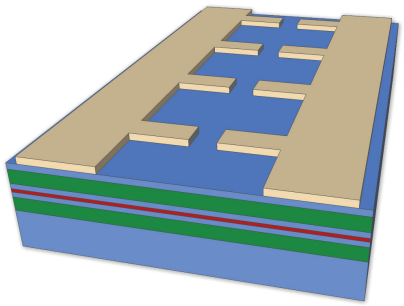

Remove PR

- Acetone → IPA → Water → IPA → Dry with N_2
- Descum in O_2 planar plasma etcher

Photolithography: Pattern Contact Metal

- Mask Quadrant #2
- AZ 5214 as negative photoresist

Deposit P-Type Contact Metal

- CHA Evaporator (E-Beam)
  - Metals: Ti | Pt | Au
  - Thicknesses: 15 | 10 | 250 nm
  - Rates: 1 | 1 | 2 Å/s

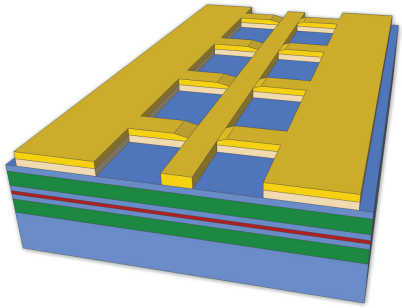

Liftoff

- Acetone → IPA → Water → IPA → Dry with N_2

Etch Ridge

- Wet Etch
  - Chemicals: H_3PO_4 : H_2O_2 : H_2O
  - Ratio: 1 : 1 : 20
  - Etch Rate: ∼200 nm/min
  - Etch Time: ∼3 min
  - Desired Etch Depth: 600 nm

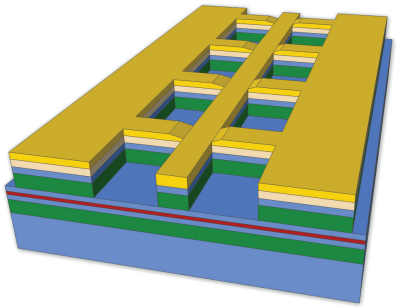

Photolithography: Pattern Palladium

- Mask Quadrant #3
- AZ 5214 as negative photoresist

Deposit Palladium

- CHA Evaporator (E-Beam)
  - Metal: Pd
  - Thickness: 30 nm
  - Rate: 1 Å/s

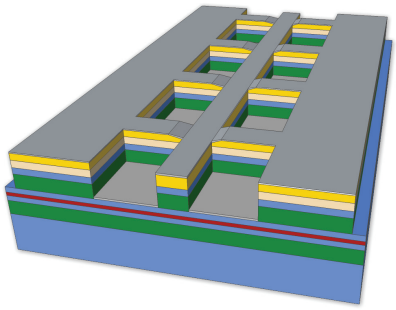

Liftoff

- Acetone → IPA → Water → IPA → Dry with N_2

Lapping and Polishing

- Lap backside of sample to a thickness of ∼6.5 mils (165 μm)

Deposit N-Type Contact Metal (Backside)

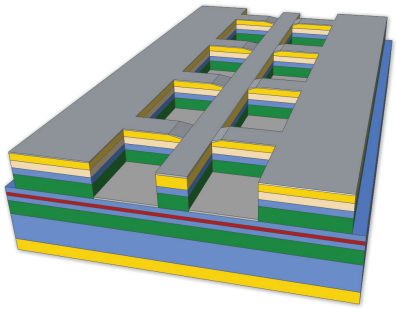

- CHA Evaporator (E-Beam)
  - Metals: Ge | Au | Ni | Au
  - Thicknesses: 20 | 50 | 30 | 50 nm
  - Rates: 1 | 2 | 1 | 2 Å/s

Anneal

- Jipelec RTP
  - Temperature: 400°C
  - Time: 30 sec
  - Ambient: N_2

Cleave

- Cleave location defines cavity length

B.2 Distributed Bragg Reflector Laser Sensor

This device structure was never fabricated, but the fabrication process has been designed. This fabrication process uses the mask titled *PSL_HIRES_ACTIVEPASSIVE_GASSE*, dated 7/13/2011. It was made by Compugraphics.

The mask is comprised of four quadrants. Quadrant #1 (upper-right) and #2 (upper-left) are for active-passive integration devices, quadrant #3 (lower-left) contains the patterns for this DBR laser sensor, and quadrant #4 (lower-right) is for DBR-MRR devices. Quadrant #3 used for this process is split into 6 patterns, all of which are labeled on the mask.

The mask contains ridge widths of 1, 1.5, 2, 2.5, and 3 μm, and cavity lengths of 200, 400, and 800 μm. Each device is designed to have two DBR gratings on each side of the cavity, and can be optionally cleaved through the cavity between the two gratings. Running parallel to each side of the ridge in the cavity region are contact pads. The contact pad on one side of the ridge connects to the ridge as the gain contact, and the other connects to each end of the cavity as the phase contact. Additionally, there are contacts available to electrically pump each of the gratings. At the end of each grating are inline PIN photodiodes connected to their own contact pads. These photodiodes allow for built-in electrical measurement of the laser's output power.

Clean Sample

- Acetone (using sonication) → Methanol → IPA → Water → IPA → dry with N_2

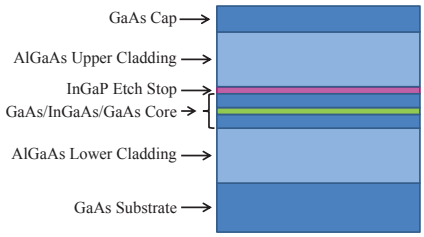

Photolithography: Pattern Alignment Marks

- Pattern #1
- AZ 5214 as negative photoresist
- Metallic alignment marks are used as they are required for e-beam lithography, and they provide enhanced contrast for fine photolithography alignment.

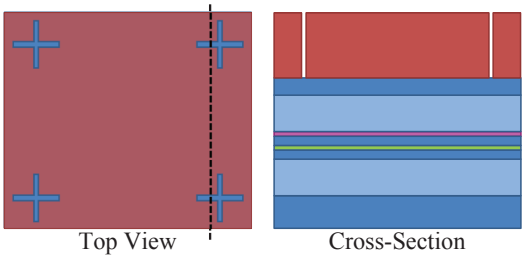

Deposit Alignment Mark Metal

- CHA Evaporator (E-Beam)
  - Metals: Ti | Au
  - Thicknesses: 15 | 80 nm
  - Rates: 1 | 2 Å/s

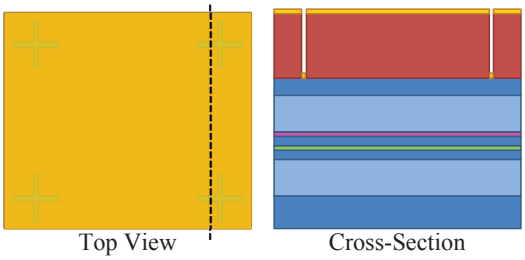

Liftoff

- Acetone → IPA → Water → IPA → Dry with N_2

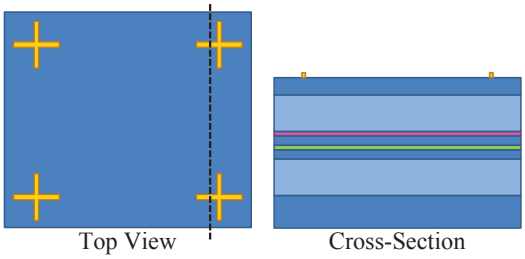

Deposit SiO_2

- PlasmaLab PECVD
  - Power: 35 W
  - Pressure: 1000 mTorr
  - Temperature: 300°C
  - N_2O Flow Rate: 114 sccm
  - SiH_4 Flow Rate: 11 sccm
  - Deposition Time: 11 min
  - Deposition Rate: 10.8 nm/min
  - Desired Thickness: ∼120 nm
- This is used as an etch mask and an electrical insulator for the grating contact.

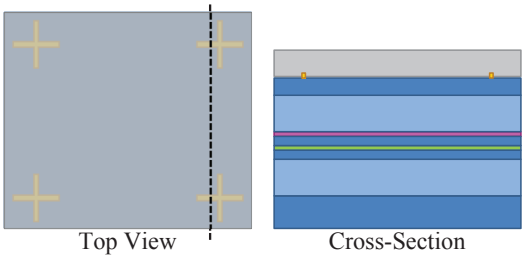

Photolithography: Pattern Ridge

- Pattern #2
- SPR 511a as positive photoresist
- Pattern the sample with positive PR to define the laser ridge, grating contact, and photodiode. Also cover the alignment marks to leave a layer of protective oxide.

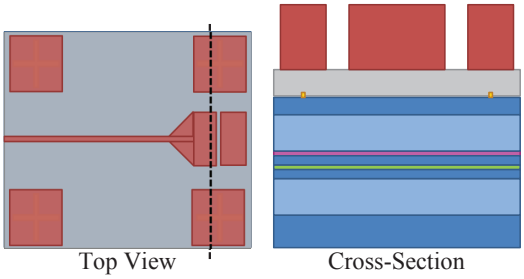

Etch Oxide

- PlasmaLab Freon RIE
  - Power: 90 W
  - Pressure: 35 mTorr
  - CF_4 Flow Rate: 60 sccm
  - Etch Time: 8 min
  - Etch Rate: 23 nm/min
  - Desired Etch Depth: ∼184 nm

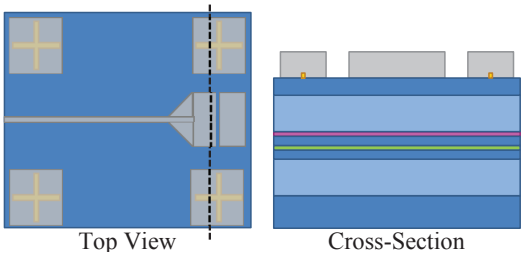

Remove PR

- Acetone → IPA → Water → IPA → Dry with N_2
- Descum in O_2 planar plasma etcher

Etch Ridge

- PlasmaTherm ICP-RIE
  - RF1 Power: 25 W
  - RF2 (ICP) Power: 50 W
  - Pressure: 3 mTorr
  - $SiCl_4$ Flow Rate: 1.7 sccm
  - H_2 Flow Rate: 1 sccm
  - Ar Flow Rate: 10 sccm
  - DC Voltage: ∼80 V
  - Etch Time: ∼8.5 min
  - Etch Rate: ∼70 nm/min
  - Desired Etch Depth: 600 nm

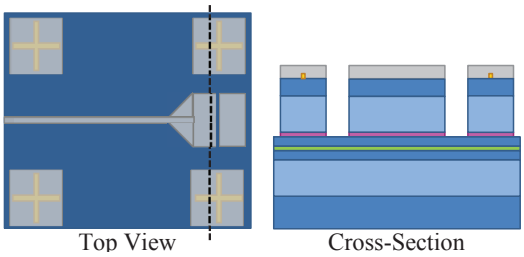

Photolithography: Pattern Insulating Oxide

- Pattern #3
- SPR 511a as positive photoresist
- Pattern the sample with positive PR to define the electrically insulating region of the grating contact pad, and protect the alignment marks.

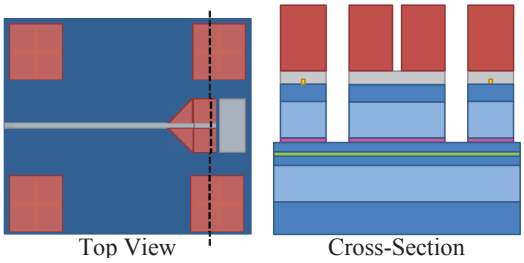

Etch Oxide

- PlasmaLab Freon RIE
  - Power: 90 W
  - Pressure: 35 mTorr
  - CF_4 Flow Rate: 60 sccm
  - Etch Time: 8 min
  - Etch Rate: 23 nm/min
  - Desired Etch Depth: ~184 nm
- Etch through the oxide and remove the PR. This opens up a window to deposit contact metal on the laser ridge and the photodiode, while leaving oxide to electrically insulate the grating contact. This also serves to protect the alignment marks.

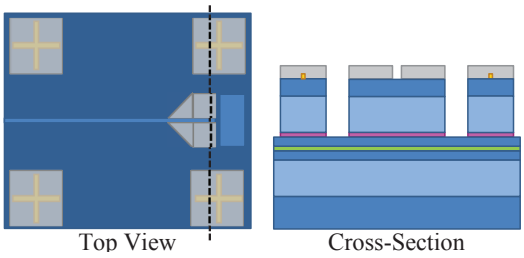

Planarize

- Spin on BCB (~2.1 μm thick)
- Cure BCB
  - N_2 ambient
  - Ramp up to 250°C for 30 min
  - Remain at 250°C for 1 hr
  - Cool down to room temperature for 3 hrs

Etch Back BCB

- PlasmaLab Freon RIE
  - Power: 90 W
  - Pressure: 35 mTorr
  - CF_4 Flow Rate: 25 sccm
  - O_2 Flow Rate: 12.5 sccm
  - Etch Time: 12 min
  - Etch Rate: ~160 nm/min
  - Desired Etch Depth: ~1.9 μm

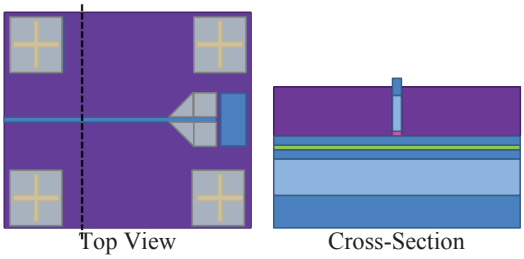

Photolithography: Pattern BCB

- Pattern #4
- SPR 511a as positive photoresist
- Pattern the sample with positive PR to define the BCB layer. All oxide layers must also be covered to protect them from the BCB etch.

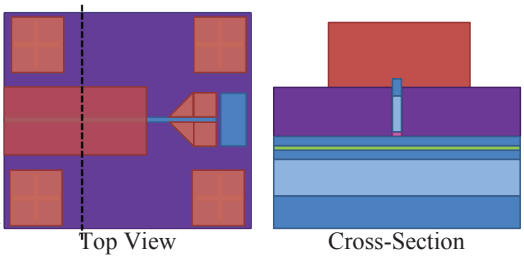

Etch BCB

- PlasmaLab Freon RIE
  - Power: 90 W
  - Pressure: 35 mTorr
  - CF_4 Flow Rate: 25 sccm
  - O_2 Flow Rate: 12.5 sccm
  - Etch Time: ~4 min
  - Etch Rate: ~160 nm/min
  - Desired Etch Depth: ~600 nm

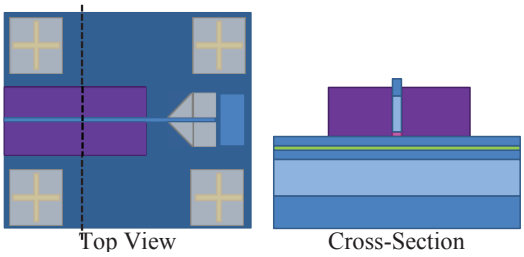

Remove PR

- Acetone → IPA → Water → IPA → Dry with N_2
- Descum in O_2 planar plasma etcher

Photolithography: Pattern Contact Metal

- Pattern #5
- AZ 5214 as negative photoresist

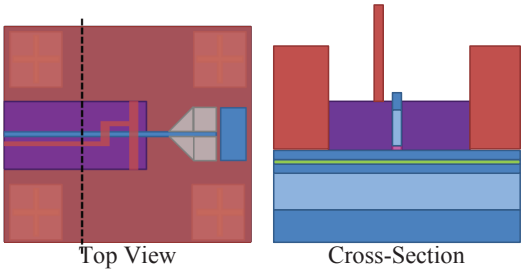

Deposit P-Type Contact Metal

- CHA Evaporator (E-Beam)
  - Metals: Ti | Pt | Au
  - Thicknesses: 15 | 10 | 250 nm
  - Rates: 1 | 1 | 2 Å/s

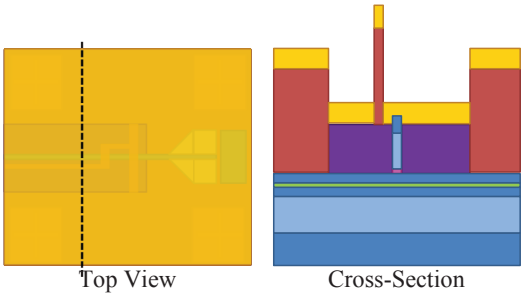

Liftoff

- Acetone → IPA → Water → IPA → Dry with N_2

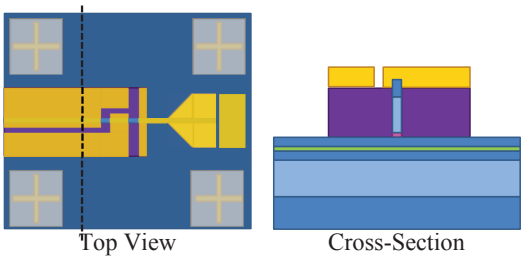

Photolithography: Pattern Cap Etch

- Pattern #6
- AZ 5214 as negative photoresist
- Pattern negative PR on the sample to open windows revealing the metallic alignment marks, and the separation between the contacts on the laser ridge. This PR should be sufficiently thick to protect the AlGaAs cladding from the subsequent BOE etch.

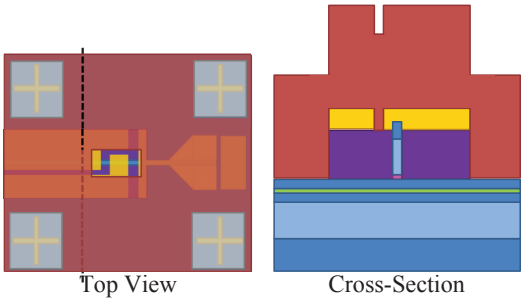

Etch GaAs Cap

- Wet Etch (Citric Acid)
  - ∗ Chemicals: $C_6H_8O_7$: H_2O_2
  - ∗ Ratio: 3 : 1
  - ∗ Etch Rate: ∼6 nm/sec
  - ∗ Etch Time: ∼20 sec
  - ∗ Desired Etch Depth: 100 nm
- Perform a GaAs cap wet etch to separate the gain, phase, and grating contacts. The oxide layers protecting the alignment marks should be unaffected.
- Do not remove the PR yet.

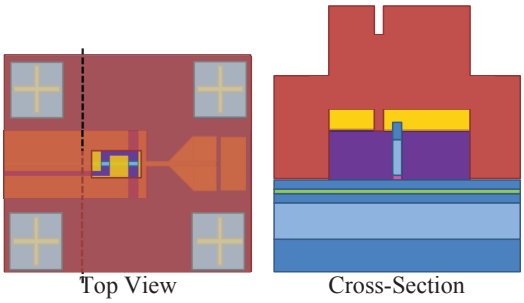

Etch Oxide

- Wet Etch (BOE)
  - ∗ Chemical: BOE (Buffered Oxide Etch)
  - ∗ Etch Rate: ∼8 nm/sec
  - ∗ Etch Time: ∼15 sec
  - ∗ Desired Etch Depth: ∼120 nm
- Perform BOE etch to reveal the metallic alignment marks.

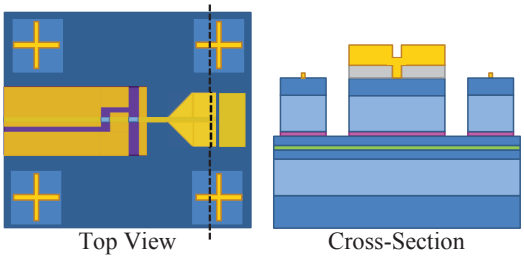

Remove PR

- Acetone → IPA → Water → IPA → Dry with N_2
- Descum in O_2 planar plasma etcher

E-Beam Lithography

- ZEP as positive e-beam resist
  - Open up windows for the Pd deposition.

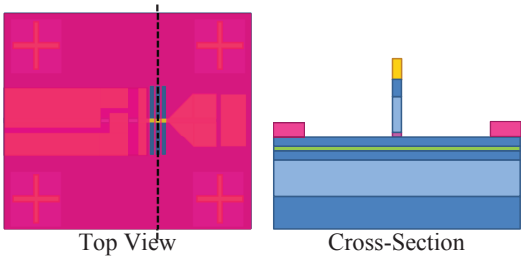

Deposit Palladium

- CHA Evaporator (E-Beam)
  - Metal: Pd
  - Thickness: 10 nm
  - Rate: 1 Å/s
- This thickness must be significantly thinner than the e-beam resist layer.

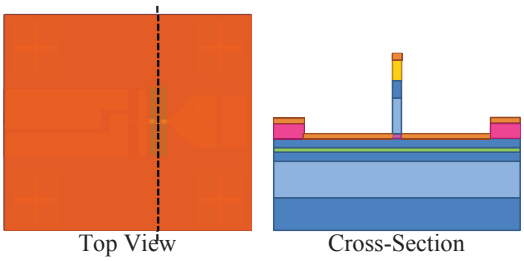

Liftoff

- Acetone → IPA → Water → IPA → Dry with N_2

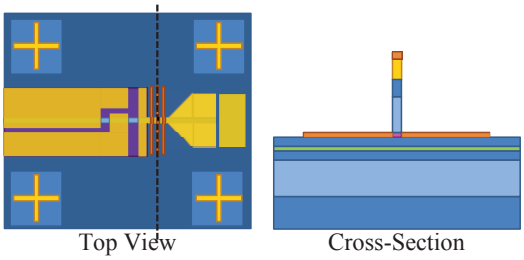

Lapping and Polishing

- Lap backside of sample to a thickness of ∼6.5 mils (165 μm)

Deposit N-Type Contact Metal (Backside)

- CHA Evaporator (E-Beam)
  - Metals: Ge | Au | Ni | Au
  - Thicknesses: 20 | 50 | 30 | 50 nm
  - Rates: 1 | 2 | 1 | 2 Å/s

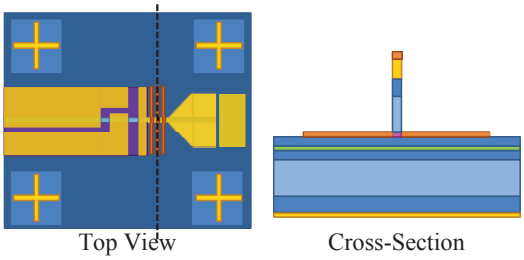

Anneal

- Jipelec RTP
  - Temperature: 400°C
  - Time: 30 sec
  - Ambient: N_2

Cleave (Optional)

- Cleave location defines cavity length

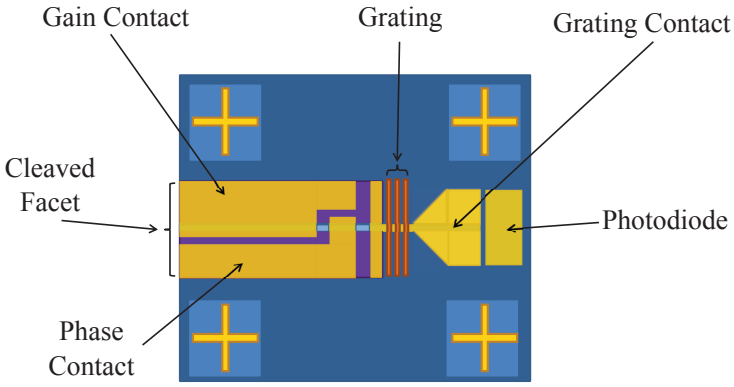

B.3 Distributed Feedback Laser Sensor

This fabrication process uses an electronic e-beam mask to define the ridge and grating, and a photolithography mask titled *AmirBenYMK_2012-12-17*, dated 12/17/2012, which is used to open a window around the ridge and pattern the contact metal. The photolithography mask was made by Compugraphics.

The e-beam mask contains 10 DFB laser ridges, with three different grating periodicities and three different apodizations (with the center point for each parameter repeated), all with a length of 1.04 mm. The grating periodicities are designed for 985, 990, and 995 nm. The apodized ridges are 3 μm in the wide sections, and vary between 2.6, 2.7, and 2.8 μm in the narrow sections (apodization of 200, 150, and 100 nm from each side of the ridge). This pattern is then arrayed on the sample such that there are 30 parallel ridges, with a total length of 10.4 mm.

The photolithography mask is comprised of many different patterns, each clearly labeled. The patterns used for the DFB laser sensor are *6UM T 1UM W STRAIGHT*, which opens a 6 μm-wide window around the ridge, and *METAL FOR STRAIGHT LASER*, which is used to pattern the contact metal pads (155 μm wide).

The fabrication process is designed to etch 600 nm deep, so that the bottom of the etch ends at the top of the core region.

Clean Sample

- Acetone (using sonication) → Methanol → IPA → Water → IPA → dry with N_2

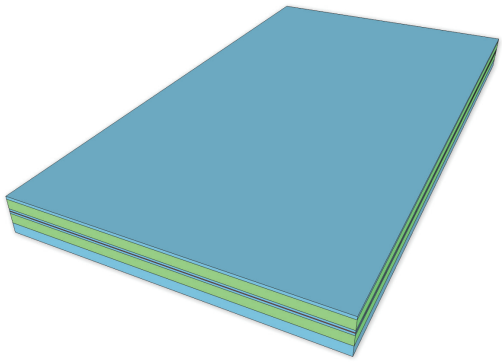

Deposit SiO_2

- PlasmaLab PECVD
  - Power: 35 W
  - Pressure: 1000 mTorr
  - Temperature: 300°C
  - N_2O Flow Rate: 114 sccm
  - SiH_4 Flow Rate: 11 sccm
  - Deposition Time: 11 min
  - Deposition Rate: 10.8 nm/min
  - Desired Thickness: ∼120 nm

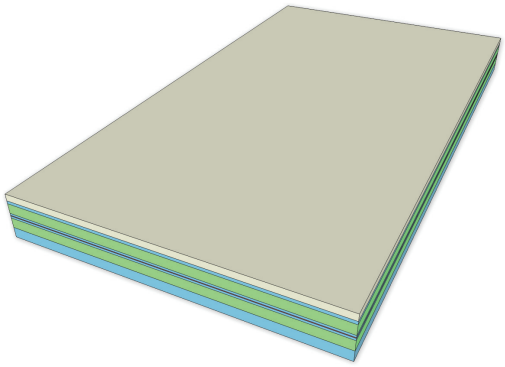

E-Beam Lithography

- ZEP as positive e-beam resist
  - Pattern apodized ridge
- Since ZEP is a positive resist, this will open up windows on each side of the ridge, but the rest of the sample will still be covered in e-beam resist.

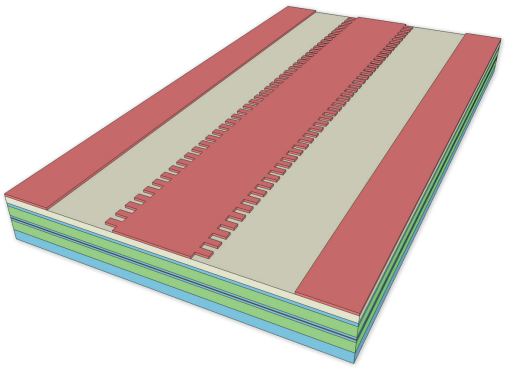

Etch Oxide

- PlasmaLab Freon RIE
  - Power: 90 W
  - Pressure: 35 mTorr
  - CF_4 Flow Rate: 9.5 sccm
  - CHF_3 Flow Rate: 30 sccm
  - Etch Time: 10 min
  - Etch Rate: 14 nm/min
  - Desired Etch Depth: ∼140 nm

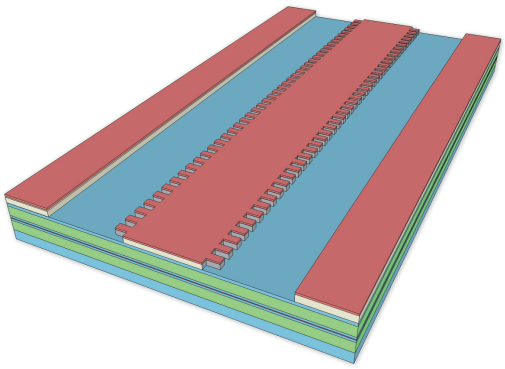

Remove E-Beam Resist

- O_2 Planar Plasma Etcher
  - Etch Time: 20 min
  - Etch until all ZEP has been removed

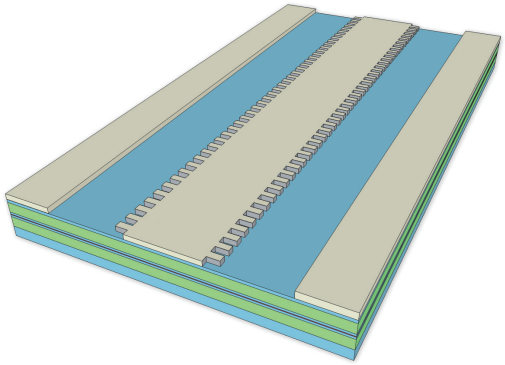

Etch Ridge

- PlasmaTherm ICP-RIE
  - RF1 Power: 25 W
  - RF2 (ICP) Power: 50 W
  - Pressure: 3 mTorr
  - $SiCl_4$ Flow Rate: 1.7 sccm
  - H_2 Flow Rate: 1 sccm
  - Ar Flow Rate: 10 sccm
  - DC Voltage: ∼80 V
  - Etch Time: ∼8.5 min
  - Etch Rate: ∼70 nm/min
  - Desired Etch Depth: 600 nm

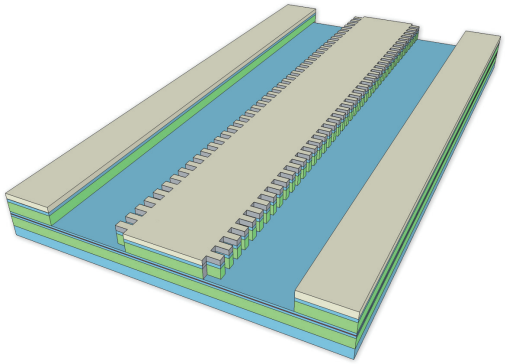

Deposit SiO_2

- PlasmaLab PECVD
  - Power: 35 W
  - Pressure: 1000 mTorr
  - Temperature: 300°C
  - N_2O Flow Rate: 114 sccm
  - SiH_4 Flow Rate: 11 sccm
  - Deposition Time: 4.5 min
  - Deposition Rate: 10.8 nm/min
  - Desired Thickness: ∼50 nm
  - This thin oxide layer helps passivate the ridge sidewalls, and allows for better BCB adhesion.

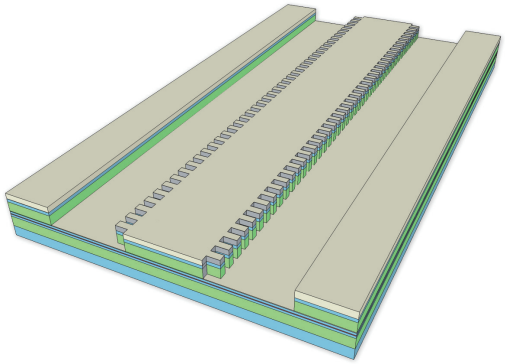

Planarize

- Spin on BCB (∼2.1 μm thick)
- Cure BCB
  - N_2 ambient
  - Ramp up to 250°C for 30 min
  - Remain at 250°C for 1 hr
  - Cool down to room temperature for 3 hrs

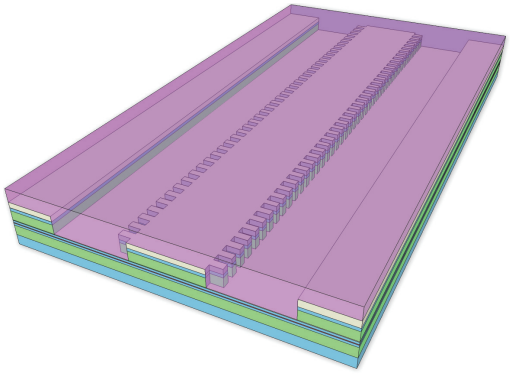

Etch Back BCB (Fast)

- PlasmaLab Freon RIE
  - Power: 90 W
  - Pressure: 35 mTorr
  - CF_4 Flow Rate: 25 sccm
  - O_2 Flow Rate: 12.5 sccm
  - Etch Time: 12 min
  - Etch Rate: ∼160 nm/min
  - Desired Etch Depth: ∼1.9 μm
- This etch removes most of the BCB.

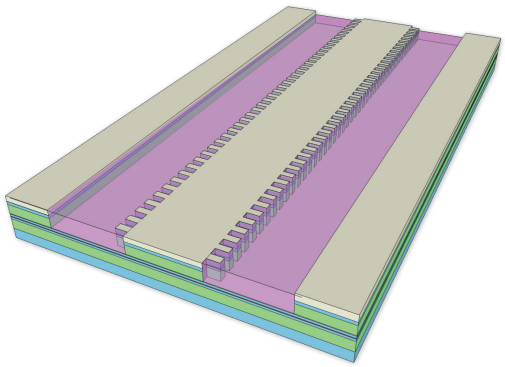

Etch Back BCB (Slow)

- PlasmaLab Freon RIE
  - Power: 90 W
  - Pressure: 35 mTorr
  - CF_4 Flow Rate: 18.5 sccm
  - CHF_3 Flow Rate: 30 sccm
  - Etch Time: ∼15 min
  - Etch Rate: ∼6 nm/min
  - Desired Etch Depth: ∼90 nm
- This etches BCB and SiO_2 at a ∼1:1 ratio. The etch is carefully controlled until it has been determined that the GaAs cap has been exposed.

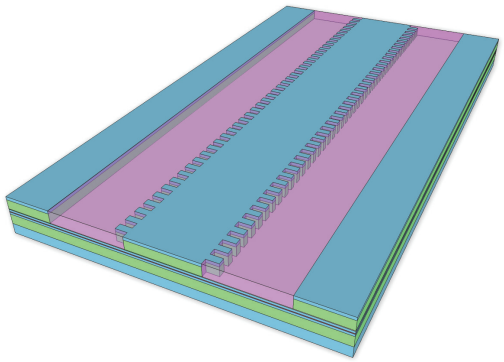

Deposit SiO_2

- PlasmaLab PECVD
  - Power: 35 W
  - Pressure: 1000 mTorr
  - Temperature: 200°C
  - N_2O Flow Rate: 114 sccm
  - SiH_4 Flow Rate: 11 sccm
  - Deposition Time: 11 min
  - Deposition Rate: 10.8 nm/min
  - Desired Thickness: ∼120 nm

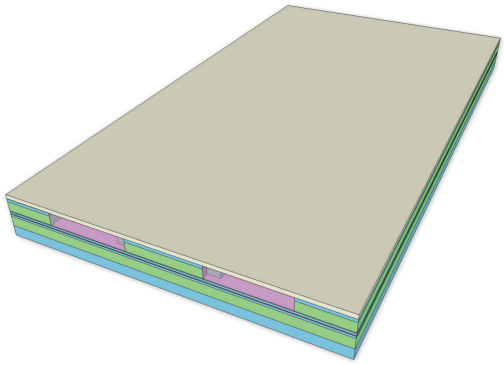

Photolithography: Pattern Oxide Window

- AZ 5214 as negative photoresist
- Pattern negative PR on the sample to open windows around the ridge, so the oxide in this region can be removed, but oxide will remain on the rest of the sample. This ensures all current injection goes into the ridge.

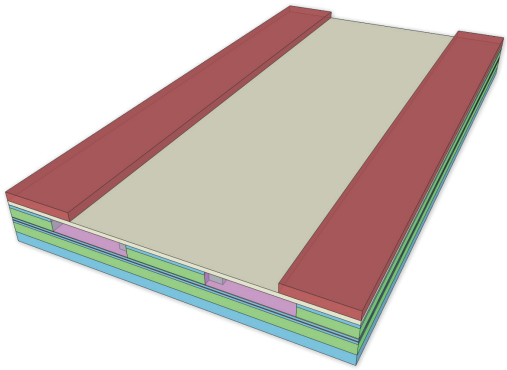

Etch Oxide

- PlasmaLab Freon RIE
  - Power: 90 W
  - Pressure: 35 mTorr
  - CF_4 Flow Rate: 9.5 sccm
  - CHF_3 Flow Rate: 30 sccm
  - Etch Time: 9 min
  - Etch Rate: 14 nm/min
  - Desired Etch Depth: ∼126 nm

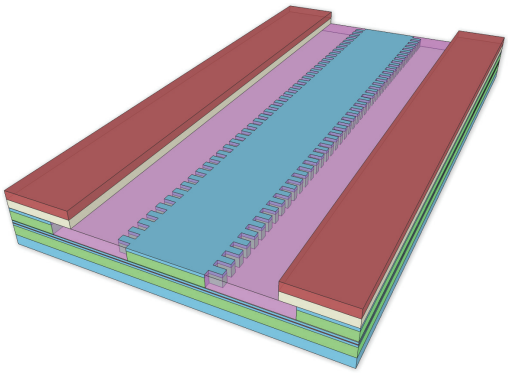

Remove PR

- Acetone → IPA → Water → IPA → Dry with N_2
- Descum in O_2 planar plasma etcher

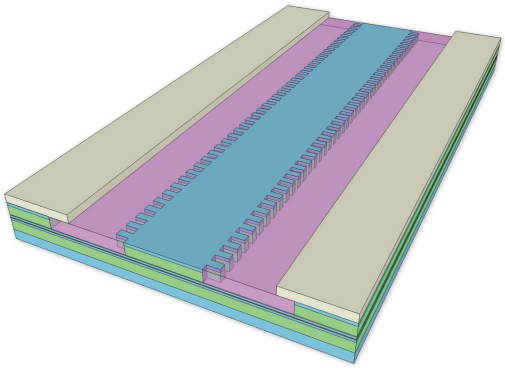

Photolithography: Pattern Contact Metal

- AZ 5214 as negative photoresist

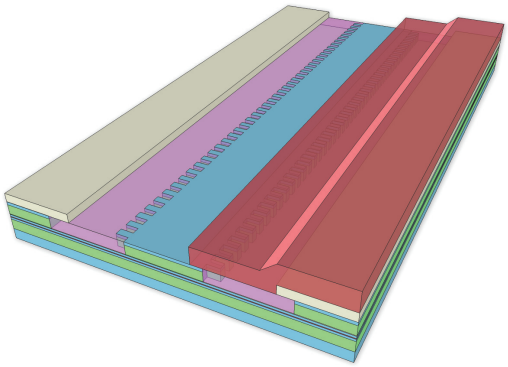

Deposit P-Type Contact Metal

- CHA Evaporator (E-Beam)
  - Metals: Ti | Pt | Au
  - Thicknesses: 15 | 10 | 250 nm
  - Rates: 1 | 1 | 2 Å/s

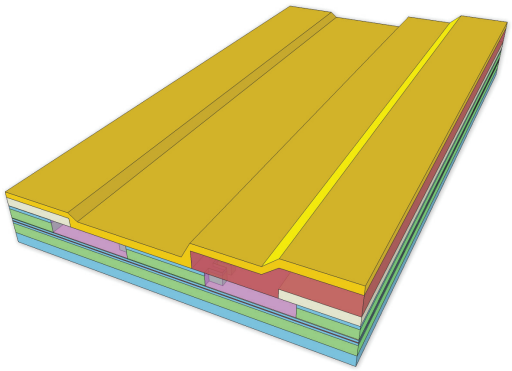

Liftoff

- Acetone → IPA → Water → IPA → Dry with N_2

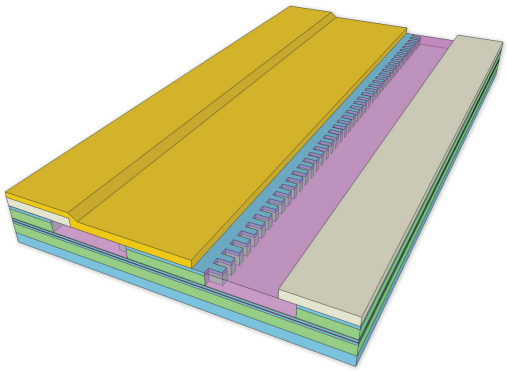

Etch BCB and Oxide

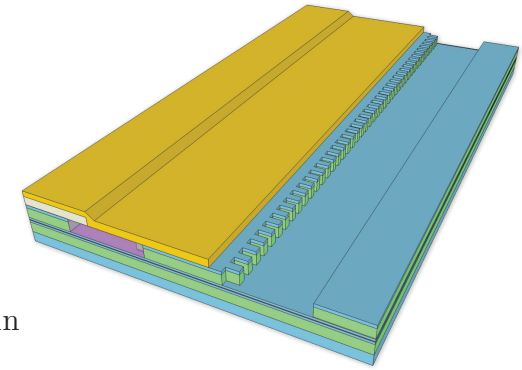

- PlasmaLab Freon RIE
  - Power: 90 W
  - Pressure: 35 mTorr
  - CF_4 Flow Rate: 25 sccm
  - O_2 Flow Rate: 12.5 sccm
  - Etch Time: 15 min
  - BCB Etch Rate: ∼160 nm/min
  - SiO_2 Etch Rate: ∼20 nm/min
  - Total Etch Depth: ∼800 nm

Lapping and Polishing

- Lap backside of sample to a thickness of ∼6.5 mils (165 μm)

Deposit N-Type Contact Metal (Backside)

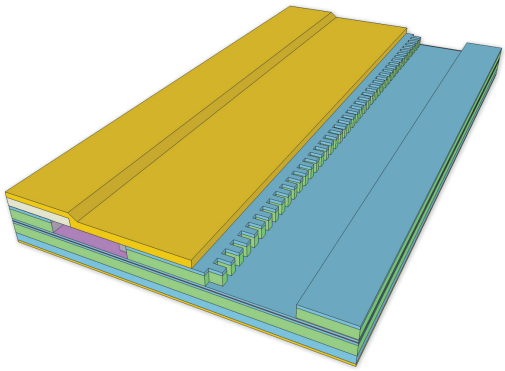

- CHA Evaporator (E-Beam)
  - Metals: Ge | Au | Ni | Au
  - Thicknesses: 20 | 50 | 30 | 50 nm
  - Rates: 1 | 2 | 1 | 2 Å/s

Anneal

- Jipelec RTP
  - Temperature: 400°C
  - Time: 30 sec
  - Ambient: N_2

Deposit Palladium

- CHA Evaporator (E-Beam)
  - Metal: Pd
  - Thickness: 20 nm
  - Rate: 1 Å/s

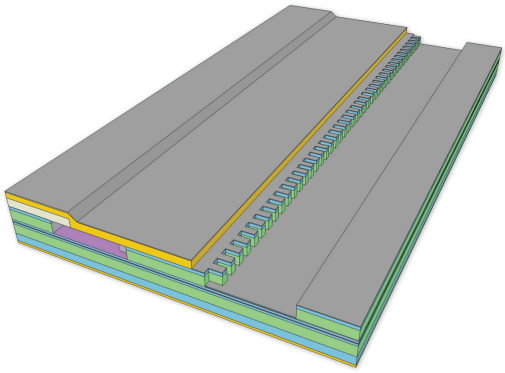

Cleave

- Cleave location defines cavity length

APPENDIX C

SIDE MODE SUPPRESSION RATIO ENHANCEMENT OF PHOTONIC CRYSTAL VERTICAL-CAVITY SURFACE-EMITTING LASERS

VCSELs with two-dimensional PhCs integrated on the surface by etching periodically ordered air holes around a non-etched defect in the center have been shown to be effective in providing single-mode operation with greater than 40 dB side mode suppression ratio (SMSR) [72–75]. The single-mode nature of these devices with their large SMSR is important for a variety of applications including optical communications [76], short-range optical interconnects [77], and optical storage. Further improvements to the SMSR can lead to advancements in high-speed single-mode optical communications in which bit error rates due to modal dispersion can be reduced [78, 79]. Additionally, improving the SMSR has been shown to influence the output beam properties and thus will be important for display applications [80]. Additionally, these single-mode properties are useful for a variety of spectroscopic and sensing techniques, as demonstrated by the PhC VCSEL H_2 sensor.

The value for the SMSR can be calculated from

$$\begin{aligned}\mathrm{SMSR(dB)} \approx 10 \cdot \log_{10}\left[\frac{\Delta\alpha + \Delta g}{\delta_G} + 1\right] = \\ 10 \cdot \log_{10}\left[\left(\frac{I}{I_{th}} - 1\right) \cdot \left(\frac{\alpha_m(\lambda_1) - \alpha_m(\lambda_0) + \Gamma g(\lambda_0) - \Gamma g(\lambda_1)}{(\alpha_i + \alpha_m(\lambda_0))\,\beta_{sp}\eta_r}\right) + 1\right]\end{aligned} \quad \text{(C.1)}$$

where $\alpha_m(\lambda_1)$ is the mirror loss of the first-order mode, $\alpha_m(\lambda_0)$ is the mirror loss of the fundamental mode, $\Gamma g(\lambda_0) - \Gamma g(\lambda_1)$ is the difference in gain between the fundamental and first-order mode frequencies, α_i is the intrinsic loss, β_{sp} is the spontaneous emission factor, η_r is the radiative efficiency, I_{th} is the threshold current, and I is the operating current. A graphical representation of these parameters is presented in Fig. C.1.

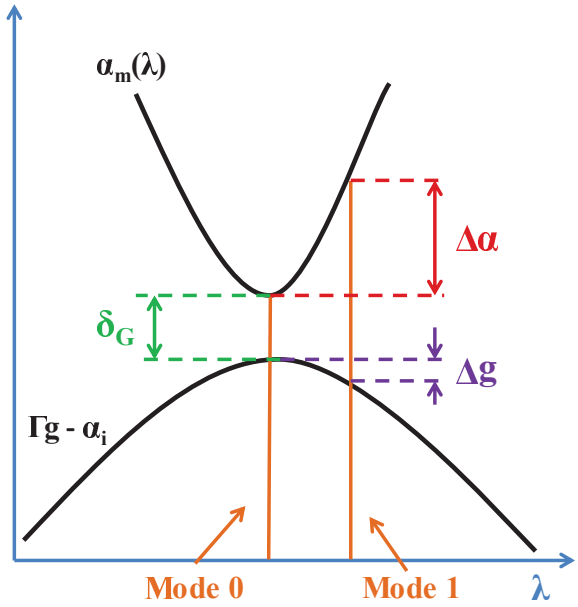

Figure C.1: Graphical representation of side mode suppression ratio.

For the PhC VCSEL H_2 sensor, a thin-film of Pd was deposited over the top surface such that it was located at the bottom of the etched air holes. It was suggested that in addition to providing H_2 sensing capabilities, the inclusion of this metal would further enhance the single-mode behavior of the PhC VCSEL. This inclusion of metal within the holes of the PhC VCSEL enhances side-mode suppression due to at least three factors. The first is that the metal deposited within the holes is lossy in nature, and the higher-order modes being more spread out, interact more with this lossy material than the fundamental mode. This implies that the higher-order modes experience a larger propagation loss through the PhC layers than the fundamental mode. The next factor is that the inclusion of the metal leads to greater confinement of the modes which causes them to diverge more quickly below the PhC structure, so that once it is reflected from the bottom DBR back up towards the PhC structure, much of the power is no longer contained within the PhC defect, leading to radiative losses. Naturally, since the higher-order modes are affected more by the metal, they undergo more of this beam spreading, and as a result, experience greater losses. The third factor is that the interface at the top of the deposited metal layer, between the PhC with metal-filled holes and PhC with air holes, experiences an index mismatch, which adds a greater reflective loss for the higher-order modes [81].

First, simulations were performed for an oxide-confined PhC VCSEL that

is similar in structure and PhC pattern to the one used for the H_2 sensor. An analysis was run to quantify the effect that different metals had on SMSR enhancement, and a figure of merit was decided to determine the best metals to use. Based on this figure of merit, it was determined that Cr was superior to many other metals (including Pd, which was used for the H_2 sensor). Then, the full PhC VCSEL structure was simulated assuming Cr located inside the etched air holes, and the SMSR as a function of Cr thickness was modeled. Next, experimental measurements were performed on a readily-available implant-confined PhC VCSEL to experimentally demonstrate the effect of Cr on SMSR enhancement. Due to the significant difference in material structure for the implant-confined PhC VCSEL, new simulation results were also derived. Here, the simulation methods and results, as well as the experimental measurements are presented.

C.1 Oxide-Confined PhC VCSELs

C.1.1 Device Design

The VCSEL structure used for these simulations is designed to lase at 850 nm with 3 GaAs quantum wells. The top DBR is comprised of 24.5 pairs of alternating $Al_{0.15}Ga_{0.85}As$ / $Al_{0.90}Ga_{0.10}As$ layers each with a thickness of $\lambda/4n$, and the bottom DBR is comprised of 34.5 pairs of the same layers. Just above the active region is an $Al_{0.98}Ga_{0.02}As$ layer that is laterally oxidized, forming a 12 μm diameter aperture. This helps to initially confine the current and the optical mode before it interacts with the PhC. The PhC itself is a hexagonal pattern with a hole period of 4.5 μm and varying hole diameters. In the center of the pattern is one hole missing, which acts as a defect in the PhC, further confining the mode to this defect diameter. The pattern is etched 90% of the way through the top DBR, and a layer of metal is then deposited inside the hole. Figure C.2 shows the PhC VCSEL structure with the important elements labeled and a cross-section of the same structure demonstrating where the deposited metal is located. Table C.1 shows a detailed layer structure for the VCSEL including thicknesses and refractive indices. It should be noted that this layer structure matches that of the PhC VCSEL H_2 sensor shown in Fig. 3.2.

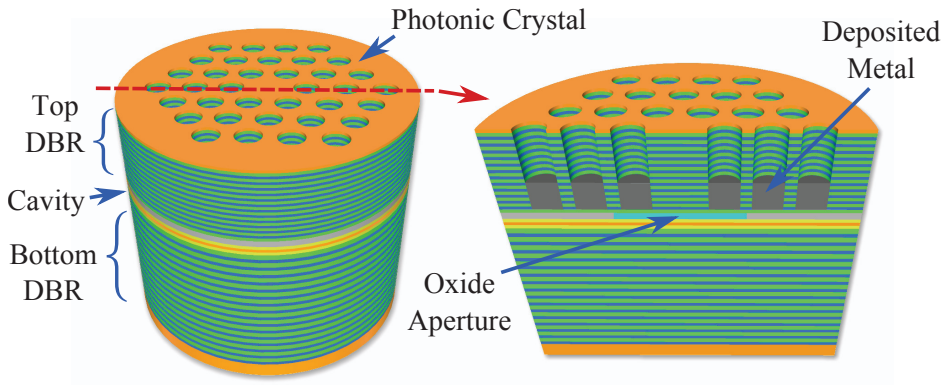

Figure C.2: Illustration and cross-sectional diagram of the oxide-confined PhC VCSEL structure used for the simulations.

Table C.1: Layer structure for the oxide-confined PhC VCSEL

Label	**Thickness (nm)**	**Material**	**Refractive Index**
		Air	1.00
Cap	80	GaAs	3.66
Top DBR 24.5 Pairs	60 69	$Al_{0.15}Ga_{0.85}As$ $Al_{0.90}Ga_{0.10}As$	3.53 3.06
Oxide Aperture	70	$Al_{0.98}Ga_{0.02}As$	3.01
Spacer	127	$Al_{0.60}Ga_{0.40}As$	3.24
4 Barriers & 3 QWs	10 8	$Al_{0.30}Ga_{0.70}As$ GaAs	3.43 3.66
Spacer	127	$Al_{0.60}Ga_{0.40}As$	3.24
Bottom DBR 34.5 Pairs	60 69	$Al_{0.15}Ga_{0.85}As$ $Al_{0.90}Ga_{0.10}As$	3.53 3.06
Substrate		GaAs	3.66

C.1.2 Metal Selection

The understanding is that since the metal is lossy in nature, and the higher-order modes are more spread out and have a greater overlap with the metal, the propagation loss through the PhC for the higher-order modes is much higher than that of the fundamental. In this case, the thickness and physical properties of the selected metal are very significant. The selected metal must

have adequate loss such that the higher-order mode is sufficiently suppressed, yet must be impedance matched to the AlGaAs layer in which it is embedded. If the loss of the metal is high, but the impedance matching is poor, the penetration depth will be very small, and the metal will have only a negligible difference on the mode suppression. For the impedance matching, a simple transmission line model is used such that the impedance of the AlGaAs layer in which the metal is embedded (Z_{AlGaAs}) is matched to the impedance of the metal (Z_{metal}), such that the reflection Γ is as small as possible. Therefore, when selecting a metal for the PhC structure, a figure of merit ζ is selected that represents the percentage of power that is absorbed by the metal from the simple transmission line model, with larger values corresponding to better SMSRs. This figure of merit is by

$$\zeta = 1 - \left| \frac{Z_{AlGaAs} - Z_{metal}}{Z_{AlGaAs} + Z_{metal}} \right|^2 = 1 - \left| \frac{n_{AlGaAs} - \tilde{n}_{metal}}{n_{AlGaAs} + \tilde{n}_{metal}} \right|^2 \tag{C.2}$$

with n_{AlGaAs} corresponding to the refractive index of the AlGaAs and $\tilde{n}_{metal}$ corresponding to the complex refractive index of the metal. Since the top DBR of the PhC VCSEL is comprised of alternating layers of different AlGaAs concentrations, ζ parameters must be calculated for each of these AlGaAs concentrations. Table C.2 shows the complex refractive indices and figures of merit for a variety of metals commonly used in semiconductor laser fabrication. Using this figure of merit for the metals selected, Cr should provide the most SMSR enhancement.

C.1.3 Transmission Matrix Method Simulations

The transmission matrix method involves breaking down the full three-dimensional device geometry into two-dimensional slices. Each slice corresponds to a layer in the VCSEL structure. The transmission matrices representing propagation through each layer and the interface between each layer are formulated using the same technique presented in Chapter 3.2.

After the transmission matrices for each layer and the interfaces between layers are derived, a single transmission matrix representing the entire structure is formed by multiplying each of the layers together. This transmission matrix is then used to solve for the resonant complex wavelength of the structure, which is used to determine the photon lifetime, and therefore the

Table C.2: Figure of merit ζ for various metals embedded in each of the top DBR AlGaAs concentrations

Metal	**Refractive Index**	$\boldsymbol{\zeta}$ **($Al_{0.15}Ga_{0.85}As$)**	$\boldsymbol{\zeta}$ **($Al_{0.90}Ga_{0.10}As$)**
Cr [82]	$3.24387 - i3.4964$	0.7882	0.7643
Ni [83]	$2.57929 - i4.5357$	0.6290	0.6030
Pt [83]	$2.99157 - i5.1694$	0.6099	0.5783
Pd [82]	$2.17935 - i5.3175$	0.5055	0.4789
Al [84]	$2.58839 - i8.1687$	0.3509	0.3214
Au [83]	$0.19673 - i5.5843$	0.0616	0.0576
Ag [83]	$0.15214 - i5.6785$	0.0469	0.0438

mirror loss. This is done for all metal types, thicknesses, and hole diameters for both the fundamental and first-order modes to show how the mirror loss shift between the modes is larger with metal added to the holes.

One key property of the transmission matrix method is the assumption that the mode shape is unchanged throughout the length of the device. This implies that any change in the mirror loss from the inclusion of metal is due to the increased propagation loss through the layers rather than the diffraction of the beam below the PhC structure. Figure C.3 shows the difference in mirror loss between the first-order and fundamental modes versus metal thickness for three selected metals and three hole diameters. To simplify the simulation, each metal thickness is specified as an integer number of $\lambda/8$-thick layers. It is clear that the added metals increase the mirror loss difference, which would in turn enhance the SMSR. Additionally, of the three metals, it seems that Cr is the best at suppressing the higher order mode, as the previously mentioned figure of merit suggests. Additionally for Cr, it seems that the 2 m hole diameter yields the best SMSR enhancement, so further simulations will use this value.

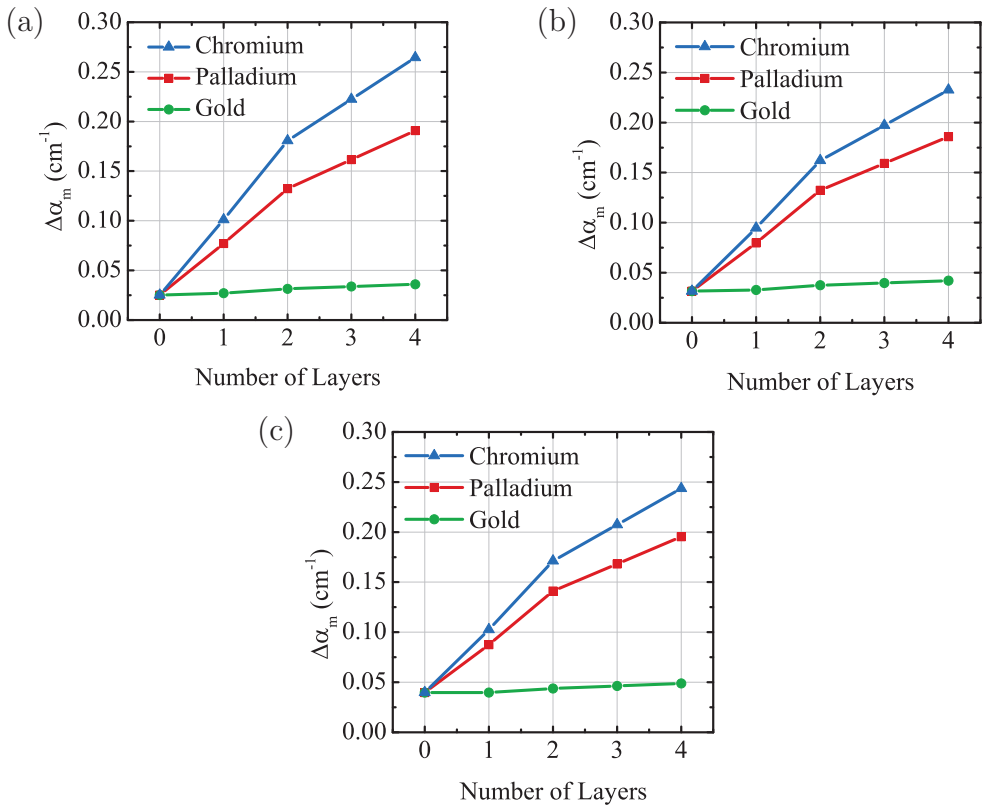

Figure C.3: Difference in mirror loss between the first-order and fundamental modes as a function of metal thickness (defined by the number of layers each with $\lambda/8$ thickness) for oxide-confined PhC VCSEL structures with a 4.5 μm period and (a) 2 μm, (b) 2.5 μm, and (c) 3 μm hole diameter.

C.1.4 Plane Wave Admittance Method Simulations

As mentioned, one drawback of the TMM is that it does not take the changing mode shape into consideration. As a result, the mirror losses produced by this method will not yield an accurate value for the SMSR, because it is a poor approximation for the higher-order modes. Additionally, since it is believed that a significant portion of the side-mode suppression is due to the changing mode shape of the reflected beam from the bottom DBR, the transmission matrix method will also underestimate the actual change in mirror loss. Therefore, a more accurate three-dimensional simulation technique is required. There are a variety of methods used in literature for modeling PhC VCSEL structures, with the seemingly most accurate being the plane wave admittance method (PWAM) [61].

The PWAM combines the plane wave expansion method and the method of

lines to produce a relatively fast and very accurate way of modeling a variety of photonic devices including PhC VCSELs. Essentially, each mode within the structure is decomposed into a series of plane waves traveling at a variety of directions through the structure [85]. This allows for accurate computations of mirror loss due to the radiative loss from the reflected beam. The plane wave admittance simulations were performed using a piece of software called PSlab [86].

The device structure was created in much the same way as for the TMM. Each two-dimensional layer is defined along with its geometry and material parameters, and later each defined layer is stacked to form the full structure. The PWAM simulation provides the electric field profiles in the structure, and the complex resonant frequency in the structure. Like for the TMM, the complex frequency is used to determine the photon lifetime, which is used to determine the mirror loss. Figure C.4 shows the normalized electric field profiles for the fundamental and first-order modes at two locations in the PhC VCSEL structure: the top and bottom DBRs. As shown, the field clearly expands as it travels from the top DBR with the PhC holes to the bottom DBR. Since the bottom DBR is designed to reflect plane waves at normal incidence, most of the expanded field will not be reflected back into the PhC defect region, and will be effectively lost. From these plots, it also appears that the first-order mode spreads more in the bottom DBR than the fundamental mode. This implies that the first-order mode will experience more loss than the fundamental mode, enhancing the SMSR.

Using (C.1), one can calculate the SMSR from the simulated difference in mirror loss. In this equation, $\alpha_m(\lambda_1)$ is the mirror loss of the first-order mode, $\alpha_m(\lambda_0)$ is the mirror loss of the fundamental mode, $\Gamma g(\lambda_0) - \Gamma g(\lambda_1)$ is the difference in gain between the fundamental and first-order mode frequencies (this is a small value compared to $\Delta\alpha$, and will be ignored), α_i is the intrinsic loss with is assumed to be 10 cm^{-1} for both modes, β_{sp} is the spontaneous emission factor which is assumed to be 10^{-3} for a 7 μm diameter VCSEL [87] (defined by the defect diameter in the PhC for 2 μm diameter holes), η_r is the radiative efficiency which is assumed to be 0.82915, I_{th} is the threshold current which is assumed to be 1 mA [39], and I is the operating current which is assumed to be 12 mA.

From the results of the TMM simulation, Cr and Pd seem to be adequate metals for a noticeable SMSR enhancement. Additionally for Cr, 2 μm-

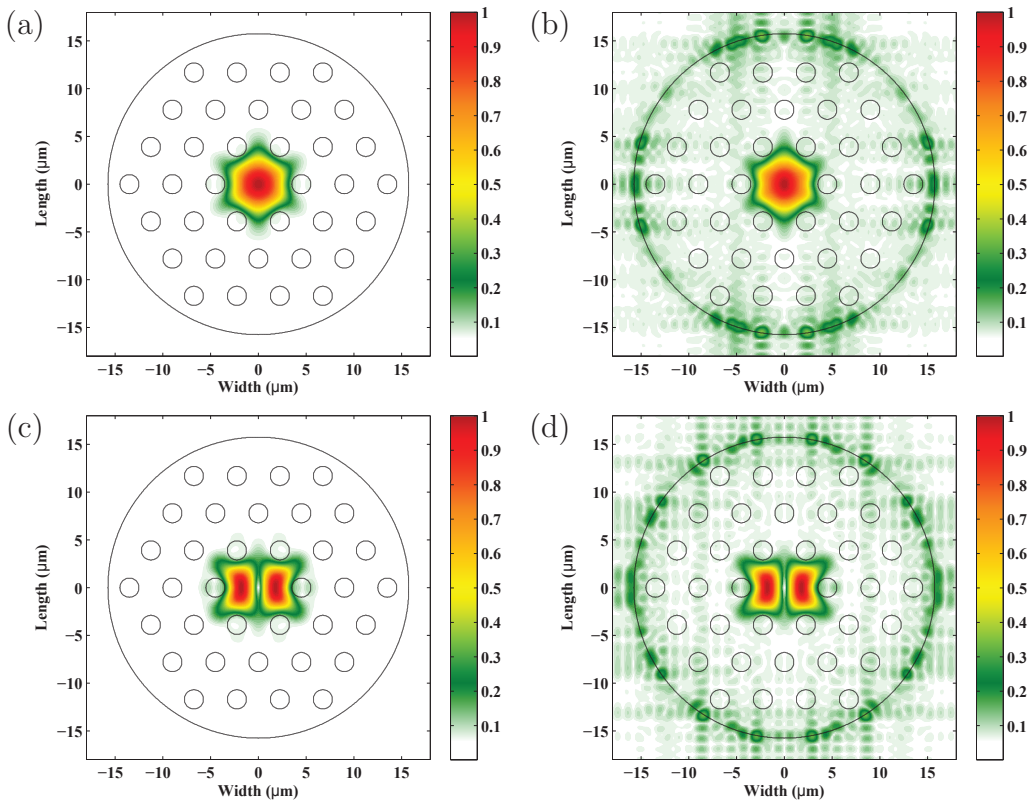

Figure C.4: Field profiles in the oxide-confined PhC VCSEL for the normalized electric field of the (a) fundamental mode in the top DBR, (b) fundamental mode in the bottom DBR, (c) first-order mode in the top DBR, and (d) first-order mode in the bottom DBR. The hole patterns displayed for the bottom DBRs are shown for reference; however, there are no etched holes in the bottom DBR.

diameter holes produce the best SMSR. Therefore, the PWAM simulations were performed for various thicknesses of Cr and Pd with 2 μm diameter holes. The results of these simulations are shown in Table C.3, and a plot of the SMSR versus metal thickness for the chosen metals is shown in Fig. C.5.

From Fig. C.5, it is clear that adding metal in the holes is an effective method of enhancing side-mode suppression. Additionally, the SMSR saturates at a metal thickness of about 500 nm, which is a reasonable metal thickness to use for semiconductor laser fabrication. One notable property of Fig. C.5 is the slight dip at 2.93 μm of metal. That thickness is the total height of the etched PhC holes, and the dip that occurs from fully filling the holes implies that some of the SMSR enhancement is the result of the mode mismatch between adjacent metal-filled and non-metal-filled PhC

layers, which is no longer present if the holes are entirely filled.

Table C.3: Simulation results for the SMSR enhancement of oxide-confined PhC VCSELs

Metal Thickness (μm)	**Chromium**			**Palladium**		
	$\alpha_m\,(\lambda_0)$ **(cm^{-1})**	$\alpha_m\,(\lambda_1)$ **(cm^{-1})**	**SMSR (dB)**	$\alpha_m\,(\lambda_0)$ **(cm^{-1})**	$\alpha_m\,(\lambda_1)$ **(cm^{-1})**	**SMSR (dB)**
0.00	16.1915	24.1734	36.0689	16.1915	24.1734	36.0689
0.05	22.4849	36.2416	37.4975	26.4669	41.1585	37.2809
0.20	25.3351	48.3880	39.3741	27.4135	49.7107	38.9812
0.50	29.5158	59.5350	40.0351	29.5214	57.3443	39.7045
1.00	31.3890	63.9272	40.1839	29.8873	58.3714	39.7665
2.00	32.0110	65.0434	40.1846	30.0694	58.7458	39.7760
2.50	32.0644	65.1378	40.1844	30.0948	58.8136	39.7796
2.93	34.5990	67.7051	39.9347	32.6299	61.3854	39.5189

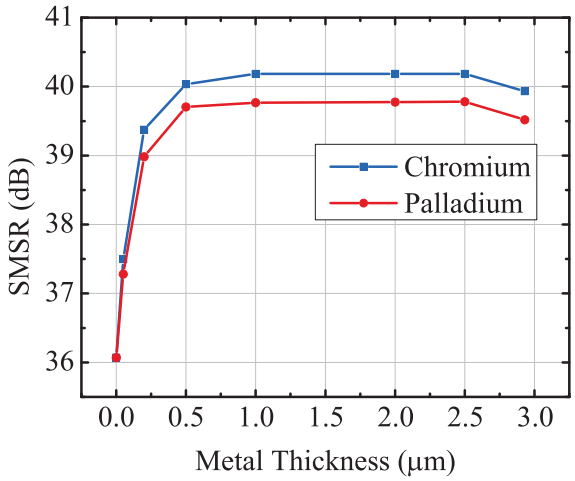

Figure C.5: SMSR versus metal thickness for Cr and Pd in the oxide-confined PhC VCSEL structure.

C.2 Implant-Confined PhC VCSELs

Due to the simulation results for the oxide-confined PhC VCSELs, which have demonstrated that the SMSR could theoretically be improved by partially filling the etched air holes with a metal layer, experimental verification was desired. The previous simulation results studied a variety of metals and found Cr to be the most effective at improving the SMSR; therefore, these experimental results were performed using Cr as the SMSR enhancement metal. To verify this concept experimentally, implant-confined VCSELs with an etched PhC were fabricated, and a 30 nm blanket layer of Cr was deposited. The implant-confined design was chosen over a similar oxide-confined design due entirely to availability. Since the layer structure of these VCSELs is different from that of the previous simulated work, and since a blanket deposition was performed covering the top DBR instead of just partially filling the holes, new simulation results were required for direct comparison.

C.2.1 Device Design

Figure C.6 shows a cross-section of the PhC VCSEL with Cr deposited, showing that the Cr layer is present on the top of the DBR as well as inside the etched air holes. Table C.4 details the layer structure for the simulated VCSEL, including the refractive index of each layer. This VCSEL is designed to lase at a wavelength of 850 nm. The PhC is formed with etched holes of 1.8 μm diameter and 3μm period. This PhC is etched through 80% of the top DBR.

C.2.2 Simulation Methods

The simulation procedure used was the PWAM [85], which like the simulation for the oxide-confined PhC VCSEL, was performed using a software solution called PSlab [86]. The output of the PWAM simulation can be used to determine the electric fields within the structure, as well as the resonant frequencies, which can then be used to determine the mirror losses. The SMSR is calculated using (C.1), and uses the difference in mirror loss between the fundamental and first-order mode from the PWAM simulation.

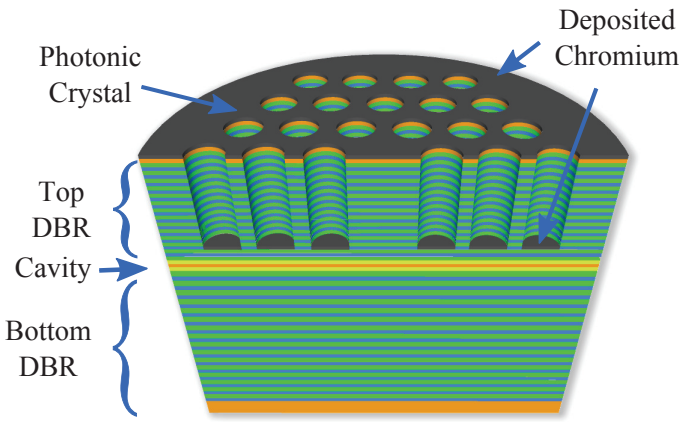

Figure C.6: Cross-sectional diagram of the implant-confined PhC VCSEL structure used for the simulations and similar to that used for the experimental measurements.

Table C.4: Layer structure for the implant-confined PhC VCSEL

Label	**Thickness (nm)**	**Material**	**Refractive Index**
—	—	Air	1.00
Cr	30	Cr	$3.24 - i3.50$
Cap	20 300	GaAs $Al_{0.15}Ga_{0.85}As$	3.66 3.53
Top DBR 21 Pairs	71 60	AlAs $Al_{0.15}Ga_{0.85}As$	3.00 3.53
Spacer	99	$Al_{0.60}Ga_{0.40}As$	3.24
4 Barriers & 3 QWs	10 8	$Al_{0.30}Ga_{0.70}As$ GaAs	3.43 3.66
Spacer	99	$Al_{0.60}Ga_{0.40}As$	3.24
Bottom DBR 35 Pairs	71 60	AlAs $Al_{0.15}Ga_{0.85}As$	3.00 3.53
Substrate	—	GaAs	3.66

In (C.1), $\alpha_m(\lambda_1)$ is the mirror loss of the first-order mode, $\alpha_m(\lambda_0)$ is the mirror loss of the fundamental mode, $\Gamma g(\lambda_0) - \Gamma g(\lambda_1)$ is the difference in gain between these modes (which is a small value compared to $\Delta\alpha_m$, and will be ignored in these simulations), α_i is the intrinsic loss which is assumed

to be 10 cm^{-1} for both modes, β_{sp} is the spontaneous emission factor which is assumed to be 2×10^{-5} [88], η_r is the radiative efficiency which is assumed to be 0.83 [39], I_{th} is the threshold current, and I is the operating current above threshold.

C.2.3 Simulation Results

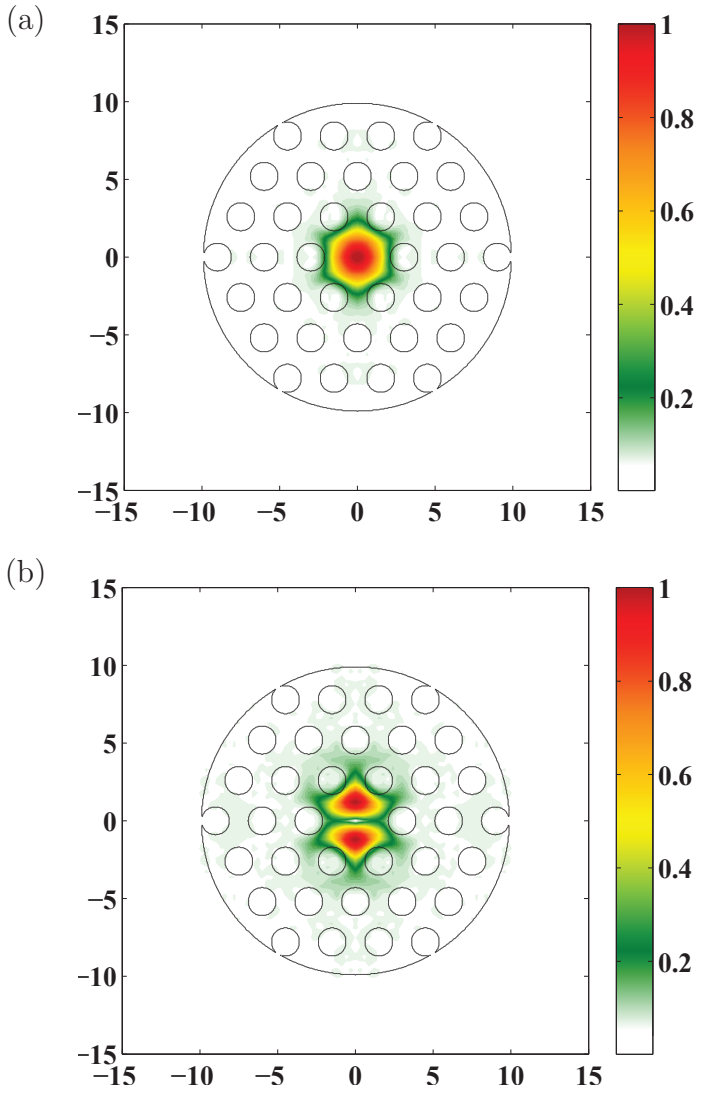

Figure C.7: Field profiles in the implant-confined PhC VCSEL of the normalized electric field contained in the PhC in the top DBR for the (a) fundamental mode, and (b) first-order mode.

Figure C.7 shows the normalized electric field profiles for the fundamental

and first-order modes in the PhC, illustrating their shapes and confinements within the center defect. Table C.5 shows the mirror loss values for the fundamental and first-order modes, and their differences with and without Cr. These values are used to calculate the SMSRs from (C.1). Finally, Fig. C.8 shows the simulated SMSR as a function of current relative to threshold for the cases with and without Cr. As shown, the values for the SMSR are enhanced with the addition of Cr. The SMSR enhancement is approximately 1.8 dB.

Table C.5: Simulated mirror loss values for the fundamental and first-order modes with and without Cr deposited for the implant-confined PhC VCSEL

	$\alpha_m\,(\lambda_0)\ (\mathrm{cm}^{-1})$	$\alpha_m\,(\lambda_1)\ (\mathrm{cm}^{-1})$	$\Delta\alpha_m\ (\mathrm{cm}^{-1})$
No Cr	48.69	94.79	46.10
With Cr	75.68	182.99	107.31

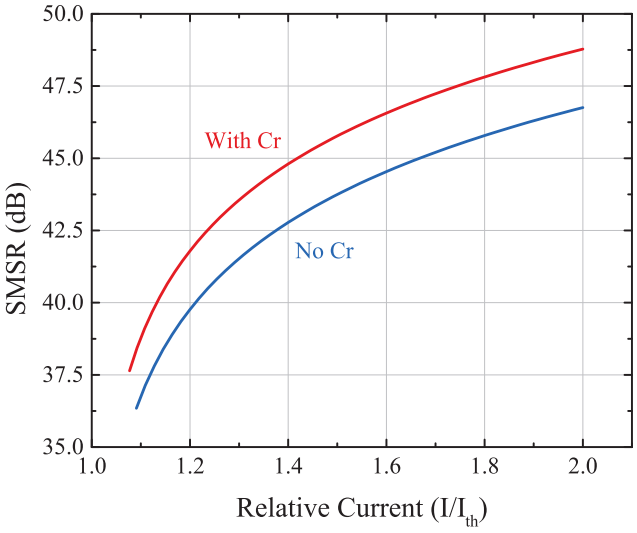

Figure C.8: Simulated SMSR versus current normalized to threshold for the implant-confined PhC VCSEL with and without Cr.

C.2.4 Experimental Measurements

The fabricated PhC VCSELs were tested by injecting CW current through the device using an ILX Lightwave LDC-3916 Laser Diode Controller, collect-

ing the laser output onto a lensed optical fiber, and measuring the resulting spectra using an HP 70951B Optical Spectrum Analyzer (OSA) with the resolution set to 0.08 nm. A photograph of the measured implant-confined PhC VCSEL is shown in Fig. C.9.

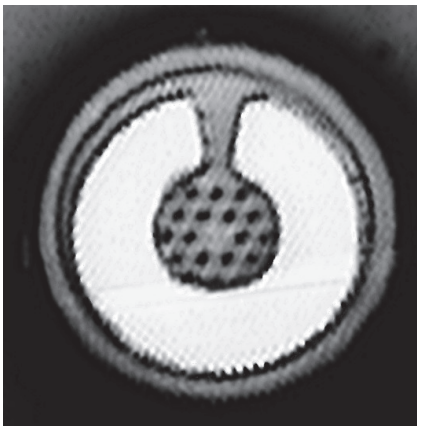

Figure C.9: CCD photograph of the implant-confined PhC VCSEL used for experimental measurements.

Figure C.10 shows the measured spectra of the PhC VCSEL before and after Cr deposition with the peak values normalized. These spectra are collected at a relative current $I/I_{th} = 1.1$. It is clear that the SMSR for the PhC VCSEL with Cr is significantly larger than that of the PhC VCSEL without Cr.

SMSR values were measured for the PhC VCSEL before and after Cr deposition for a variety of relative current values above threshold. This data is presented in Fig. C.11. As expected from the simulation results, the SMSR for the PhC VCSEL with Cr is consistently larger than the PhC VCSEL without Cr. The experimental results show a SMSR enhancement of approximately 4 dB.

The simulated and measured results from this PhC VCSEL are in agreement that the SMSR can be enhanced by incorporating metal within the PhC. The SMSR enhancement is consistent for injection currents relative to threshold. This relative current is used in place of absolute current due to a small increase in threshold current resulting from the Cr layer. Further work should look at isolating Cr within the etched air holes only, as it is believed that the Cr on the top DBR is the cause of this threshold increase. The improvements to the SMSR demonstrated here have potential to impact a variety of single-mode laser applications.

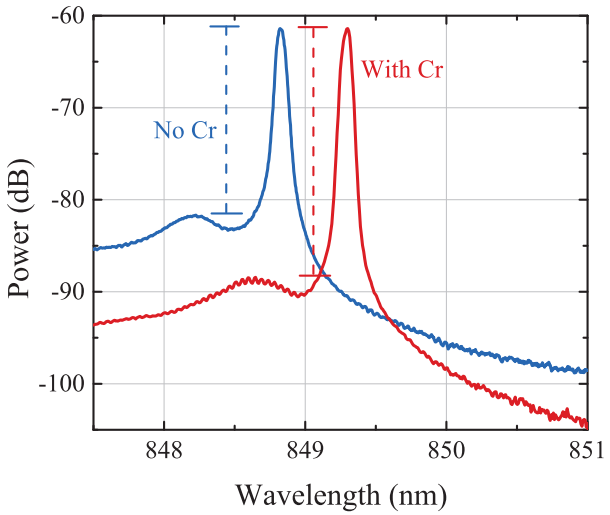

Figure C.10: Measured spectra from the implant-confined PhC VCSEL before and after Cr deposition at relative current I/I_{th}=1.1, showing the improvement in SMSR with the addition of Cr.

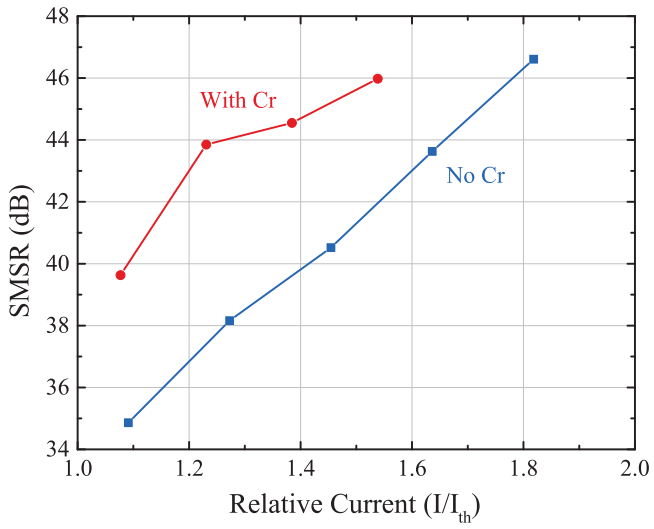

Figure C.11: Measured SMSR versus current normalized to threshold for the implant-confined PhC VCSEL with and without Cr.

REFERENCES

[1] A. M. Omer, "Energy, environment and sustainable development," *Renewable and Sustainable Energy Reviews*, vol. 12, no. 9, pp. 2265–2300, 2008.

[2] I. Dincer, "Renewable energy and sustainable development: a crucial review," *Renewable and Sustainable Energy Reviews*, vol. 4, no. 2, pp. 157–175, 2000.

[3] N. Lefévre, "Measuring the energy security implications of fossil fuel resource concentration," *Energy Policy*, vol. 38, no. 4, pp. 1635–1644, 2010.

[4] M. Nehrir, C. Wang, K. Strunz, H. Aki, R. Ramakumar, J. Bing, Z. Miao, and Z. Salameh, "A review of hybrid Renewable/Alternative energy systems for electric power generation: Configurations, control, and applications," *IEEE Transactions on Sustainable Energy*, vol. 2, no. 4, pp. 392–403, 2011.

[5] T. N. Veziroğlu and S. Şahin, "21st century's energy: Hydrogen energy system," *Energy Conversion and Management*, vol. 49, no. 7, pp. 1820–1831, 2008.

[6] T. N. Veziroğlu and F. Barbir, "Hydrogen: the wonder fuel," *International Journal of Hydrogen Energy*, vol. 17, no. 6, pp. 391–404, 1992.

[7] P. Edwards, V. Kuznetsov, W. David, and N. Brandon, "Hydrogen and fuel cells: Towards a sustainable energy future," *Energy Policy*, vol. 36, no. 12, pp. 4356–4362, 2008.

[8] B. Sørensen, *Hydrogen and Fuel Cells: Emerging Technologies and Applications*. Elsevier Academic Press, 2005.

[9] A. L. Dicks, "Hydrogen generation from natural gas for the fuel cell systems of tomorrow," *Journal of Power Sources*, vol. 61, no. 12, pp. 113–124, 1996.

[10] A. F. Ghenciu, "Review of fuel processing catalysts for hydrogen production in PEM fuel cell systems," *Current Opinion in Solid State and Materials Science*, vol. 6, no. 5, pp. 389–399, 2002.

[11] D. K. Ross, "Hydrogen storage: The major technological barrier to the development of hydrogen fuel cell cars," *Vacuum*, vol. 80, no. 10, pp. 1084–1089, 2006.

[12] L. Schlapbach and A. Züttel, "Hydrogen-storage materials for mobile applications," *Nature*, vol. 414, no. 6861, pp. 353–358, 2001.

[13] W. J. Buttner, M. B. Post, R. Burgess, and C. Rivkin, "An overview of hydrogen safety sensors and requirements," *International Journal of Hydrogen Energy*, vol. 36, no. 3, pp. 2462–2470, 2011.

[14] G. Korotcenkov, S. D. Han, and J. R. Stetter, "Review of electrochemical hydrogen sensors," *Chemical Reviews*, vol. 109, no. 3, pp. 1402–1433, 2009.

[15] K. Ihokura and J. Watson, *The stannic oxide gas sensor: principles and applications*. CRC Press, 1994.

[16] C. Christofides and A. Mandelis, "Solidstate sensors for trace hydrogen gas detection," *Journal of Applied Physics*, vol. 68, no. 6, pp. R1–R30, 1990.

[17] T. B. Flanagan and W. A. Oates, "The palladium-hydrogen system," *Annual Review of Materials Science*, vol. 21, pp. 269–304, 1991.

[18] A. Othonos, K. Kalli, and D. P. Tsai, "Optically thin palladium films on silicon-based substrates and nanostructure formation: effects of hydrogen," *Applied Surface Science*, vol. 161, no. 1-2, pp. 54–60, 2000.

[19] T. Hübert, L. Boon-Brett, G. Black, and U. Banach, "Hydrogen sensors – a review," *Sensors and Actuators B: Chemical*, vol. 157, no. 2, pp. 329–352, 2011.

[20] Z. Zhao, M. A. Carpenter, H. Xia, and D. Welch, "All-optical hydrogen sensor based on a high alloy content palladium thin film," *Sensors and Actuators B: Chemical*, vol. 113, no. 1, pp. 532–538, 2006.

[21] J.-H. Yoon, B.-J. Kim, and J.-S. Kim, "Design and fabrication of micro hydrogen gas sensors using palladium thin film," *Materials Chemistry and Physics*, vol. 133, no. 23, pp. 987–991, 2012.

[22] M. G. Chung, D.-H. Kim, D. K. Seo, T. Kim, H. U. Im, H. M. Lee, J.-B. Yoo, S.-H. Hong, T. J. Kang, and Y. H. Kim, "Flexible hydrogen sensors using graphene with palladium nanoparticle decoration," *Sensors and Actuators B: Chemical*, vol. 169, no. 5, pp. 387–392, 2012.

[23] X. Q. Zeng, M. L. Latimer, Z. L. Xiao, S. Panuganti, U. Welp, W. K. Kwok, and T. Xu, "Hydrogen gas sensing with networks of ultrasmall palladium nanowires formed on filtration membranes," *Nano Letters*, vol. 11, no. 1, pp. 262–268, 2010.

[24] J.-S. Noh, J. M. Lee, and W. Lee, "Low-dimensional palladium nanostructures for fast and reliable hydrogen gas detection," *Sensors*, vol. 11, no. 1, pp. 825–851, 2011.

[25] F. DiMeo Jr., I.-S. Chen, P. Chen, J. Neuner, A. Roerhl, and J. Welch, "MEMS-based hydrogen gas sensors," *Sensors and Actuators B: Chemical*, vol. 117, no. 1, pp. 10–16, 2006.

[26] A. Fabre, E. Finot, J. Demoment, and S. Contreras, "Monitoring the chemical changes in Pd induced by hydrogen absorption using microcantilevers," *Ultramicroscopy*, vol. 97, no. 14, pp. 425–432, 2003.

[27] D. Iannuzzi, M. Slaman, J. Rector, H. Schreuders, S. Deladi, and M. Elwenspoek, "A fiber-top cantilever for hydrogen detection," *Sensors and Actuators B: Chemical*, vol. 121, no. 2, pp. 706–708, 2007.

[28] S. V. Pham, L. J. Kauppinen, M. Dijkstra, H. A. G. M. van Wolferen, R. M. M. De Ridder, and H. J. W. M. Hoekstra, "Read-out of cantilever bending with a grated waveguide optical cavity," *IEEE Photonics Technology Letters*, vol. 23, no. 4, pp. 215–217, 2011.

[29] D. R. Baselt, B. Fruhberger, E. Klaassen, S. Cemalovic, C. L. Britton Jr., S. V. Patel, T. E. Mlsna, D. McCorkle, and B. Warmack, "Design and performance of a microcantilever-based hydrogen sensor," *Sensors and Actuators B: Chemical*, vol. 88, no. 2, pp. 120–131, 2003.

[30] M. Raval, S. McKeown, A. Arbabi, and L. L. Goddard, "Palladium based Fabry-Pérot etalons for hydrogen sensing," in *Optical Sensors*. Monterey, CA: Optical Society of America, 2012, p. STh2B.5.

[31] R. Gupta, A. A. Sagade, and G. U. Kulkarni, "A low cost optical hydrogen sensing device using nanocrystalline Pd grating," *International Journal of Hydrogen Energy*, vol. 37, no. 11, pp. 9443–9449, 2012.

[32] S. J. McKeown and L. L. Goddard, "Hydrogen detection using polarization diversity via a subwavelength fiber aperture," *IEEE Photonics Journal*, vol. 4, no. 5, pp. 1752–1761, 2012.

[33] C. Perrotton, R. J. Westerwaal, N. Javahiraly, M. Slaman, H. Schreuders, B. Dam, and P. Meyrueis, "A reliable, sensitive and fast optical fiber hydrogen sensor based on surface plasmon resonance," *Optics Express*, vol. 21, no. 1, pp. 382–390, 2013.

[34] S. F. O. Silva, L. Coelho, O. J. Frazão, J. L. Santos, and F. X. Malcata, "A review of palladium-based fiber-optic sensors for molecular hydrogen detection," *IEEE Sensors Journal*, vol. 12, no. 1, pp. 93–102, 2012.

[35] S. J. McKeown, B. G. Griffin, and L. L. Goddard, "Fiber optic hydrogen sensor utilizing facet-etched metal nano-apertures," in *2010 23rd Annual Meeting of the IEEE Photonics Society*. Denver, CO: IEEE, 2010, pp. 730–731.

[36] C. Perrotton, N. Javahiraly, M. Slaman, H. Schreuders, B. Dam, and P. Meyrueis, "Optimization of Pd surface plasmon resonance sensors for hydrogen detection," in *Proc. SPIE, SPIE Eco-Photonics 2011: Sustainable Design, Manufacturing, and Engineering Workforce Education for a Green Future*. Strasbourg, France: SPIE, 2011, pp. 80 651F–80 651F–5.

[37] L.-J. Cui, H.-C. Shang, G. Zhang, Z.-X. Zhao, and J. Zhou, "Optical fiber hydrogen sensor based on light reflection and a palladium-sliver thin film," *Optoelectronics Letters*, vol. 7, no. 4, pp. 249–252, 2011.

[38] H. Liu, M. Yang, J. Dai, K. Cao, H. Liao, and P. Zhang, "Hydrogen sensor based on side-polished fiber Bragg gratings coated with thin palladium film," in *Proc. SPIE, 21st International Conference on Optical Fiber Sensors*, vol. 7753. Ottawa, Canada: SPIE, 2011, pp. 77 538O–77 538O–4.

[39] L. A. Coldren and S. W. Corzine, *Diode Lasers and Photonic Integrated Circuits*. New York, NY: John Wiley & Sons, Inc., 1995.

[40] Y. Arakawa and A. Yariv, "Quantum well lasers–gain, spectra, dynamics," *IEEE Journal of Quantum Electronics*, vol. 22, no. 9, pp. 1887–1899, 1986.

[41] C.-P. P. Chao, S.-Y. Y. Hu, P. D. Floyd, K.-K. K. Law, S. W. Corzine, J. L. Merz, A. C. Gossard, and L. A. Coldren, "Fabrication of low-threshold InGaAs/GaAs ridge waveguide lasers by using in situ monitored reactive ion etching," *IEEE Photonics Technology Letters*, vol. 3, no. 7, pp. 585–587, 1991.

[42] P. K. Cheo, *Handbook of Solid–State Lasers*. New York, NY: CRC Press, 1989.

[43] I. P. Kaminow and R. S. Tucker, "Mode-controlled semiconductor lasers," in *Guided-Wave Optoelectronics*, ser. Springer Series in Electronics and Photonics, T. Tamir, Ed. Berlin, Germany: Springer Berlin Heidelberg, 1988, no. 26, pp. 211–315.

[44] B. G. Griffin, C.-L. Chang, A. Arbabi, and L. L. Goddard, "Pd coated edge-emitting lasers for hydrogen sensing applications," in *2010 IEEE Sensors*. Waikoloa, HI: IEEE, 2010, pp. 1710–1713.

[45] B. G. Griffin and L. L. Goddard, "Edge emitting sensors for accurate quantification of hydrogen composition above 0.5%," in *Conference on Lasers and Electro-Optics (CLEO)*. Baltimore, Maryland: IEEE, 2011, pp. 1–2.

[46] P. Tobiška, O. Hugon, A. Trouillet, and H. Gagnaire, "An integrated optic hydrogen sensor based on SPR on palladium," *Sensors and Actuators B: Chemical*, vol. 74, no. 1-3, pp. 168–172, 2001.

[47] C. W. Wilmsen, H. Temkin, and L. A. Coldren, *Vertical-Cavity Surface-Emitting Lasers: Design, Fabrication, Characterization, and Applications*. Cambridge, United Kingdom: Cambridge University Press, 2001.

[48] R. Szweda, "VCSEL applications diversify as technology matures," *III-Vs Review*, vol. 19, no. 1, pp. 34–38, 2006.

[49] K. D. Choquette and H. Q. Hou, "Vertical-cavity surface emitting lasers: moving from research to manufacturing," *Proceedings of the IEEE*, vol. 85, no. 11, pp. 1730–1739, 1997.

[50] M. Henini, "Developments continue for VCSEL research," *III-Vs Review*, vol. 13, no. 1, pp. 18–23, 2000.

[51] A. M. Kasten, M. P. Tan, J. D. Sulkin, P. O. Leisher, and K. D. Choquette, "Photonic crystal vertical cavity lasers with wavelength-independent single-mode behavior," *IEEE Photonics Technology Letters*, vol. 20, no. 23, pp. 2010–2012, 2008.

[52] K.-H. Lee, J.-H. Baek, I.-K. Hwang, Y.-H. Lee, G.-H. Lee, J.-H. Ser, H.-D. Kim, and H.-E. Shin, "Square-lattice photonic-crystal vertical-cavity surface-emitting lasers," *Optics Express*, vol. 12, no. 17, pp. 4136–4143, 2004.

[53] H.-P. P. D. Yang, F.-I. I. Lai, Y.-H. S. Chang, H.-C. C. Yu, C.-P. P. Sung, H.-C. C. Kuo, S.-C. C. Wang, S. Y. Lin, and J.-Y. Y. Chi, "Single-mode (SMSR>40 dB) proton-implanted photonic crystal vertical-cavity surface-emitting lasers," *Electronics Letters*, vol. 41, no. 6, pp. 326– 328, 2005.

[54] D.-S. Song, S.-H. Kim, H.-G. Park, C.-K. Kim, and Y.-H. Lee, "Single-fundamental-mode photonic-crystal vertical-cavity surface-emitting lasers," *Applied Physics Letters*, vol. 80, no. 21, pp. 3901–3903, 2002.

[55] H. J. Unold, M. Golling, R. Michalzik, D. Supper, and K. J. Ebeling, "Photonic crystal surface-emitting lasers: tailoring waveguiding for single-mode emission," in *27th European Conference on Optical Communication, ECOC 2001*, vol. 4. Amsterdam, Netherlands: IEEE, 2001, pp. 520– 521.

[56] H. Hasegawa, Y. Oikawa, T. Hirooka, M. Yoshida, and M. Nakazawa, "10 Gb/s transmission over 3 km at 850 nm using single-mode photonic crystal fiber, single-mode VCSEL, and si-APD," in *Optical Fiber Communication Conference and Exposition/National Fiber-Optic Engineers Conference, OFC/NFOEC 2006*. Anaheim, California: IEEE, 2006.

[57] J. P. G. Bristow, J. A. Lehman, Y. Liu, M. K. Hibbs-Brenner, L. M. Galarneau, and R. A. Morgan, "Recent progress in short-distance optical interconnects," in *Proc. SPIE, Optoelectronic Interconnects and Packaging IV*, vol. 3005. San Jose, CA: SPIE, 1997, pp. 112–119.

[58] M. Mansuripur and G. T. Sincerbox, "Principles and techniques of optical data storage," *Proceedings of the IEEE*, vol. 85, no. 11, pp. 1780–1796, 1997.

[59] B. G. Griffin, A. M. Kasten, K. D. Choquette, and L. L. Goddard, "Palladium-coated photonic crystal vertical cavity lasers for hydrogen sensing applications," in *2010 23rd Annual Meeting of the IEEE Photonics Society*. Denver, CO: IEEE, 2010, pp. 373–374.

[60] B. G. Griffin, A. Arbabi, A. M. Kasten, K. D. Choquette, and L. L. Goddard, "Hydrogen detection using a functionalized photonic crystal vertical cavity laser," *IEEE Journal of Quantum Electronics*, vol. 48, no. 2, pp. 160–168, 2012.

[61] M. Dems, I.-S. Chung, P. Nyakas, S. Bischoff, and K. Panajotov, "Numerical methods for modeling photonic-crystal VCSELs," *Optics Express*, vol. 18, no. 15, pp. 16 042–16 054, 2010.

[62] H.-Y. Y. Ryu, H.-G. G. Park, and Y.-H. H. Lee, "Two-dimensional photonic crystal semiconductor lasers: computational design, fabrication, and characterization," *IEEE Journal of Selected Topics in Quantum Electronics*, vol. 8, no. 4, pp. 891– 908, 2002.

[63] T. Czyszanowski, M. Dems, R. P. Sarzala, and K. Panajotov, "Numerical analysis of photonic-crystal VCSELs," in *Proc. SPIE, Vertical-Cavity Surface-Emitting Lasers XVII*. San Francisco, CA: SPIE, 2013, pp. 86 390Q–86 390Q.

[64] S. Adachi, "GaAs, AlAs, and $Al_xGa_{1-x}As$: material parameters for use in research and device applications," *Journal of Applied Physics*, vol. 58, no. 3, pp. R1–R29, 1985.

[65] J. Hong, W.-P. P. Huang, and T. Makino, "On the transfer matrix method for distributed-feedback waveguide devices," *Journal of Lightwave Technology*, vol. 10, no. 12, pp. 1860–1868, 1992.

[66] J. G. Mendoza-Alvarez, F. D. Nunes, and N. B. Patel, "Refractive index dependence on free carriers for GaAs," *Journal of Applied Physics*, vol. 51, no. 8, pp. 4365–4367, 1980.

[67] M. Ramanathan, G. Skudlarek, H. H. Wang, and S. B. Darling, "Crossover behavior in the hydrogen sensing mechanism for palladium ultrathin films," *Nanotechnology*, vol. 21, no. 12, p. 125501, 2010.

[68] A. Hubaux and G. Vos, "Decision and detection limits for calibration curves," *Analytical Chemistry*, vol. 42, no. 8, pp. 849–855, 1970.

[69] B. Griffin, A. Arbabi, and L. L. Goddard, "Coupled mode analysis of a distributed bragg reflector laser for hydrogen detection," in *Optical Sensors*. Monterey, CA: Optical Society of America, 2012, p. STh1B.6.

[70] A. Arbabi, Y. M. Kang, and L. L. Goddard, "Cylindrical coordinates coupled mode theory," *IEEE Journal of Quantum Electronics*, vol. 46, no. 12, pp. 1769–1774, 2010.

[71] S. L. Chuang, *Physics of Photonic Devices*. Hoboken, NJ: John Wiley & Sons, Inc., 2009.

[72] M. S. Alias and S. Shaari, "Analysis of single-mode condition and high-order modes discrimination in photonic crystal VCSEL," *Applied Physics B*, vol. 103, no. 4, pp. 889–896, 2011.

[73] A. M. Kasten, M. P. Tan, P. O. Leisher, and K. D. Choquette, "Endlessly single-mode photonic-crystal vertical-cavity surface-emitting lasers," in *Proc. SPIE, Vertical-Cavity Surface-Emitting Lasers XII*, vol. 6908. San Jose, CA: SPIE, Feb. 2008, pp. 69 080B–69 080B.

[74] K. D. Choquette, D. F. Siriani, A. M. Kasten, M. P. Tan, J. D. Sulkin, P. O. Leisher, J. J. Raftery, and A. J. Danner, "Single mode photonic crystal vertical cavity surface emitting lasers," *Advances in Optical Technologies*, vol. 2012, pp. 1–8, 2012.

[75] H. J. Unold, S. W. Z. Mahmoud, R. Jaeger, M. Golling, M. Kicherer, F. Mederer, M. C. Riedl, T. Knoedl, M. Miller, R. Michalzik, and K. J. Ebeling, "Single-mode VCSELs," in *Proc. SPIE, Vertical-Cavity Surface-Emitting Lasers VI*, vol. 4649. San Jose, CA: SPIE, June 2002, pp. 218–229.

[76] S. Matsuo, K. Takeda, T. Sato, M. Notomi, A. Shinya, K. Nozaki, H. Taniyama, K. Hasebe, and T. Kakitsuka, "Electrically-pumped photonic crystal lasers for optical communications," in *European Conference and Exhibition on Optical Communication*. Amsterdam, The Netherlands: Optical Society of America, 2012, p. Th.1.E.2.

[77] A. V. Krishnamoorthy, K. W. Goossen, W. Jan, X. Zheng, R. Ho, G. Li, R. G. Rozier, F. Y. Liu, D. Patil, J. K. Lexau, H. Schwetman, D. Feng, M. Asghari, T. J. Pinguet, and J. E. Cunningham, "Progress in low-power switched optical interconnects," *IEEE Journal of Selected Topics in Quantum Electronics*, vol. 17, no. 2, pp. 357–376, 2011.

[78] R. E. Freund, C.-A. Bunge, N. N. Ledentsov, D. Molin, and C. Caspar, "High-speed transmission in multimode fibers," *IEEE Journal of Lightwave Technology*, vol. 28, no. 4, pp. 569–586, 2010.

[79] J. M. Castro, R. Pimpinella, B. Kose, and B. Lane, "Investigation of the interaction of modal and chromatic dispersion in VCSEL-MMF channels," *Journal of Lightwave Technology*, vol. 30, no. 15, pp. 2532–2541, 2012.

[80] A. M. Kasten, D. F. Siriani, M. K. Hibbs-Brenner, K. L. Johnson, and K. D. Choquette, "Beam properties of visible proton-implanted photonic crystal VCSELs," *IEEE Journal of Selected Topics in Quantum Electronics*, vol. 17, no. 6, pp. 1648–1655, 2011.

[81] B. G. Griffin, A. Arbabi, and L. L. Goddard, "Mode suppression in metal filled photonic crystal vertical cavity lasers," in *Proc. SPIE, Vertical-Cavity Surface-Emitting Lasers XVI*, vol. 8276. San Francisco, CA: SPIE, 2012, pp. 82 760N–82 760N–8.

[82] "SOPRA SA N&K database." [Online]. Available: http://www.sopra-sa.com/

[83] E. D. Palik, *Handbook of Optical Constants of Solids*. San Diego, CA: Academic Press, 1991.

[84] A. D. Rakić, "Algorithm for the determination of intrinsic optical constants of metal films: application to aluminum," *Applied Optics*, vol. 34, no. 22, pp. 4755–4767, 1995.

[85] M. Dems, R. Kotynski, and K. Panajotov, "Plane wave admittance method — a novel approach for determining the electromagnetic modes in photonic structures," *Optics Express*, vol. 13, no. 9, pp. 3196–3207, 2005.

[86] "PSlab." [Online]. Available: http://pslab.sourceforge.net/

[87] G. Shtengel, H. Temkin, T. Uchida, M. Kim, P. Brusenbach, and C. Parsons, "Spontaneous emission factor and its scaling in vertical cavity surface emitting lasers," *Applied Physics Letters*, vol. 64, no. 9, pp. 1062–1064, 1994.

[88] F. Koyama, K. Morito, and K. Iga, "Intensity noise and polarization stability of GaAlAs-GaAs surface emitting lasers," *IEEE Journal of Quantum Electronics*, vol. 27, no. 6, pp. 1410–1416, 1991.